

## **Energy Correction TechNote for $2\nu\beta\beta$ Analysis (Spring 2013)**

Josh Albert, Sean Daugherty, Steve Herrin, Caio Licciardi, Mike Marino, Josiah Walton, Liangjian Wen

## CONTENTS

I. Introduction	4
II. Gain Calibration	4
A. Introduction	4
B. Absolute Charge Injection Gains	4
1. Manual External Charge Injection Runs	4
2. Internal Charge Injection Runs	4
3. Charge Injection Pulse Fitting	6
4. Gains	6
C. Shaping Times and Time Variation	11
1. Principle	11
2. Selected Time Periods	12
3. Implementation	13
D. Time Varying Gain Correction	14
E. Pair Production Gains	14
1. Physics	14
2. Data selection	15
3. Fitting the Peaks	16
F. Gain Validation and Other Tests	17
1. Validation	17
2. Other Tests	18
G. Conclusions	19
III. Grid Shielding Effect and Corrections	22
A. Grid Shielding Effect	22
B. Grid Correction	22
1. Calculation of Grid Correction	23
2. Test of Grid Correction	24
IV. Purity Measurement and Corrections	28
A. Electron Capture on Impurities	28
B. Measuring Electron Lifetime	29
1. Method	29
2. Comparison to Simulation	30
3. Practical Considerations	31
C. Effects of Electron Lifetime on the Energy Resolution	32
1. Position Uncertainty	32
2. Electron Lifetime Uncertainty	33
3. Rate of Change	33
4. Overall	34
D. Measurements of Electron Lifetime in EXO-200	34
1. Time Variation and Correction Function	35
2. Comparison with Recirculation Rate	35
3. Comparison with Gas Purity Monitor Readings	35
4. Electron Lifetime in Low Electric Field	36
5. Electron Lifetime Results	38
V. Light Map and Corrections	42
A. APD gain measurement	42
B. Building the light map	42
1. Calibration Runs	43
2. Event Selection	43
3. Binning the Detector Volume	43
C. Correction Function	46
1. Trilinear interpolation in cylindrical polar coordinates	46
2. Correcting for Light Response	46

D. Residual Dependence Check	49
VI. Anti-correlation and Time Variation Corrections	52
A. Calibration Sources	52
B. Anti-correlation	52
C. Time variation correction	52
1. Time dependent rotation angle	52
2. Energy Ratio and Time Variation Correction	55
D. Systematics	58
1. Efficiency uncertainty caused by energy scale uncertainty	61
VII. Energy Resolution (Iterative Approach)	62
A. Introduction	62
B. The Iterative Approach	62
1. Description of the Method	62
2. Implementation of the Method	63
3. Results Using Th@S5 Data	64
4. $^{60}\text{Co}$ Cross-check	68
C. Resolution Parameters for $2\nu\beta\beta$ Analysis	68
1. Weekly Resolution	68
2. Average Resolution and Parameters	73
D. Future Work	77
References	78

## I. INTRODUCTION

This TechNote contains all the analysis details of energy calibration and corrections for the EXO  $2\nu\beta\beta$  analysis in Spring, 2013.

## II. GAIN CALIBRATION

### A. Introduction

This document should explain how the U-wire gains were calculated for the Spring 2013 EXO-200  $2\nu\beta\beta$  analysis. It includes descriptions of the methods, the rationale behind those methods, as well as thoughts for future improvement.

There are two main methods for computing the U-wire gains. The first method is based on using charge injection data. Charge injection runs are used to monitor the performance of all the APD and wire channels by injecting specific amounts of charge (electrons) into each channel and measuring the detector response (channel gain, rms and preamp time constants). In this method, absolute U-wire gains were derived from data from the manual external charge injection runs taken just before the  $0\nu bb$  data run began and a select subset of internal charge injection runs taken just before and after the front end electronics cards were installed in the electronics boxes for the  $0\nu bb$  run.

Next, there is pair-production data. Our thorium-228 source decay chain includes the Tl-208 beta decay, which includes a gamma emission at 2614.5 keV. This gamma has sufficient energy to pair produce in the xenon, making an  $e^+e^-$  pair with total kinetic energy 1592.5 keV. This energy deposit is quite similar to double beta decay (it is a pair of betas depositing energy in the xenon), and it is quite localized, as the  $e^+e^-$  pair will deposit its energy in a small volume. This last feature makes it useful for measuring the gain on individual wires. There will also be additional charge deposits from the eventual  $e^+$  annihilation (making two gammas at 511 keV each), but those are ignored for the gain calibration analysis.

The final method used for gain calibration actually combines the strengths of charge injection (low statistical error) with pair production (strong physical basis) to produce a time-varying gain. Additionally, the charge injection data is used to derive measurements of the pre-amplifier shaping times, which are now allowed to vary in time for this analysis.

### B. Absolute Charge Injection Gains

#### 1. Manual External Charge Injection Runs

For the manual external charge injection runs (Table I), the front end electronics cards were removed from the electronics boxes after the  $2\nu bb$  run and placed in an external test enclosure at SLAC. A precision pulser was used to inject specific amounts of charge into each U-wire channel. Within the pulser, a capacitor with a known capacitance of 20 pf ( $\pm 1\%$ ) was charged to a specific voltage and then discharged as a square wave (with a frequency of 600 Hz), and then sent through a 1:1000 attenuator into the channel, where the channel preamp turns the square wave transition edges into positive and negative pulses. During the manual external charge calibration runs, the data acquisition system took data with a random trigger at a rate of 50 Hz, ensuring at least one positive pulse in each frame. Approximately 1500 pulses of amplitudes 0.5 V, 1.0 V, 1.5 V, and 2.0 V were injected into each channel, corresponding to charges of 62,500, 125,000, 185,000, and 250,000 electrons, respectively. For a subset of channels, there is a small correction of 0.10 pf.

#### 2. Internal Charge Injection Runs

For internal charge injection runs, an onboard calibrator circuit (Figure 1) injects a specific amount of charge into each channel (wire and APD). Unlike the manual external charge injection runs, the total capacitance of the calibrator is not precisely known, hence, the injected charge is not precisely known. In this sense, gains measured from the internal charge injection runs are not absolute, but can be used for relative measurements. Referring to Figure 1, the charge,  $Q$ , injected into each channel is given by  $Q = (V_1 - V_2)(C_1/(C_1 + C_2)) \cdot C_3$ . The voltages  $V_1$  and  $V_2$  are determined by resistors and voltage regulators in the circuit, each of which varies  $\leq 50$  ppm/K. The capacitances  $C_1$  and  $C_2$  are approximately 1nF; assuming they are of the same type, the temperature variability of  $C_1$  and  $C_2$  would approximately cancel to first order.  $C_1$  and  $C_2$  are likely X7R type capacitors (which vary about 0.1%/K, with

TABLE I: Manual External Charge Injection Runs

Run Number	Start Time	End Time	Events	Dropped Events	Injected Channels
10000636	2011-09-16 11:26:05	2011-09-16 12:39:25	102,339	0	95-104, 112, 113
10000639	2011-09-16 13:05:47	2011-09-16 13:35:41	19,570	0	105-107
10000641	2011-09-16 15:36:05	2011-09-16 17:36:52	132,892	7,632	76-82, 105-111
10000643	2011-09-16 17:51:51	2011-09-16 19:05:35	147,829	1,560	83-94
10000645	2011-09-16 19:20:16	2011-09-16 19:49:17	65,166	947	25-30
10000646	2011-09-17 06:33:01	2011-09-17 07:03:12	55,928	345	19-25
10000649	2011-09-17 07:19:27	2011-09-17 07:53:51	66,461	2,564	2-4, 31-37
10000660	2011-09-17 08:48:48	2011-09-17 09:05:35	34,713	956	4-8
10000662	2011-09-17 09:20:16	2011-09-17 09:36:43	33,693	1,743	9-12
10000668	2011-09-17 10:21:31	2011-09-17 10:37:48	30,919	2,271	12-15
10000671	2011-09-17 10:45:15	2011-09-17 11:05:02	33,721	2,671	0, 1, 17, 18
10000688	2011-09-18 17:41:05	2011-09-18 17:51:01	21,059	793	16,17

hysteresis), so we'll need to consider second order effects in a future study.  $C_3 = 1\text{pF}$  and it's typically a NP0 type capacitor for small value surface mounts; its capacitance varies by 30 ppm/K. In total, the internal charge calibrators should be stable to about 100-200 ppm/K.

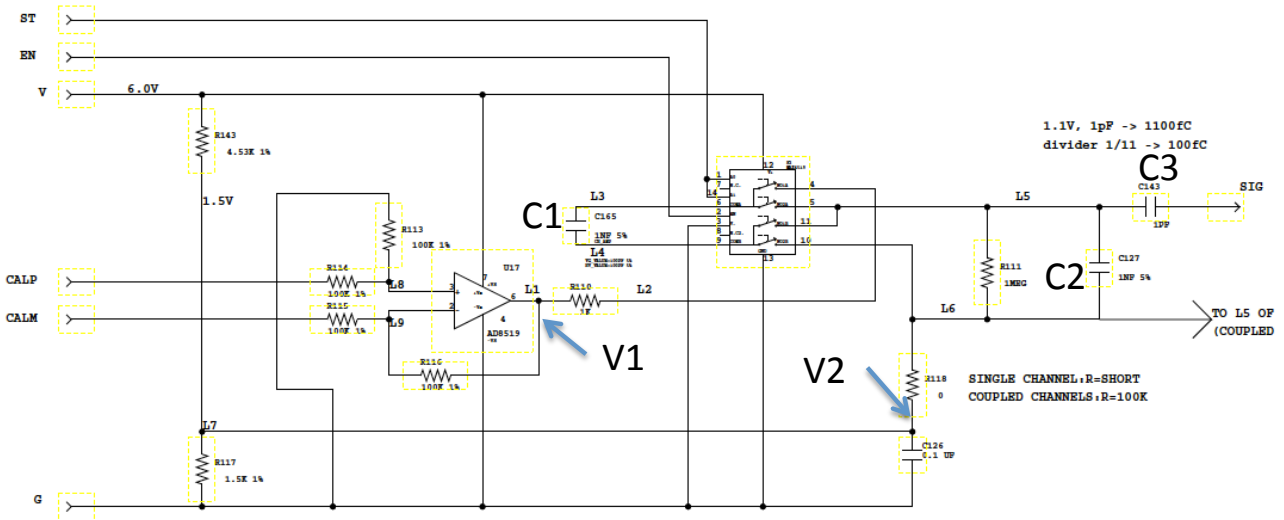


FIG. 1: Schematic of the on-board charge calibration circuit.

For internal charge injection runs, 33 different amplitude pulses are injected into each channel, at 400 pulses per amplitude. The internal charge injection runs are very important for monitoring the trending behavior of the channel gains, rms, and preamp time constants, since these measured quantities are sensitive to environmental (e.g., temperature) and hardware (e.g., equipment deterioration, electronic loads, etc.) changes. The internal charge injection runs used in this analysis are listed in Table II.

TABLE II: Internal Charge Injection Runs

Run Number	Start Time	End Time	DAC Count	Pulse Count	Injected Channels
10000637	2011-09-16 12:41:07	2011-09-16 12:50:30	33	400	95-104, 112, 113
10000642	2011-09-16 17:38:21	2011-09-16 17:48:03	33	400	76-82, 105-111
10000644	2011-09-16 19:06:54	2011-09-16 19:16:39	33	400	83-94
10000647	2011-09-16 07:04:24	2011-09-16 07:14:12	33	400	19-30
10000661	2011-09-17 09:07:01	2011-09-17 09:17:01	33	400	2-8, 31-37
10000689	2011-09-18 17:53:46	2011-09-18 18:03:31	33	400	0, 1, 9-18
2380	2011-09-24 07:26:36	2011-09-24 07:36:10	33	400	All U and V-wires

### 3. Charge Injection Pulse Fitting

Each U-wire signal is shaped in 5 stages: the signal is first passed through two integrators with time constants of  $1.5 \mu\text{s}$  each, then through two differentiators with time constants of  $40 \mu\text{s}$  each, and finally through one last differentiator (the preamp) with a time constant of  $60 \mu\text{s}$ . Each of the shaping stages can be conveniently modeled by a Laplace transform, such that the final shaped signal,  $f(t)$ , is given by

$$f(t) = a^2 \left( - \left( \frac{b(b^2 + ba - 2ac)}{(b-a)^3(b-c)^2 e^{bt}} \right) + \frac{a(a^2 + ba - 2bc)}{(b-a)^3(a-c)^2 e^{at}} \right. \\ \left. + \frac{c^2}{(b-c)^2(a-c)^2 e^{ct}} - \frac{b^2 t}{(b-a)^2(b-c)^2 e^{bt}} - \frac{a^2 t}{(b-a)^2(a-c)^2 e^{at}} \right), \quad (1)$$

where  $a = 1/1.5\mu\text{s}$ ,  $b = 1/40\mu\text{s}$ ,  $c = 1/60\mu\text{s}$ , and  $t$  is the time measured since the start of the signal. An example of a U-wire waveform from a manual external charge injection run containing a few charge injection pulses along with a fit to a positive pulse is shown in Figure 2.

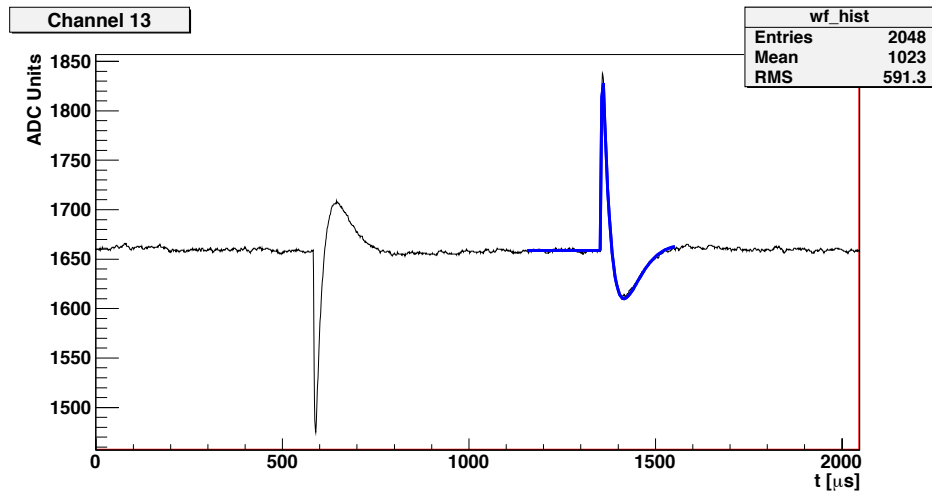


FIG. 2: Manual charge injection U-wire waveform (black line) with a fit to a positive pulse (blue line) for channel 13.

The analytical pulse model (Eq. (1)) has 6 input parameters, which are allowed to either float or remain fixed during the pulse fitting:

1. Amplitude of square wave used to generate pulse [floated]
2. Signal time [floated]
3. Integration time [fixed]
4. Differentiation time [fixed]
5. Preamp differentiation time [floated]
6. Baseline [floated]

For each fitted pulse, we use the returned values for the fitted parameters listed above and generate a function template using the analytical model (Eq. (1)) and a  $0.1 \mu\text{s}$  time spacing. We then find the maximum value of the function template, corresponding to the fitted amplitude of the charge injection pulse. When the manual external fitted pulse amplitudes are binned, four distinct distributions corresponding to the four different voltages used in the pulser are displayed (see Figure 3). Likewise, when the internal fitted pulse amplitudes are binned, 33 distinct distributions corresponding to the 33 different amplitudes are displayed.

### 4. Gains

*a. Uncorrected Gains* The gain is defined as the ratio of the amount of injected charge to the measured number of analog-to-digital counts (ADC):

$$\text{Gain} = \frac{\text{Injected Charge}}{\text{Number of Counts}} \text{ [electrons/ADC].} \quad (2)$$

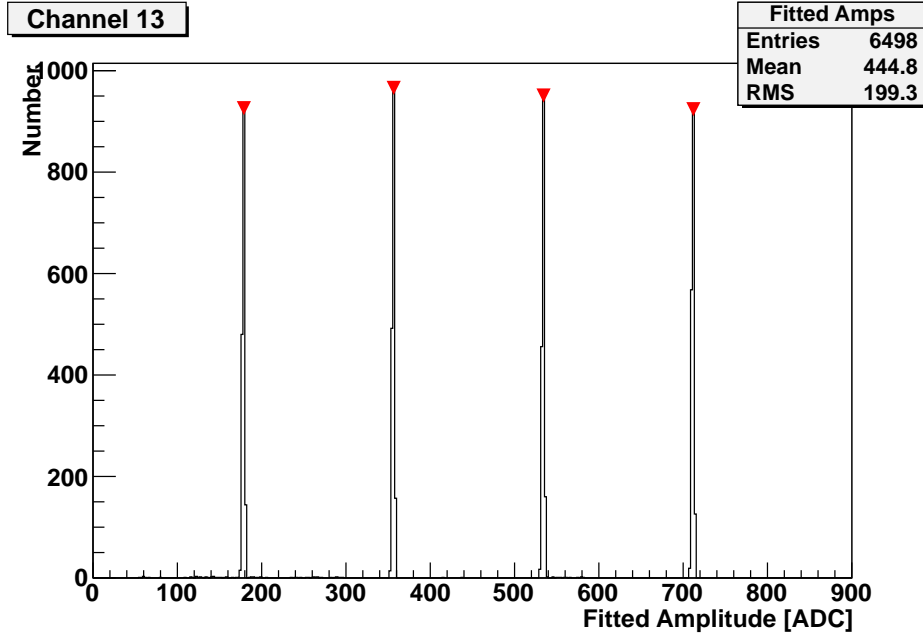


FIG. 3: Fitted pulse amplitudes for channel 13. The red markers indicate the centers of each individual distribution.

For the manual external charge injection runs, plotting the mean of each of the four fitted pulse amplitude distributions (e.g., Figure 3) vs. the injected charges and fitting a line to the data using ROOT’s MINUIT routine, the gain and gain error are obtained from the slope and error on the fitted slope, respectively (see Figure 4). These manual gain values are “uncorrected”, since they are measured when no external loads were attached to the channel; they are corrected using multiplicative correction factors derived from the internal charge injection runs listed in Table II. The gains from internal charge injection runs taken when the front end cards are in the electronics boxes are derived in a similar manner, although no correction factors are needed.

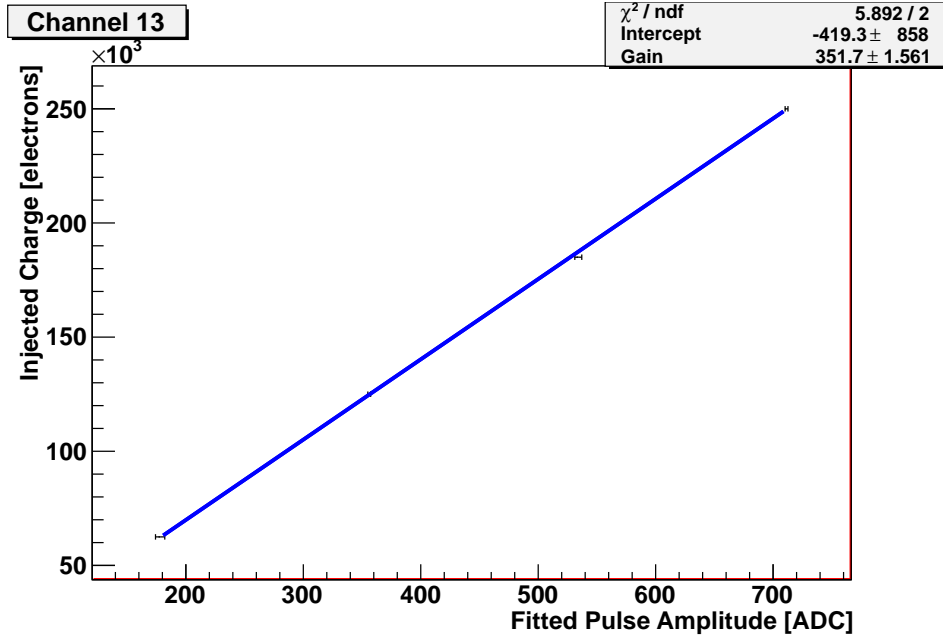


FIG. 4: Gain for channel 13. The blue line represents the linear fit to the data points (black).

*b. Manual Gains Correction Factors* In order to account for temperature effects and the electronic loads of the TPCs when attached to each channel, we derive unit-less multiplicative correction factors,  $C$ , for each channel, defined by

$$C = \frac{\text{Internal Gain "Inside"}}{\text{Internal Gain "Outside"}},$$

or the ratio of the gain from the internal charge injection run performed just after the front end cards were installed (i.e., “inside”) to the gain from the internal charge injection run performed while the cards were still in the external test enclosure (i.e., “outside”); these factors are plotted in Figure 5. Most of the correction factors are small ( $\sim 0.5\text{--}1.0\%$ ), but some channels (e.g., channels 2, 5, 7, 34, 37, 85) have larger corrections of approximately 5%–10%.

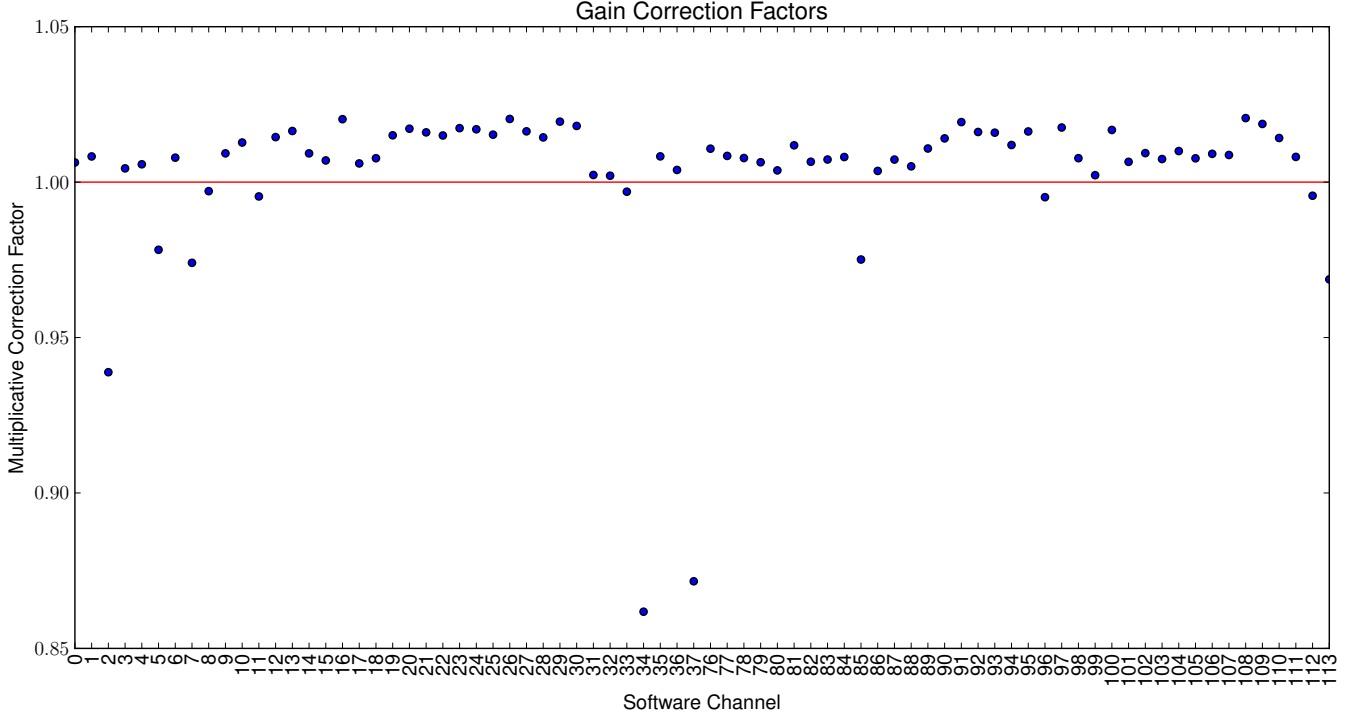


FIG. 5: Correction factors for each U-wire channel. The red horizontal line represents a correction of 1.0 (no correction)

*c. Corrected Gains* For each channel, the uncorrected manual gain is multiplied by its corresponding correction factor to produce a corrected, absolute gain value. The absolute gains are listed in Tables III and IV.

TABLE III: Charge Injection U Wire Gain Information

Channel	Uncorrected Gain [e <sup>-</sup> /ADC]	Correction Factor	Corrected Gain [e <sup>-</sup> /ADC]	Gain Error [e <sup>-</sup> /ADC]
0	347.20	1.006316	349.40	0.54
1	348.13	1.008261	351.01	0.57
2	449.80	0.938852	422.30	0.97
3	423.70	1.004423	425.57	0.85
4	411.01	1.005737	413.37	0.81
5	437.08	0.978229	427.56	0.93
6	413.62	1.007867	416.87	0.77
7	430.98	0.974044	419.79	0.91
8	408.08	0.997095	406.89	0.78
9	342.62	1.009251	345.79	1.12
10	355.09	1.012740	359.62	0.57
11	355.56	0.995397	353.93	0.53
12	340.86	1.014482	345.80	0.54
13	350.97	1.016446	356.74	0.51
14	358.97	1.009251	362.29	0.60
15	351.67	1.006968	354.12	0.55
16	356.13	1.020246	363.34	0.48
17	366.41	1.006013	368.61	0.71
18	350.11	1.007683	352.80	0.54
19	410.98	1.015061	417.17	0.75
20	405.49	1.017182	412.46	0.81
21	405.55	1.016008	412.04	0.79
22	417.30	1.015003	423.56	0.85
23	411.98	1.017363	419.14	0.79
24	413.33	1.016995	420.35	0.78
25	439.39	1.015271	446.10	0.86
26	408.54	1.020320	416.85	0.79
27	413.19	1.016336	419.94	0.80
28	413.59	1.014385	419.54	0.76
29	427.68	1.019457	436.00	0.85
30	415.69	1.018076	423.21	0.81
31	426.50	1.002297	427.48	0.85
32	408.22	1.002062	409.06	0.76
33	411.42	0.996922	410.16	0.80
34	439.99	0.861801	379.18	0.99
35	420.69	1.008282	424.18	0.75
36	428.53	1.003921	430.21	0.83
37	462.62	0.871591	403.22	1.08

TABLE IV: Charge Injection U Wire Gain Information (Cont.)

Channel	Uncorrected Gain [e <sup>-</sup> /ADC]	Correction Factor [%]	Corrected Gain [e <sup>-</sup> /ADC]	Gain Error [e <sup>-</sup> /ADC]
76	324.15	1.010760	327.64	0.54
77	330.24	1.008435	333.03	0.55
78	330.59	1.007750	333.15	0.56
79	337.89	1.006389	340.05	0.57
80	331.73	1.003775	332.98	0.73
81	337.59	1.011837	341.59	0.59
82	346.16	1.006554	348.43	0.56
83	345.93	1.007271	348.44	0.59
84	345.47	1.008079	348.26	0.55
85	336.97	0.975099	328.58	0.54
86	345.87	1.003608	347.12	0.58
87	341.20	1.007261	343.67	0.59
88	345.84	1.005076	347.59	0.60
89	354.15	1.010819	357.98	0.58
90	340.18	1.014071	344.97	0.51
91	342.64	1.019317	349.26	0.53
92	346.67	1.016130	352.26	0.57
93	356.33	1.015911	362.00	0.59
94	352.53	1.011941	356.74	0.58
95	397.72	1.016300	404.21	0.79
96	421.34	0.995151	419.30	0.94
97	395.92	1.017570	402.88	0.70
98	403.45	1.007700	406.56	0.84
99	419.70	1.002232	420.64	0.85
100	412.96	1.016782	419.89	0.84
101	428.64	1.006527	431.44	0.89
102	414.99	1.009334	418.87	0.80
103	412.26	1.007425	415.32	0.82
104	404.31	1.009997	408.35	0.80
105	336.40	1.007659	338.97	0.74
106	336.94	1.009104	340.00	0.59
107	335.15	1.008726	338.07	0.51
108	341.98	1.020601	349.02	0.58
109	321.35	1.018717	327.36	0.49
110	319.83	1.014194	324.37	0.52
111	327.29	1.008118	329.95	0.54
112	407.50	0.995622	405.72	0.87
113	415.36	0.968724	402.37	0.90

### C. Shaping Times and Time Variation

A significant motivation for updating the gain calibration is the concern that the electronics performance will vary with environmental factors, such as temperature. There is some evidence that the temperature of the front end electronics modifies the gains (based on the times when the electronics fans are turned on, and later reversed). This temperature dependence appears to be correlated with the pre-amplifier shaping times, as measured by internal charge injection (as described in Section II B 3). While the amount of charge injected may be affected by temperature, the measurement of the differentiation time is done based on the ADC timing, which should be stable, so we consider this measurement to be very reliable. Figure 6 shows the shaping time measurements from internal charge injection runs over the relevant data period (Sept. 22, 2011 through April 15, 2012, hereafter called run 2a) and somewhat beyond. Clear shifts can be seen at the indicated points, when the fans are first turned on, and when they reverse direction. A corresponding plot for gain measured from internal charge injection is shown in Figure 7.

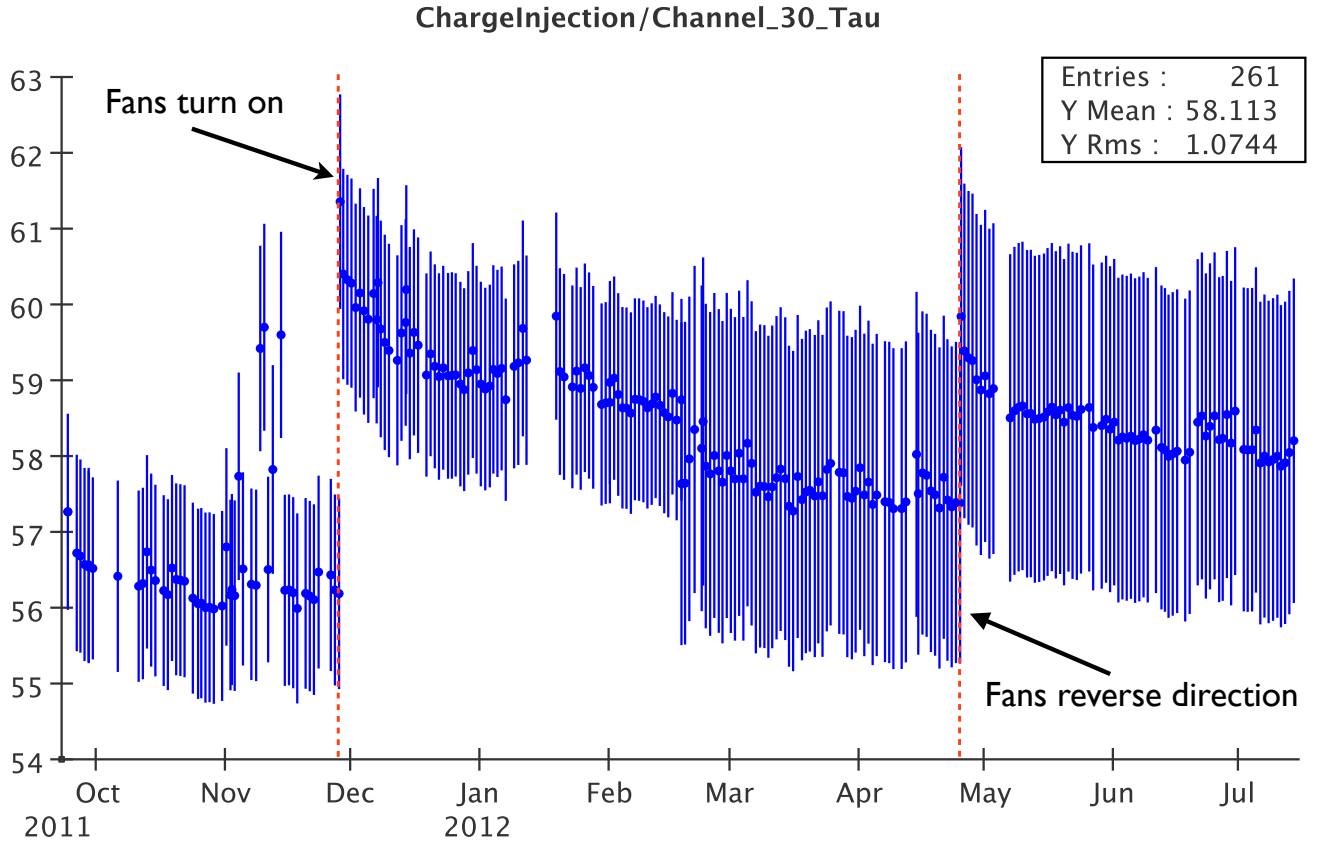


FIG. 6: Shaping times measured from internal charge injection for U-wire channel 30. The times when the fans were turned on and reversed are marked. Similar patterns are seen for other channels.

#### 1. Principle

The shaping times used should have a small, but potentially noticeable effect on the gain measurements. Thus, it is necessary to calibrate the shaping times before calibrating the gains. The internal charge injection runs are used to get information on the shaping times. It is expected that these values should be unbiased by environmental factors.

Overall, the shaping times are relatively stable. Figure 6 shows the variation over time to be around 7% peak to peak (for that particular channel). Studies showed that this shaping time variation did not have a large effect on the gain measurement, though it did have some effect. The shaping times are only applied during the “reconstruction” phase of data processing, when the signal waveforms are measured.

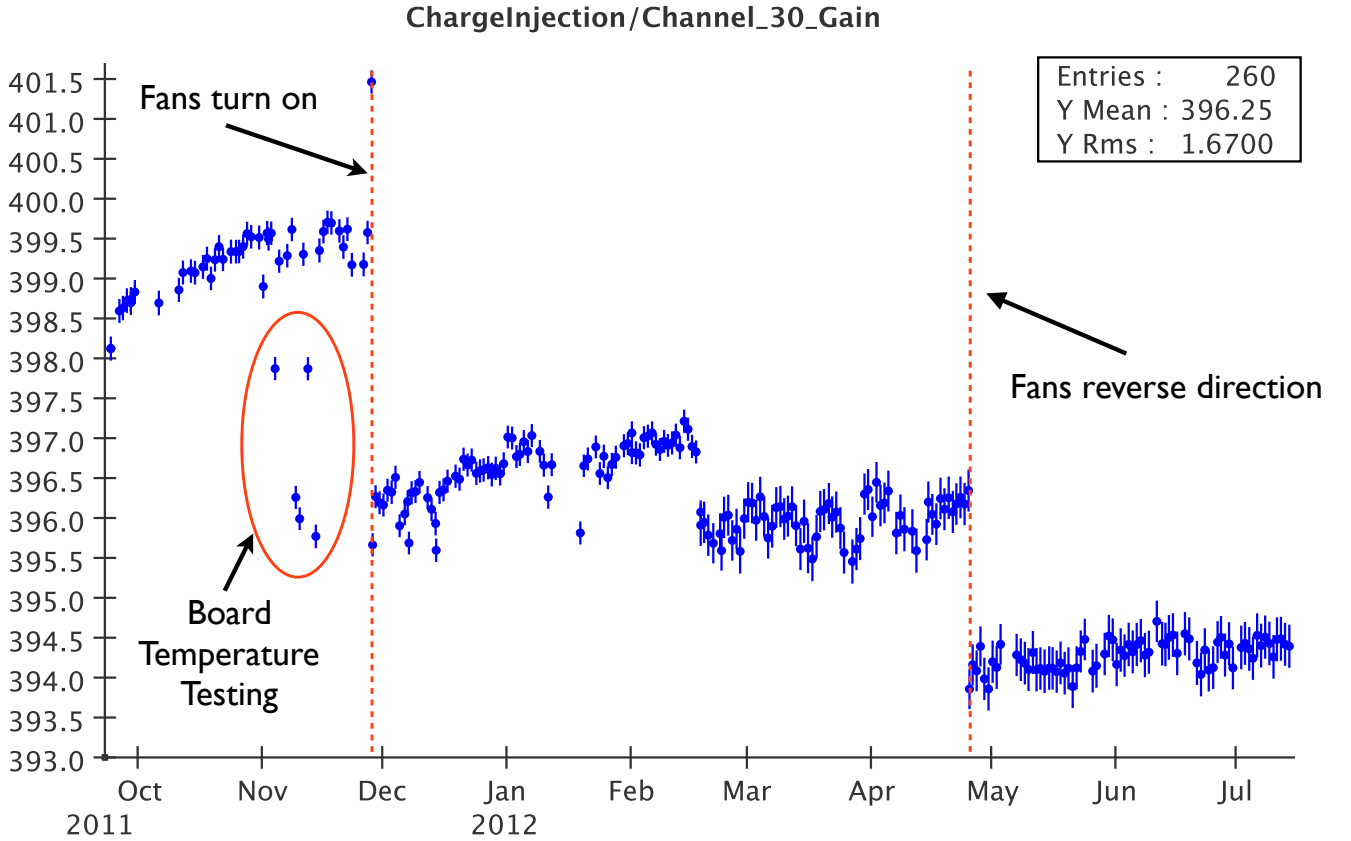


FIG. 7: Gains measured from internal charge injection for U-wire channel 30. The times when the fans were turned on and reversed are marked. Note the runs in November where some board temperature testing work may have changed the gains. This work is mentioned in the working document 2. These runs were included in the gain measurement studies here, but we may wish to exclude them for future analyses.

## 2. Selected Time Periods

As this time variation to shaping time was first implemented by hand, a simple set of time periods was desirable. The times when the electronics fans change needed to be among the divisions between periods. The selection of 6 time periods is shown in Figure 8. With the exception of the start of November, each time period boundary is selected to line up with a physical event for the system:

- Start of data period
- Start of November
- Box 1 fans turned on (Nov. 28)
- Box 2 fans turned on (Dec. 4)
- January power outage (long break in data)
- Start of unified internal charge injection (APD + wires, previously they were separate)
- End of data period

In the future, when this analysis is automated, and shaping times and gains are put into the database without human intervention, we will likely move to more regular time periods, perhaps with some manual times set for major changes. But for now, these are our time periods for run 2a data. Note that the fan direction reversal occurs outside of the data period. These same time periods are used for both shaping time variation and gain variation.

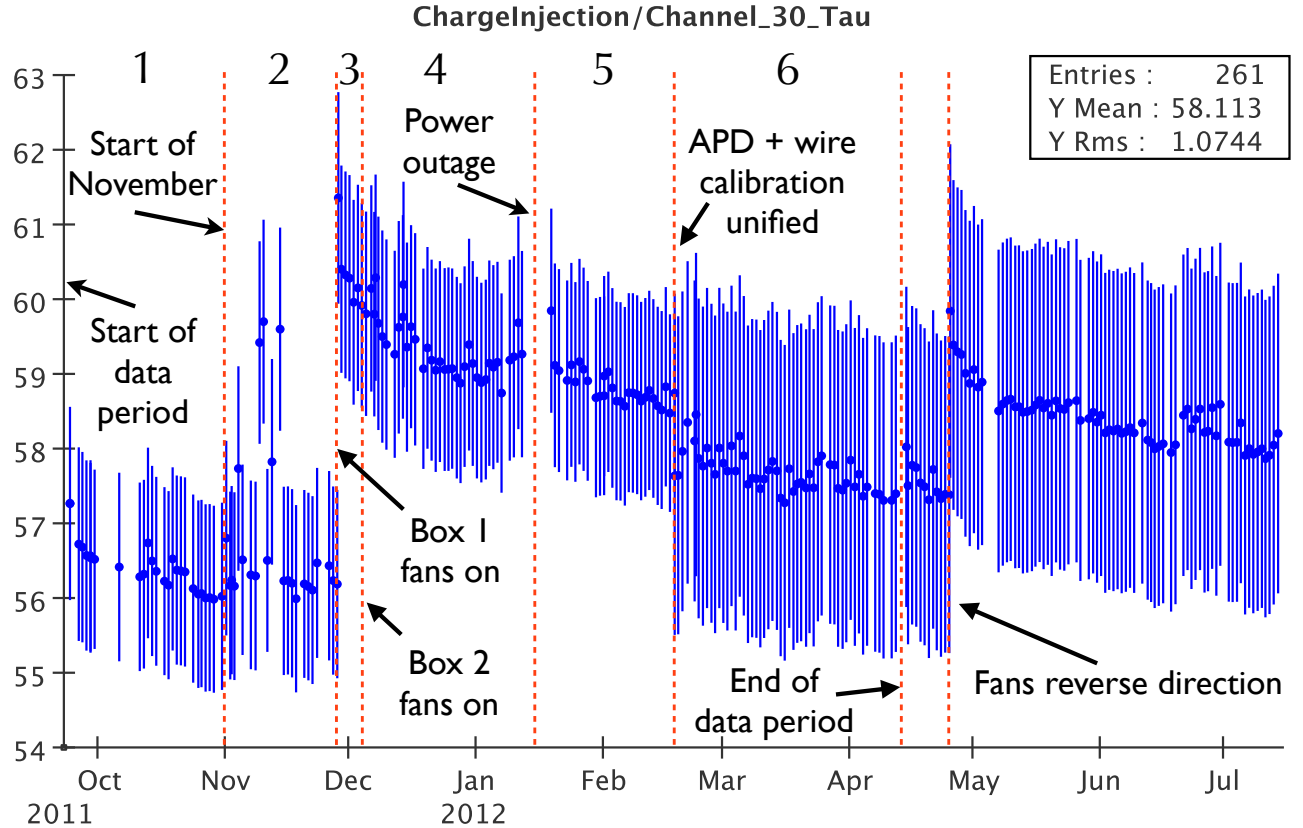


FIG. 8: The channel 30 shaping time (same as Figure 7), but with all of the calibration time periods marked above each period (numbers 1-6). Each period boundary is also marked.

### 3. Implementation

The shaping times (as well as internal charge injection gains) are read in from trending files produced in the finish-up scripts. This method was quick and easy, but is susceptible to problems if the finish-up scripts malfunction, or if ongoing processing is happening (and writing these trending files while they are being read). All charge injection runs which properly produced a trending file were selected, excepting a manual bad run list. For the shaping times used for this analysis, the manual bad run list only included only runs 2852 and 4848, which are listed as "BAD" in the run history. For future analyses, when the system is automated, this should be reconsidered.

Within each time period, all selected charge injection runs have their shaping times averaged together to get a mean shaping time. If a trending file has a gain or shaping time of zero or less for any channel, or if there is no gain or shaping time for that channel, then that run is ignored for that channel. This is especially important to avoid bias during the period where channel 16 was turned off.

A graph of the mean shaping times for each time period is shown in Figure 9. The shaping times do not vary very much, and, when they do vary, they largely vary together (all channels increase or decrease together). One exception is in the period when fans were running in one e-box, but not the other. However, it does not appear that this had a significant effect on the energy resolution.

These new shaping times have been put into the calibrations database, under the flavor name timevartau (for time varying tau (shaping time)). After running reconstruction using these new shaping times (the dump-database script was used to enable this testing before the gains were put into the online calibration database), no significant problems were noticed, and so these gains should be put into use for this analysis.

When using the timevartau flavor for dates before the run 2a data period, the "vanilla" or "measured\_times" shaping times are defaulted to. For dates after the run 2a period, an averaged shaping time from that later period is used, extending from April 15, 2012 through over a year after that (although the exact stopping time is not precisely known). The automated shaping time measurement should be set up before moving on to analyze that later data.

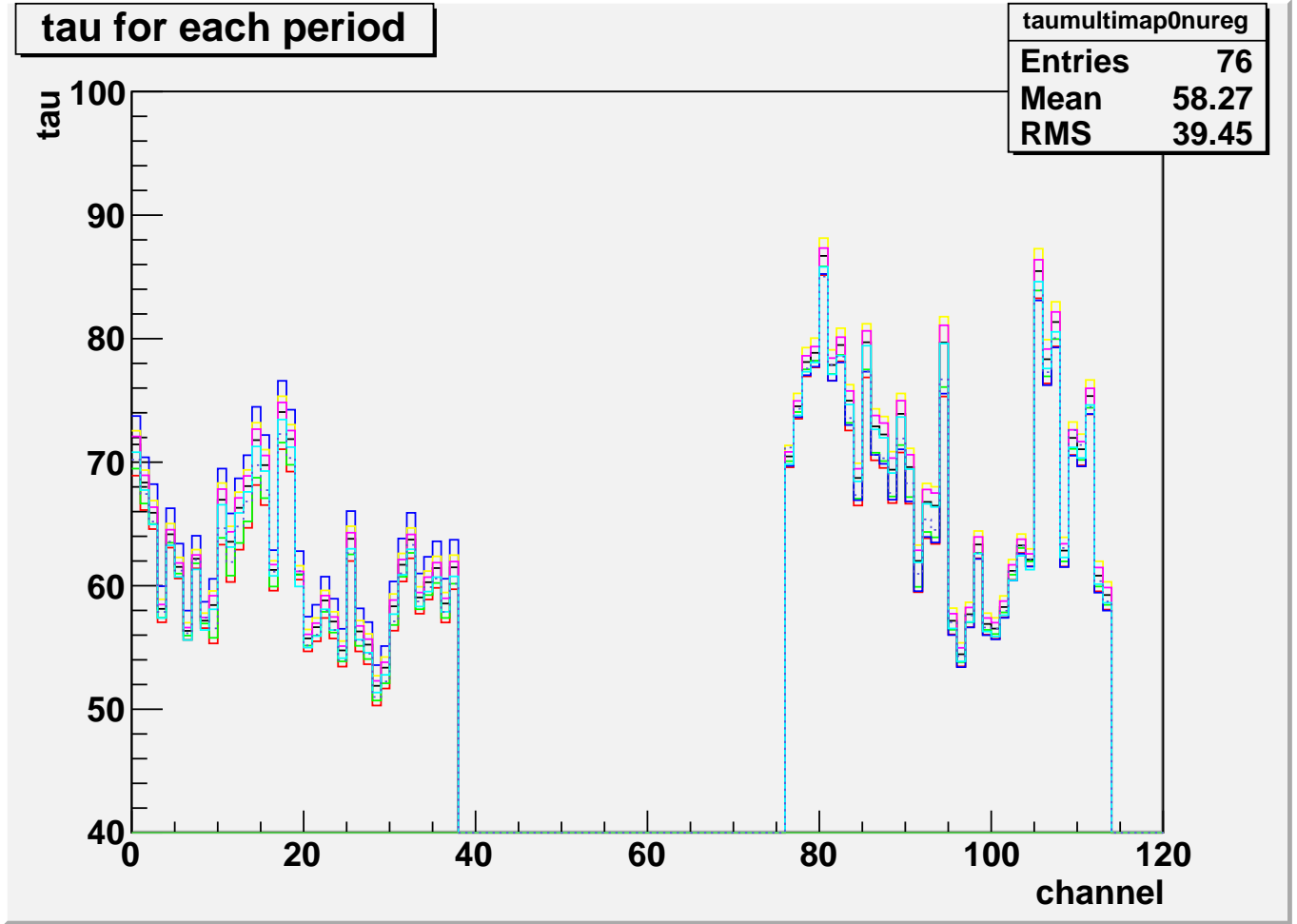


FIG. 9: Shaping times measured from internal charge injection for each time period, for each U-wire channel. The colors for time periods 1 through 6 are red, green, blue, yellow, magenta, and cyan, respectively. Additionally, the mean for all 6 time periods is drawn in dashed purple. The gap in the middle is for V-wires.

#### D. Time Varying Gain Correction

The final gain measurement for this analysis is a combination of an absolute gain from the pair production peak, and a time variation derived from internal charge injection. This charge injection time variation function is actually used before the pair production gains are computed, so it will be described first.

In a way analogous to the shaping times, time varying gains are derived from the internal charge injection runs, using the same time periods, and the same averaging method. Additionally, an average gain for the entire run 2a data period is produced. A set of gain time varying gain corrections is then produced, with the correction for the time period  $i$  defined as  $C_i = G_i/G_{\text{avg}}$ . These corrections will be applied for pair production gains. The time variations in relative gains between channels are much more important than the overall absolute gains, because the energy scale will get corrected during the processing chain.

The internal charge injection gain corrections are shown in Figure 10.

#### E. Pair Production Gains

##### 1. Physics

The Tl-208 peak pair production events have multiple features: possible charge deposits for each of the 511 keV gammas produced when the positron annihilates, and one charge deposit for the electron and positron ionization, the

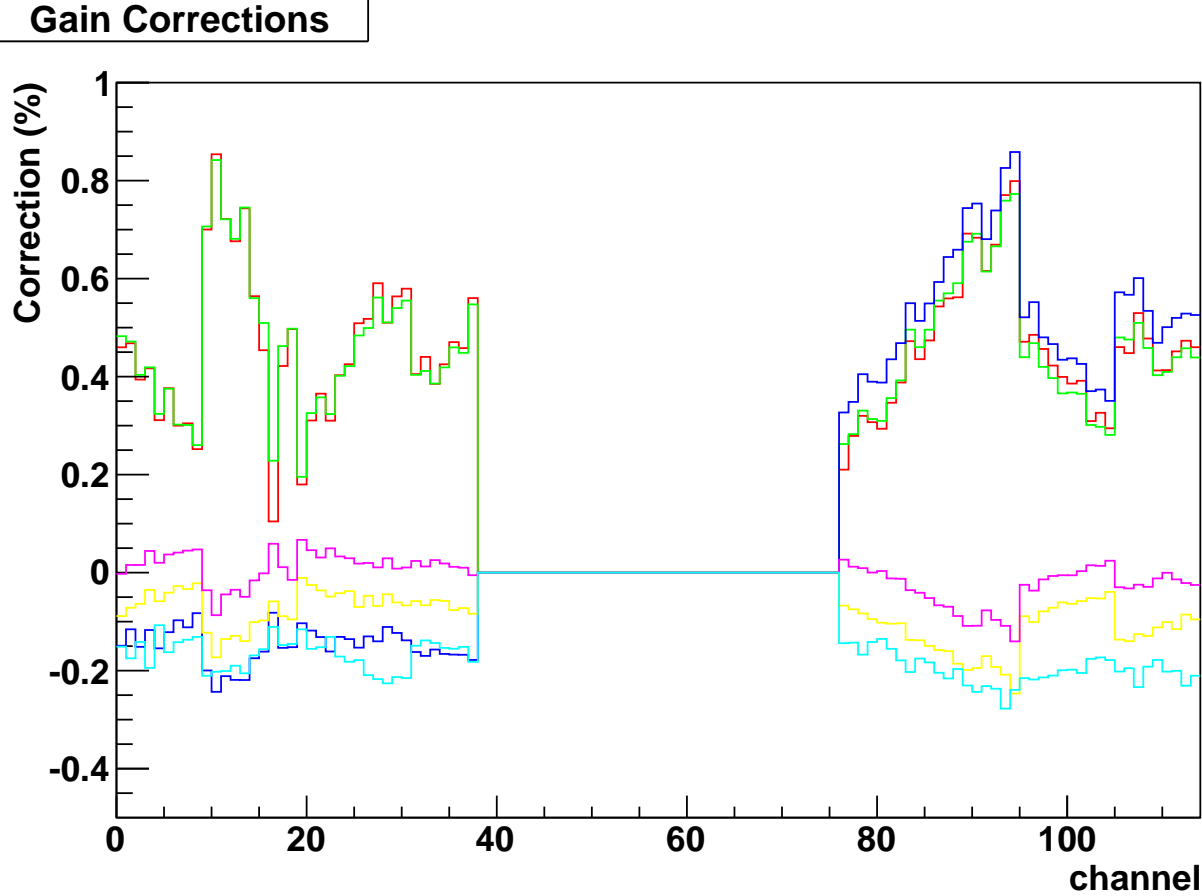


FIG. 10: Gain corrections for each channel for each of the six time periods, as derived from internal charge injection gains. The colors are red, green, blue, yellow, magenta, and cyan, for periods 1 through 6, respectively. Note that for nearly every time period, the gain correction is at roughly the same value: the channels all change together. The obvious exception is period 3 (blue), where the fan for electronics box 1 was on, but the fan for electronics box 2 was off. All gain corrections are at or below the  $\pm 1\%$  level.

so-called “double escape peak”. This peak shows up well in single-site data, looks like a double beta decay, and can be found in sufficient statistics for calibration for each wire. These characteristics add up to make it a very useful wire gain tool. In an ideal world, the two “escaped” gammas could have their charge deposits included to make a more positive identification of a pair production event. In this scheme, the fact that the gammas must be produced back to back (assuming the positron is at or near at rest, a reasonable assumption) is used to make a geometric cut: three charge clusters in a line.

In practice, this cut is not very useful for gain correction. Due to the small size of EXO-200, it is quite easy for at least one of the escaping gammas to exit the fiducial volume entirely without leaving a charge deposit. An attempt was made to apply this geometric cut (require at least three charge clusters, and require the angle formed by three of them to have  $\cos \theta \geq 0.9$ ). This cut the statistics (both the pair production peak and background) by more than half, with only a very modest improvement in signal/background ratio. While this method may be interesting and useful for getting a purer sample, statistics are essential for the gains measurement, so the geometric cut was dropped from the requirements.

## 2. Data selection

There are two steps to this. First, is the selection of runs to use. Next is the selection of charge clusters within those runs.

The source run selection was not automated, and in fact was done by hand by Liangjian. Only thorium source runs

in run 2a were selected. Both strong thorium and weak thorium source runs were used. Bad runs were excluded. For the future, a more automated selection method should be found.

The simple requirements for selecting charge clusters for the gain measurements are:

- scintillation cluster time  $< 1.92 \mu\text{s}$  (avoid events near the end of the data frames)
- charge cluster  $z$  position:  $-170 \text{ mm} < z < 170 \text{ mm}$
- charge cluster  $z$  position:  $|z| > 10 \text{ mm}$
- charge cluster  $y$  position:  $y > -500 \text{ mm}$  (rejects clustering error events)
- charge cluster only leaves signals on one U-wire.

These very basic cuts reject events in regions of the detector where the grid correction becomes important (near the anodes), and keep as many events as possible otherwise. They are nearly unchanged from the cuts used in the previous analysis (though the rejection of failed clustering events is new). Cuts on events near the teflon are intentionally not implemented, as we need good statistics on all wires, including the outside ones.

### 3. Fitting the Peaks

The above described selection cuts are applied to data which has been reconstructed and processed with new shaping times. It is necessary to use some kind of gain as a starting point, so pure internal charge injection gains were used. These gains are not optimal for use, but the corrected manual gains were not available at the time, and the exact starting gains are not very important. We needed a set of gains that were “unbiased” (so we could not use the results of the previous campaign), and having gains relatively close to the final values makes the fitting easier. For future analyses, we suggest the corrected manual charge injection gains. We have, however, applied the time dependent gain corrections (described in Section II D). The time dependent gain corrections do not alter the mean gain, and it was shown in some test studies that the pair production peak positions did not change significantly with or without the time variation. The astute reader will notice that the mean charge injection gain with the time variation correction applied, will simply yield the time varying internal charge injection gains.

The purity corrected energy for each charge cluster passing the cuts is put into a histogram for its wire. This energy includes the purity correction (for electron lifetime) as well as the gain correction and grid correction, but not the light map (which would be irrelevant for a charge only measurement anyway). The purity correction used was an older version, and not the final one for the analysis. The difference between the purity used for the gain measurement and the final purity will manifest as a change in the charge peak position. Each wire has only one histogram for the entire data period (it is not divided into time periods like the charge injection data).

After the energy histograms are filled, they are fitted to a decaying exponential summed with a gaussian. This has a total of five free parameters, though we are really only interested in the gaussian peak position. This fitting is a two-step process, with a first fit to find roughly where the peak is, and a second fit to refine it, within the constraints set by the first fit. This process is sensitive to initial conditions, and should be validated to make sure it has worked properly. Examples of these pair production peak fits are shown in Figure 11. These show an example wire with good statistics and an example wire with poor statistics.

The wire gains are then derived from these fitted peaks, by correcting the initial gains used, as follows.

$$G_{\text{new}} = G_{\text{old}}(1592.51 \text{ keV}/E_{\text{pp}}) \quad (3)$$

where  $G_{\text{new}}$  is the new gain to be used,  $G_{\text{old}}$  is the gain used for this study (the internal charge injection gains, full run 2a mean value), and  $E_{\text{pp}}$  is the fitted pair production peak energy. The gains before (pure internal charge injection gains) and after (pair production gains) the correction factors are applied are shown in Figure 12.

These new gains can then be modified with time variation correction values (Figure 10, to produce gains for each of the six time periods. These gains are shown in Figure 13. These gains were added to the database under the flavor “pp\_sourcecal\_ci\_timevar\_2a”. The constant pair production gains (with no charge injection time variation) are set to flavor “pp\_sourcecal\_const\_2a”. For “pp\_sourcecal\_ci\_timevar\_2a”, the gains for before the run 2a period default to their old values, and the gains for the last run 2a time period are applied for the remainder of data, beyond run 2a.

A comparison of wire gains from corrected manual charge injection and pair production (both without time variation) are shown in Figure 14.

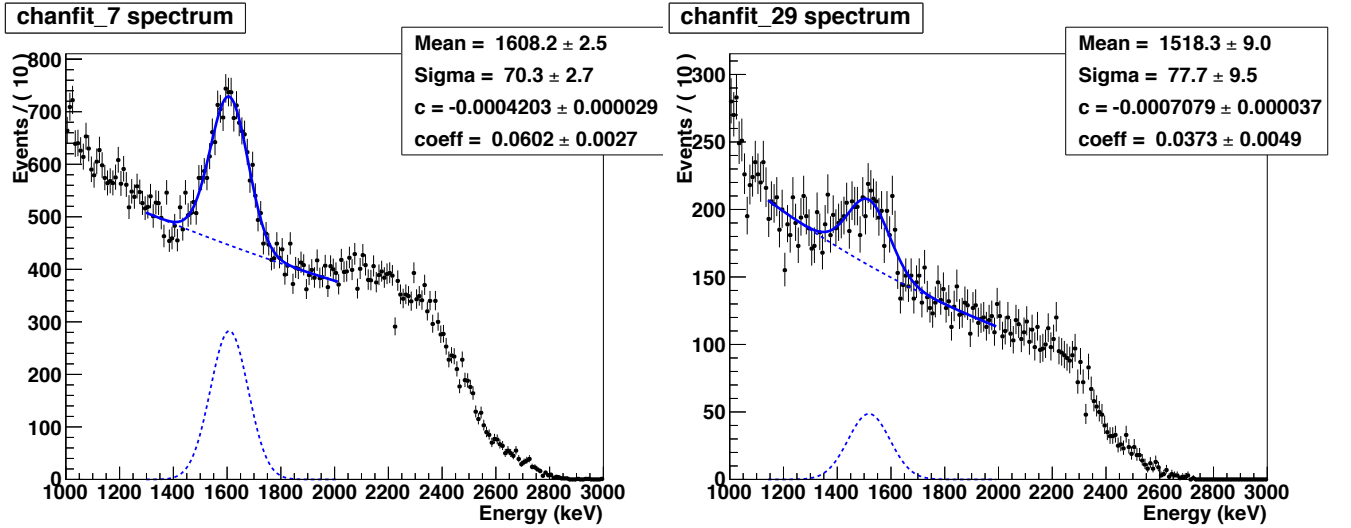


FIG. 11: Fits of the pair production peak for two of the channels. Channel 7 (left) was selected as an example of a fit with good statistics. Channel 29 (right) was selected as an example with bad statistics. The difference in statistics is likely due to proximity of the wire to the sources, mostly source position S5, but also S8, to a lesser extent. Note the exponential decay background and gaussian signal peak in the fit.

## F. Gain Validation and Other Tests

### 1. Validation

After each stage of refinement of the shaping time and gain measurement, the gains have been validated by looking at the resolution (and, to a lesser extent, position) of the Tl-208 photopeak. This peak is independent enough from the pair production peak to be a valid cross-check.

Note that this peak is checked only for the ionization channel. Weekly energy correction is added to the rotated energy. Thus, it is expected that the photopeak here may not exactly line up with the expected value. However, the resolution is still a relevant parameter. To avoid problems due to drifting of calibration parameters over time (and to measure them), the photopeak is fitted separately for each week of data. For the photopeak, only weak thorium runs are used. The exact run list was compiled for the energy correction calibration by Liangjian, and rejects runs with poor purity. It does not match the run list used for the gain calibration.

The resolution is fitted using the same method as is used for energy scale correction (error function plus gaussian). A couple example fits are shown in Figure 15. The primary measure of “goodness” for the gains is the average resolution. Here, the fitted resolution is found for each of the 30 weeks. The resolution for each of the weeks is averaged together, with each week’s contribution inversely proportional to the uncertainty on the resolution. The positions and resolutions from the Tl-208 peaks for each week are shown in Figure 16.

A table of average resolutions for various gain conditions is shown in Table V.

TABLE V: Mean resolutions for various gain conditions. Note that all of them, except for the charge injection cases, are entirely within uncertainty of each other. The first four cases were tested while computing gains, and feature the old purity measurements. The last row’s data was checked during validation of the new data processing, and uses the new purity measurements.

Conditions	SS Resolution [%]	MS Resolution [%]
p.p. gains with c.i. time variation	$3.50 \pm 0.06\%$	$4.19 \pm 0.03\%$
constant p.p. gains	$3.51 \pm 0.06\%$	$4.19 \pm 0.03\%$
const. corrected manual c.i. gain	$3.62 \pm 0.06\%$	$4.26 \pm 0.03\%$
old shaping times/old gains	$3.52 \pm 0.06\%$	$4.17 \pm 0.03\%$
All new calibration, p.p. gains with c.i. time variation	$3.51 \pm 0.06\%$	$4.17 \pm 0.03\%$

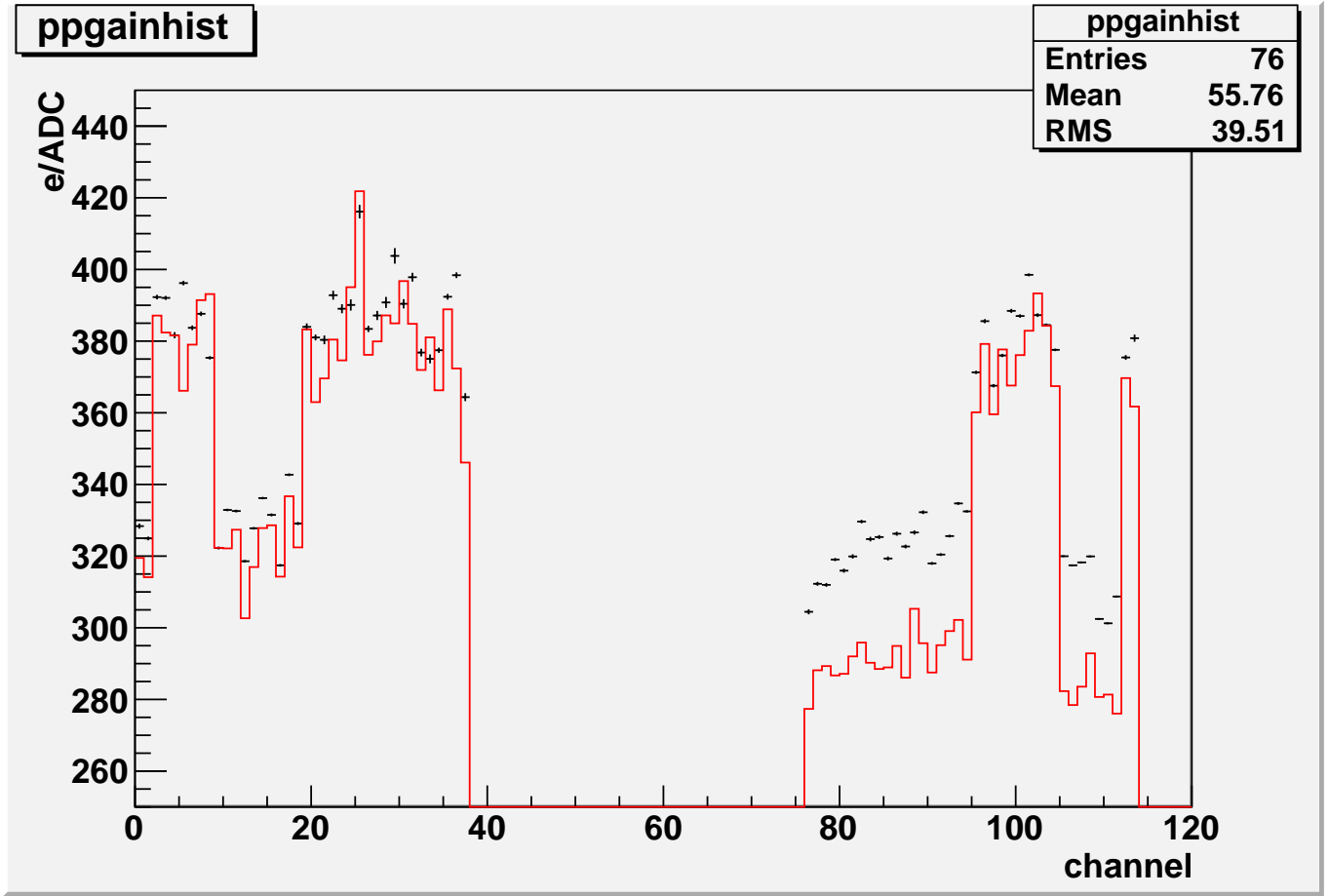


FIG. 12: Comparison of gains from internal charge injection (red line) and pair production (black points with error bars). The difference between these is the gain correction factor.

## 2. Other Tests

A major goal of this exercise was to improve the energy resolution. Thus, various techniques for producing gains were attempted. The gains were produced with and without time variation, with pair production and charge injection, and with and without the new shaping times. The main conclusion of these tests was that the energy resolution was almost entirely unaffected by any of these changes. The only difference that had an effect above the uncertainty was that the pair production based gains give a slightly better energy resolution than the charge injection based gains. Table V summarizes this nicely.

Additional study was given to the charge injection runs in November, 2011, which yield gains which are significantly different from the adjacent runs. The “November” time period has the largest variation in shaping time and gain of all the periods. The relevant runs are not marked as bad in the run history (they are 2 untagged, 2 suspect, and 1 good). It is also not clear whether any source or data runs in that time period were also affected by tests on the electronics temperature. Some of this temperature work involved reducing the clean room temperature, other involved leaving the DAQ electronics off for an hour prior to the charge injection run to give it time to cool. These runs should likely be removed for future work on calibration.

There were a couple investigations towards improving the pair production event selection, both were unable to find useful avenues to improvement. First, there was the usage of the annihilation gammas to make a geometric cut, described in Section II E 1. Next, there was a check of whether the scintillation light could provide more event selection information. It is possible to see both the main, and the single-escape peak in the total scintillation light spectrum, but there is no significant background region in the scintillation-ionization plot which could be cut to reject backgrounds. Without a good reason to make cuts, we consider it inadvisable to apply additional cuts which might bias the calibration. This is why the selection cuts are kept simple, as they were in the previous analysis.

## Time Varying Pair Production Gains

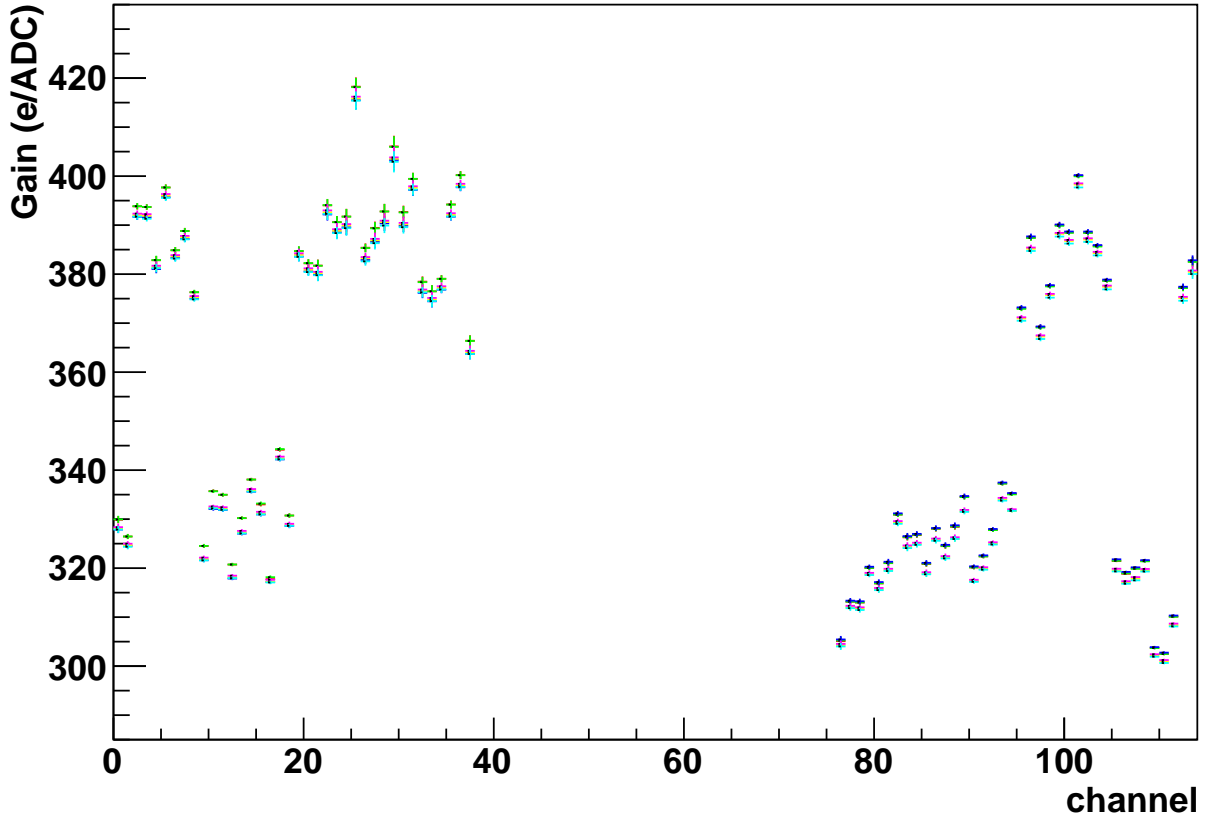


FIG. 13: Final time variation gains. These were derived from pair production data, but the time variation comes from internal charge injection data. The colors indicate the six time periods, though they are hard to see, as the time variation is so much smaller than the channel-to-channel variation. The colors are the same as in Figure 10, that is, red, green, blue, yellow, magenta, and cyan for periods 1-6, respectively.

### G. Conclusions

Using multiple methods, we have checked the U-wire gains for EXO-200 data in the period from Sept. 22, 2011, through April 15, 2012. We found that thorium source pair production gains provided for a better energy resolution on the Tl-208 photopeak than charge injection gains did. Statistics requirements force us to not divide the source data into time periods, so for time variation, we use the time variation of the internal charge injection run gains, having divided the data into six periods.

The effect of time variation is very small, and it does not change the energy resolution beyond uncertainties. However, future data could experience a relative change in gain between channels, and require this time variation feature. Thus, we implement the time variation in both U-wire gain and shaping times based on the internal charge injection data. In the future, we would like to automate the time varying gain computation.

Both charge injection and pair production data can produce good gains for these wires. At this point, improving the wire gains is very difficult. Even if a slightly better gain calculation scheme is developed, it is unlikely to have a significant effect on the energy resolution. Other contributions to the energy resolution are likely a better topic to focus on in the future.

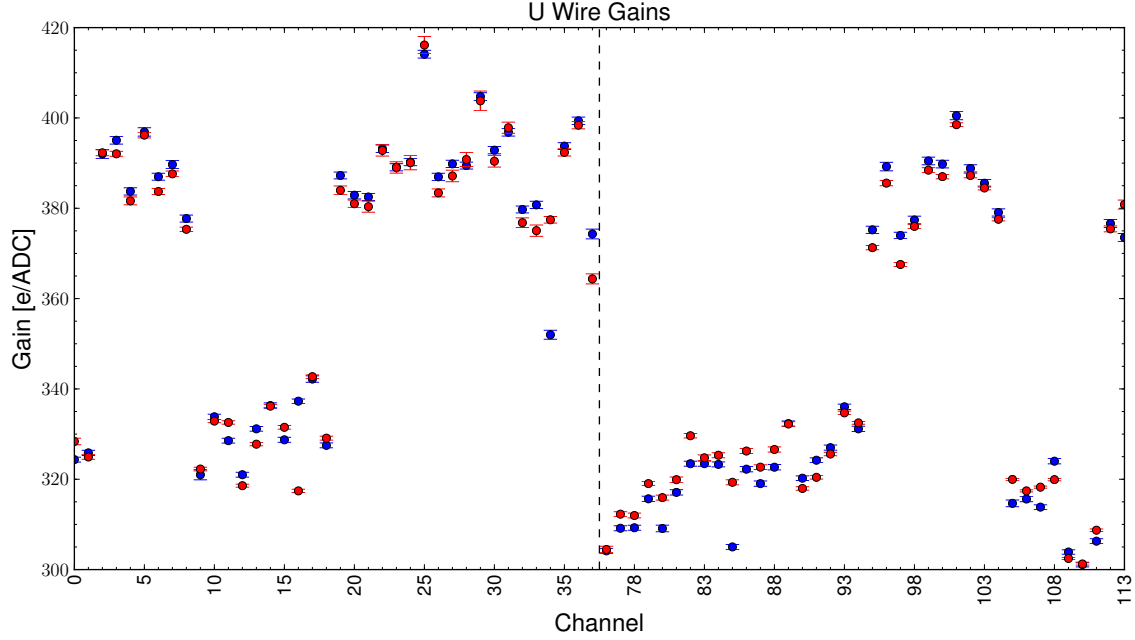


FIG. 14: Comparison of wire gains from corrected manual charge injection data (blue) and pair production gains (red). Error bars are from errors on fitted parameters, and do not consider systematic uncertainties.

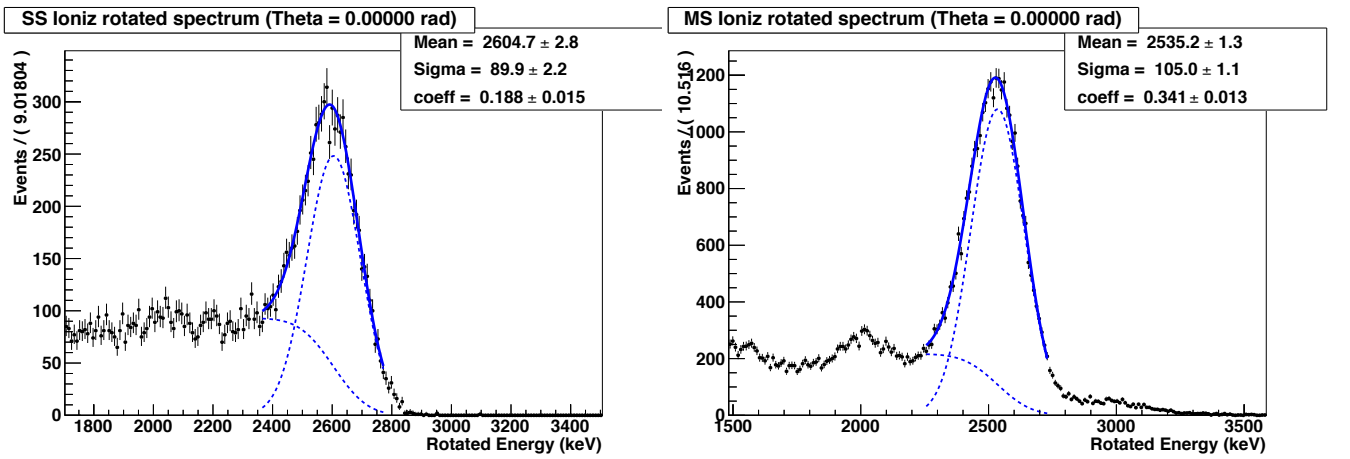


FIG. 15: Fitting the ionization energy of the Tl-208 photopeak. The error function + gaussian is used. These plots are for week 16. Left is SS, right is MS.

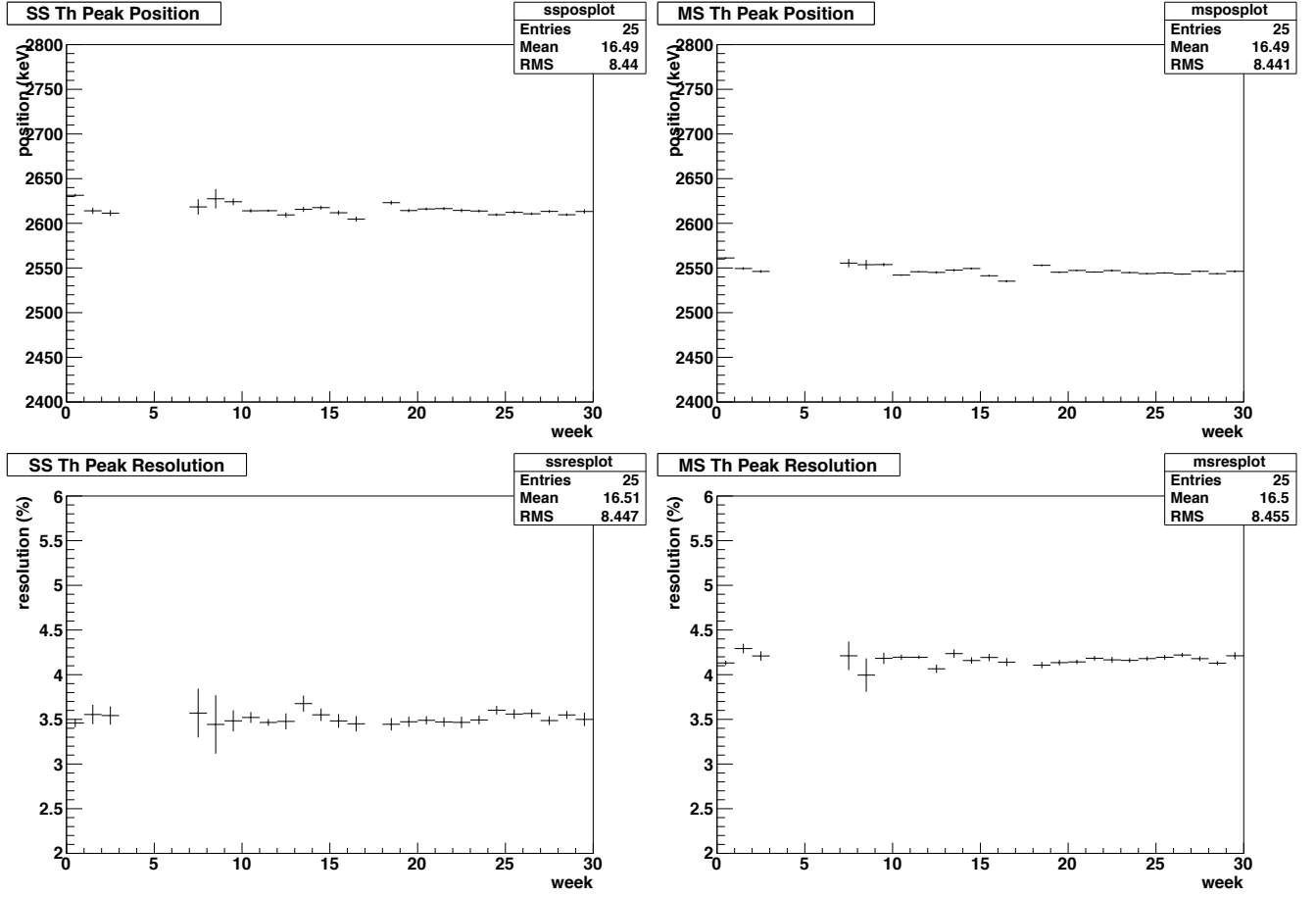


FIG. 16: Position and resolution of the Tl-208 photopeak using the new gains and shaping times, with new processing, purity fits, etc. These plots are for SS peak position (top left), MS peak position (top right), SS resolution (bottom left), and MS resolution (bottom right). There are some gaps in the data, for weeks where no Th source runs were selected.

### III. GRID SHIELDING EFFECT AND CORRECTIONS

#### A. Grid Shielding Effect

The V-wires provide a shielding effect on the U-wires, so that a charge drifting in the TPC region between the cathode and V-wires will only have a small effect on the U-wires. This shielding effect is however not fully efficient and the amplitude of the signal measured on the U-wires will depend on the initial position of the drifted charge.

One can understand this effect more clearly by considering that the induced charge on the U-wires from a charge,  $q$ , moving from  $\vec{y}_0$  to  $\vec{y}$  is given by  $q(\phi(\vec{y}) - \phi(\vec{y}_0))$ , where  $\phi$  is the weighting potential for the particular U-wire. If the V-wires fully shielded the U-wires from the drift region, then  $\phi(\vec{y})$  would be 0 through the entire drift region. A plot of the weighting potential calculated for the U-wires is shown in figure 17. It is clear from this figure that the weighting potential does not fully go to zero in the drift region. One can also see that the effect is much larger as the initial position of the charge gets closer to the V-wire plane. The ‘shielding grid inefficiency’ is then the dependence on the measure of the U-wire amplitude due to a charge originating at a particular location.

Please see the Monte Carlo document for the Run2A analysis for more information on the calculation of weighting potentials [? ].

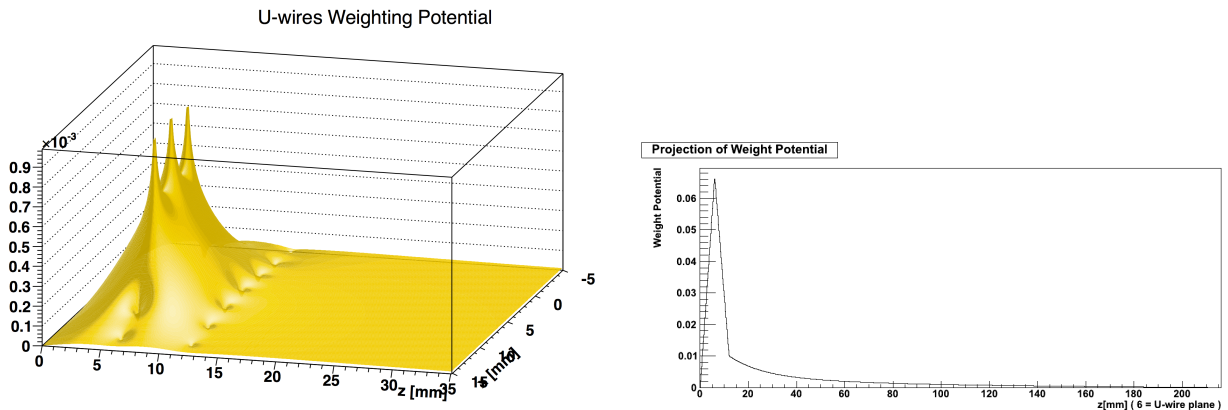


FIG. 17: Calculated weighting potential of the U-wires. One can see that the potential peaks at the location of the U-wires (6 mm in  $z$ ) and largely goes to 0 at the V-Wire plane (12 mm in  $z$ ). A projection of the 3-D plot is also shown.

#### B. Grid Correction

The shielding grid efficiency may be calculated in two ways:

1. Measure the dependence on the amplitude calculation versus initial reconstructed position of the charge. Since the initial magnitude of single charge depositions in the LXe are not known a priori in the data, this is performed by looking at the behavior of a prominent peak (e.g. 2615 keV) versus reconstructed position.
2. Use calculated weightings potentials and generate simulated U-wire signals with a simulated energy deposition. Because the initial position of charge depositions is known a priori, this can be used to directly determine the dependence of the U-wire amplitude calculation versus the initial charge position.

A combination of the two methods was performed. First, the second method was used to produce a correction function. This was then checked against data and Monte Carlo using the first method. It is important to note that, whereas the correction should in principal depend on the 3-D position of the initial charge deposition, the correction here only considers the dependence along the  $z$  direction. In addition, the correction is performed on clusters as opposed to on individual wires because the initial position of the event must be estimated. These leads to a dependency in the correction on the number of wires in a cluster.

### 1. Calculation of Grid Correction

The grid correction was calculated using the results from Monte Carlo [? ]. Monte Carlo of several different source types was taken, including  $2\nu\beta\beta$ , and  $^{228}\text{Th}$  and  $^{60}\text{Co}$  at S5. Single-site-like events were selected by requiring:

1. Energy-averaged z position of Monte Carlo pixelated charge deposits (PCDs) $\leq 3$  mm; AND
2. 1 U-wire hit with energy  $\geq 900$  keV; OR
3.  $>1$  U-wire hit with adjacent U-wires and both U-wires with energy  $\geq 200$  keV

The averaged z-position is then taken from the PCDs and the reconstructed U-wire energy is compared with the sum of the energies of the PCDs. The results from  $^{60}\text{Co}$ ,  $^{228}\text{Th}$ , and  $2\nu\beta\beta$  are shown in figures 18, 19, 20, respectively. Each set of data are fit with an equation of the form:

$$E_{meas} = E_0 \frac{1}{1 + p_0 e^{(|z| - 192.5)/p_1}} \quad (4)$$

where  $z$  is given in mm and 192.5 is z position of the V-wire plane.

Figure 21 shows the curves from the different sources overlaid. It is clear from the figure that the curves from each source predict similar correction functions. Table VI gives a summary of the values used from this study for equation 4.

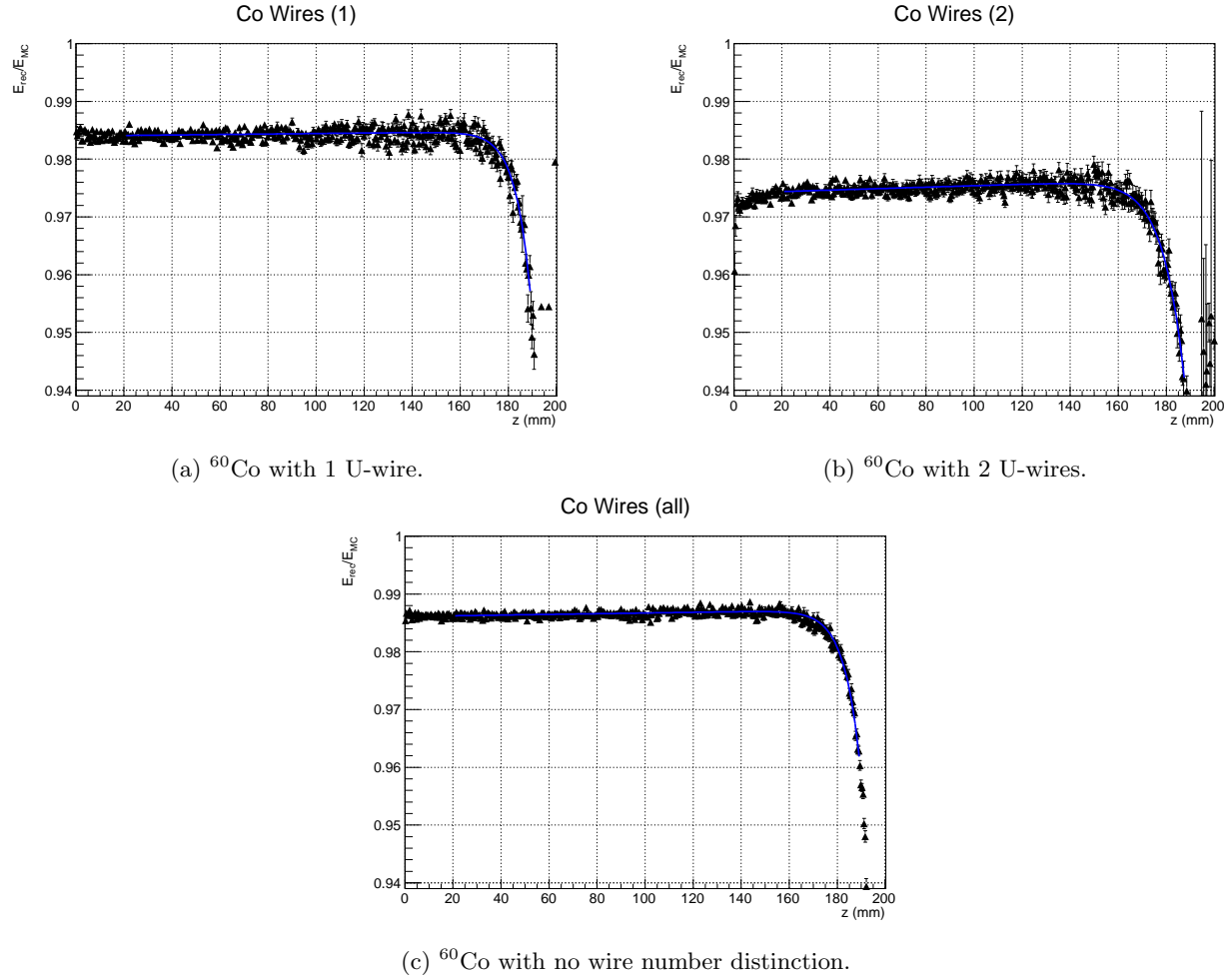
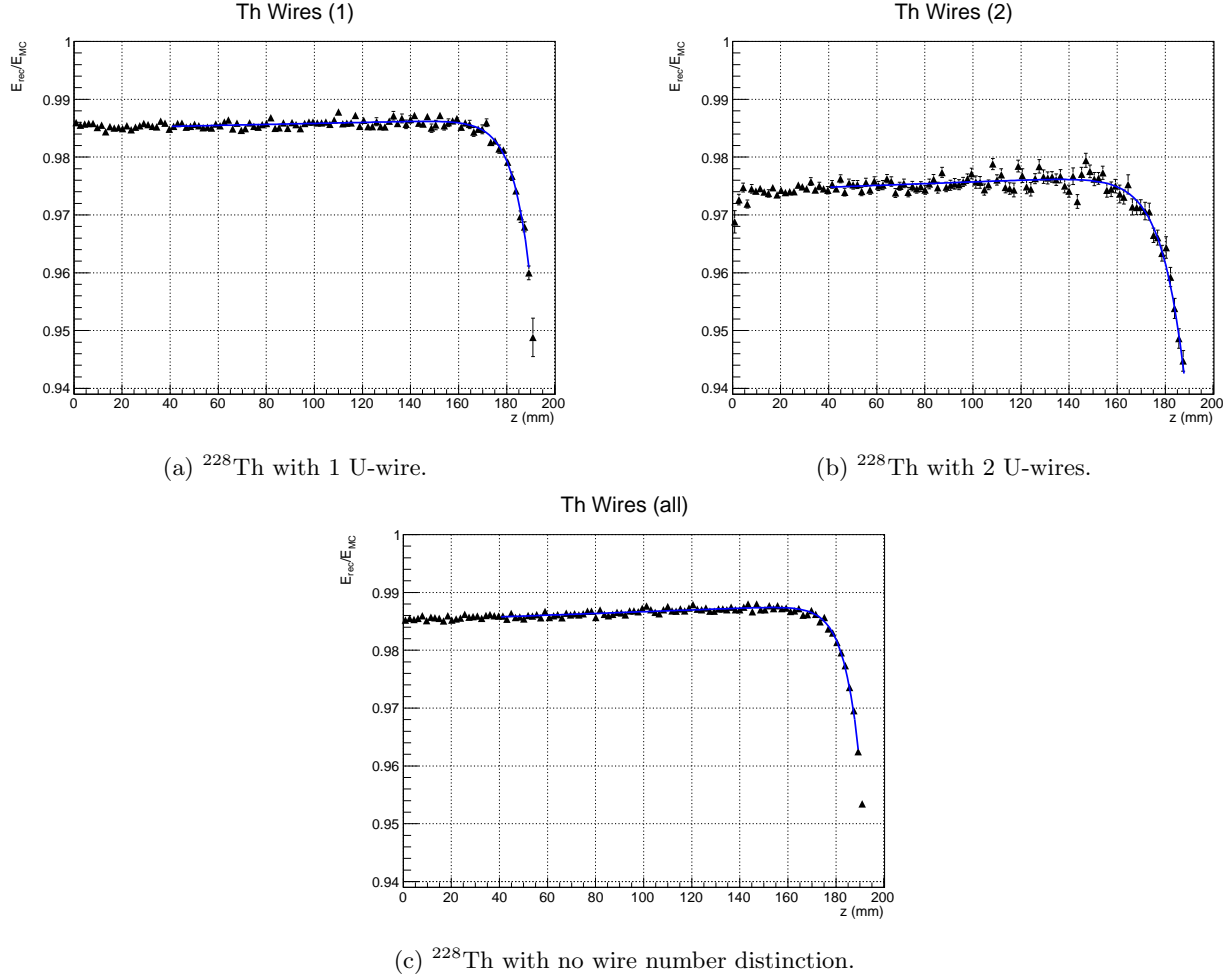


FIG. 18:  $^{60}\text{Co}$  results from Grid calculation.

FIG. 19:  $^{228}\text{Th}$  results from Grid calculation.

	$p_0$	$p_1$
1-Wire	0.043	7.02
2-Wire	0.064	8.49
All	0.043	6.06

TABLE VI: Parameters for correction functions derived from fits in figures 18, 19, 20 with equation 4.

## 2. Test of Grid Correction

After the correction was defined using the Monte Carlo study described in the previous section, this was then tested in both Monte Carlo and data by processing the data with the above correction and looking at the position of the fit 2615 keV peak in the  $^{228}\text{Th}$  spectrum versus z position. A successful correction should result in little or no z dependence. The results for Monte Carlo  $^{228}\text{Th}$  at S5 are shown in figure 22. A slight overcorrection is seen near the V-wire plane in the 2-wire case, in addition to a possible linear Z-dependence. The source of this distortion was not determined, but the magnitude of the distortion ( $\lesssim 0.4\%$  peak-to-peak) is small compared to the detector resolution.

A similar test was performed by looking at  $^{228}\text{Th}$  data at S5 and other positions as well: S2, S11, and S8. The runs used included the weak and strong runs. Specifically, 362 non-Bad or non-Suspect quality Th228 runs from 9/10/11 until 3/18/13 are used. (Note: this run quality cut will allow runs with the run quality not set into the data set.) These results are shown in figure 23. It is clear that a residual z dependence exists, and that some over correction occurs near the anode position ( $z \sim \pm 192$  mm). It is possible that this additional z dependence arises from an overcorrection in purity, and some correlation has been seen between the purity calculation and the applied gain correction. The residual z dependence results in shift of the the peak position of  $\sim 0.7\%$  over the entire z range, and

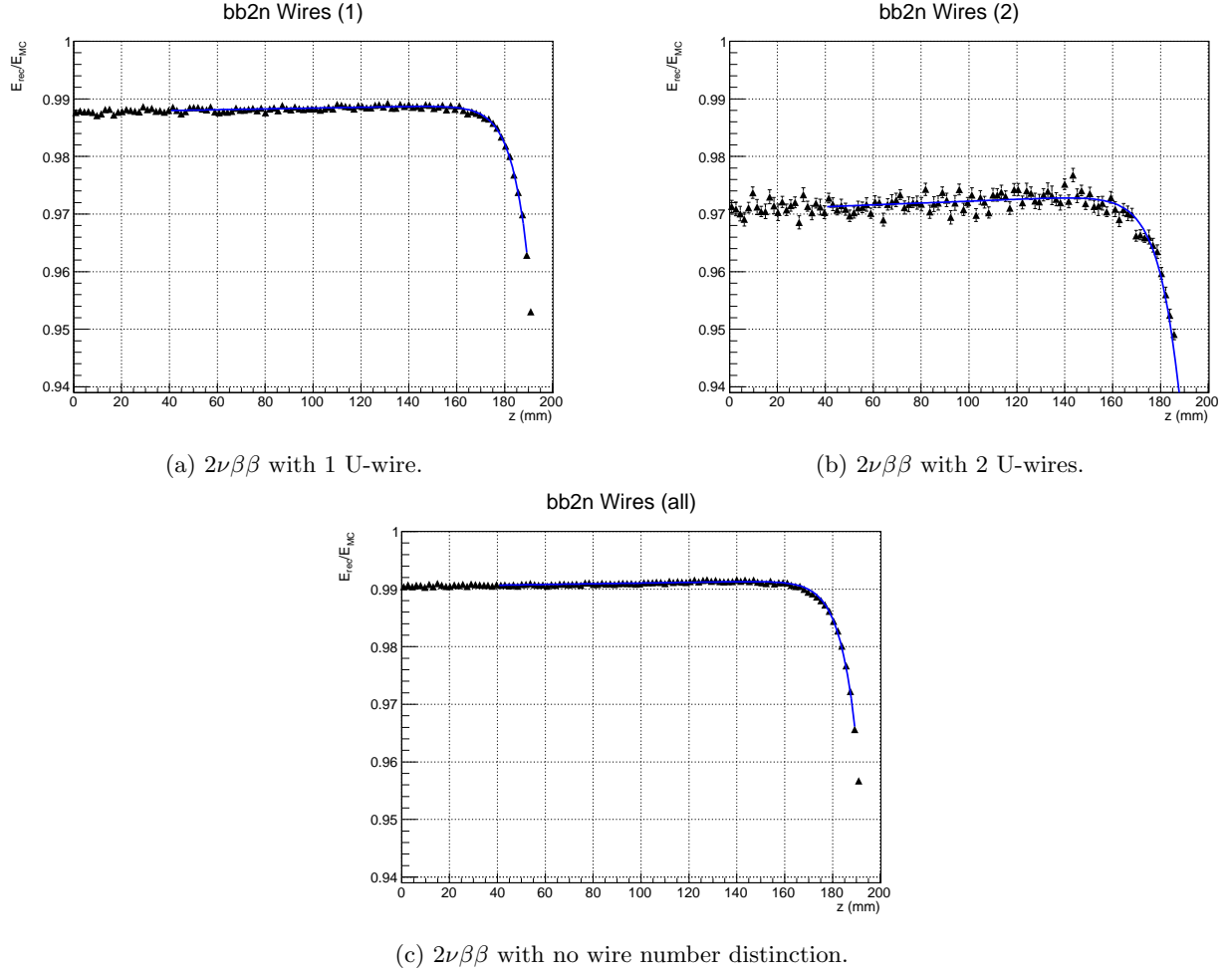


FIG. 20:  $2\nu\beta\beta$  results from Grid calculation.

somewhat less if one only considers the fiducial volume,  $15 \text{ mm} \leq |z| \leq 180 \text{ mm}$ . The remaining  $z$  dependence should not affect the overall resolution for the Run2A  $2\nu\beta\beta$  analysis, but will be investigated further.

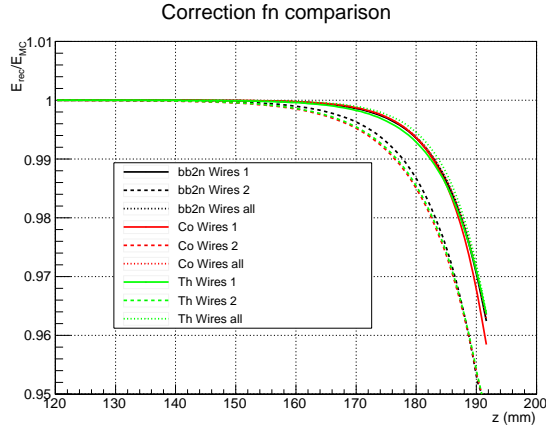


FIG. 21: Correction functions generated from grid correction analysis.

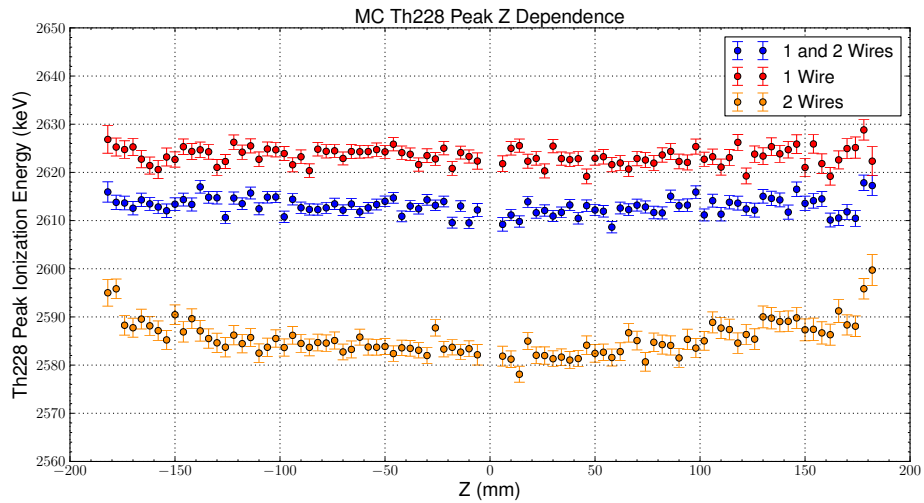


FIG. 22: Test applying the grid correction to  $^{228}\text{Th}$  Monte Carlo at S5.

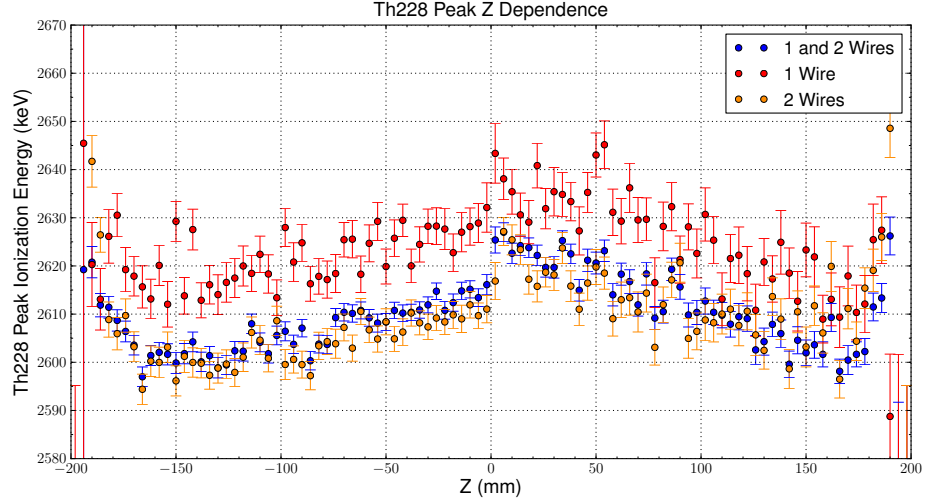


FIG. 23: Test applying the grid correction to available  $^{228}\text{Th}$  Data at S5, S2, S11, and S8. The plotted points are the fit position of the  $^{208}\text{Tl}$  2615 keV peak versus reconstruction Z position. 1-wire, 2-wire, and combined cases are shown.

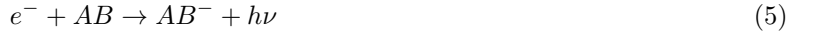
## IV. PURITY MEASUREMENT AND CORRECTIONS

### A. Electron Capture on Impurities

When an electromagnetic process deposits energy in a noble liquid detector, it ionizes the atoms, producing electrons and ions. Some of the electrons will recombine with the ions, which produces scintillation light. However, if the detector has an applied electric field, then the remaining electrons and ions will drift in opposite directions along the field lines. In a detector consisting of perfectly pure noble liquid, the electrons would all reach the anode and would be collected for an energy measurement. In a non-ideal detector, however, electronegative impurities can capture the drifting electrons and form ions. The ions are more massive and drift more slowly, and so they escape inclusion in the signal used for energy measurement.

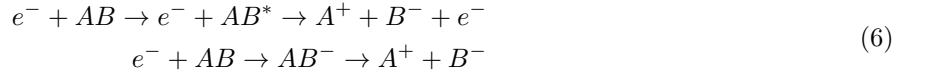
Electronegative impurities may capture electrons in three ways[? ]. Denoting the impurities, which may be atoms or molecules, as  $AB$ , these are:

1. Radiative attachment



which has a much smaller cross subsubsection than the other processes below.

2. Dissociative attachment



which requires the electron's energy to be much higher than typically found for an electron drifting in a liquid or dense gas.

3. Three-body attachment through the two-stage Bloch-Bradbury reaction



where  $X$  represents the atom or molecule that make up the majority of the liquid.

The three-body reaction shown in Eq. 7 releases some amount of energy, given by the *electron affinity* of  $AB$ . The electron affinity is positive if  $AB$  is electronegative. Noble elements have a negative electron affinity, so the reaction does not take place in a pure detector.

The rate of the reaction shown in Eq. 7 is given by:

$$\frac{dn_{AB}}{dt} = -k_3 n_{AB} n_X n_{e^-} \quad (8)$$

where  $k_3$  is constant for the 3-body reaction, and  $n_{AB}$ ,  $n_X$ , and  $n_{e^-}$  are the densities of the impurity, the atoms or molecules of the liquid, and the electrons, respectively.  $k_3$  depends on the species of the impurity, the species of the liquid, and the electric field strength.

According to Eq. 8, electrons will be captured, forming  $AB^-$  at a rate proportional to the density of electrons. Thus, the number of free electrons will decay exponentially over time according to:

$$N_{e^-}(t) = N_0 \exp(-t/\tau_e) \quad (9)$$

where  $N_0$  is the original number of electrons, and  $\tau_e$  is the *electron lifetime*.

In general, there can be several different species of electronegative impurity. In that case, they all contribute to the electron lifetime according to:

$$\tau_e^{-1} = \sum_i k_i n_i = \sum_i \tau_i^{-1} \quad (10)$$

where  $n_i$  is the density of an electronegative impurity and  $k_i$  is the cross subsubsection for electron capture by that impurity.

## B. Measuring Electron Lifetime

### 1. Method

Eq. 9 provides a simple recipe for measuring the electron lifetime: measure the exponential attenuation of a known quantity of ionization as a function of drift time. A source of monoenergetic gamma rays can provide such a signal. The ionization produced by the full absorption of a gamma ray follows a Gaussian distribution, with its width provided by the Fano factor and detector resolution. If some of the ionization is being attenuated, then the peak's mean will shift downward in energy from its true value.

A single calibration source at the cathode of the detector illuminates both TPCs, and the gamma rays interact throughout the entire drift region. After a sufficiently long calibration run, the TPC is divided into drift time bins. The size of the bins is a compromise: a larger bin in drift time will have more events, and thus the measurement of the full absorption peak energy will be better. A smaller bin will have fewer events, but will suffer less energy smearing because events will have similar drift times. In practice, 16 bins per TPC seems a good compromise.

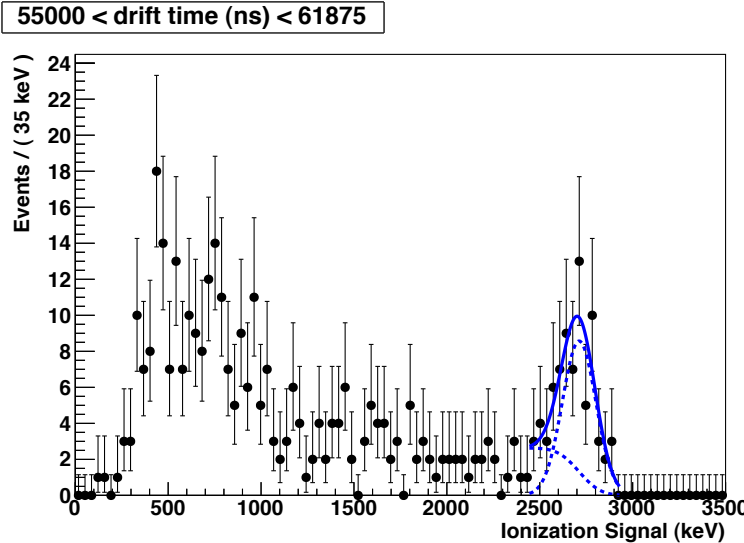


FIG. 24: A fit of the simple Gaussian + complementary error function model to one single drift time bin. In this example, the full absorption peak is the 2615 keV gamma line from  $^{228}\text{Th}$ .

In addition to the full-absorption peak, which is Gaussian, the energy spectrum from a gamma ray source will contain a Compton shoulder. Some gamma rays will interact without depositing their full energy, and then scatter out of the detector. A simple model for this shoulder is a step function convolved with a Gaussian smearing representing the effects of energy resolution, producing a complementary error function. For each drift time bin, this simple Gaussian + complementary error function model is fit to the energy spectrum of that bin using an unbinned maximum likelihood fit. This fit is performed twice, first over a broad energy range to find the full-absorption peak, then in the range  $(-3.0\sigma, +2.5\sigma)$  of the found peak to precisely determine the peak energy. Figure. 24 shows an example fit.

Plotting the full absorption peak energy from each drift time bin as a function of drift time reveals the exponential decay described in Eq. 9. Fitting an exponential to each TPC yields a measurement of the electron lifetime for each. Alternatively, a fit with a single electron lifetime to the entire detector uses information from both TPCs. In all cases, the amplitude of the exponential is allowed to float in the fit, since only the relative decay matters when measuring the electron lifetime. Presently, the separate TPC lifetimes are used when correcting for electron lifetime in EXO-200, while the single measurement is used when monitoring the detector and data quality. Figure. 25 shows an example. In EXO-200, the electron lifetime is typically  $> 1 \text{ ms}$  over a  $100 \mu\text{s}$  drift time, and so the attenuation begins to look approximately linear.

The electron lifetime measurement comes from minimizing the  $\chi^2$  statistic. Confidence intervals for the measurement come from doing a profile scan. Short electron lifetimes are easily distinguished, while longer electron lifetimes are not, and so the intervals will be asymmetric about the minimum. For a profile scan the electron lifetime is set to some fixed value away from the best fit value, and the amplitude is allowed to vary to minimize  $\chi^2$ . All electron lifetime values for which this remiminized  $\chi^2$  is less than 1 above the minimum value define the  $1\sigma$  (68%) confidence band. Figure. 26 shows an example.

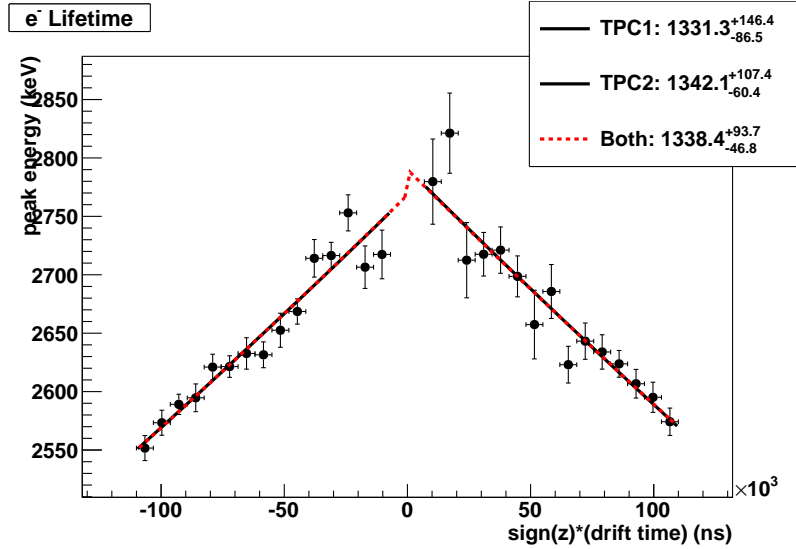


FIG. 25: Measuring the electron lifetime by fitting a decaying exponential to the full-absorption peak energies binned by drift time. TPC 2 is assigned a negative drift time for convenience in visualization. Both fits to the individual TPCs and to both TPCs together are shown. In this case, there is no large difference between the combined fit and the individual fits.

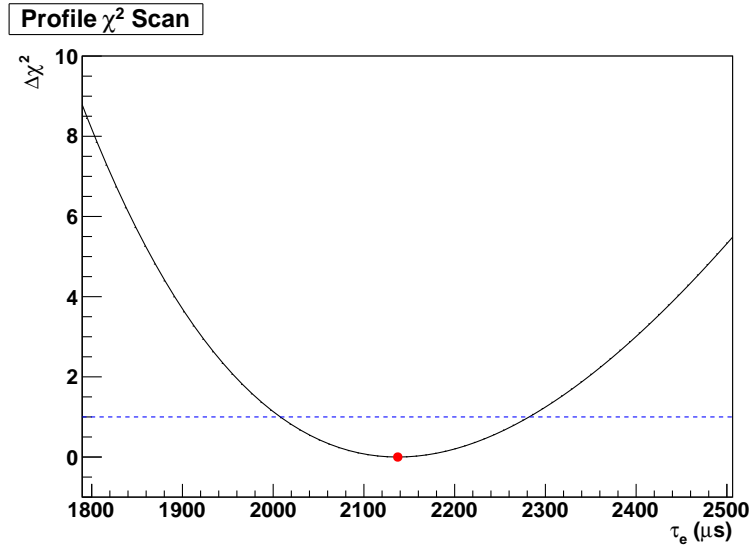


FIG. 26: Confidence intervals around the best fit electron lifetime come from a profile scan, shown here. As this figure shows, this is superior to simply estimating the  $1\sigma$  errors from the second derivative at the best fit value, since the profile is asymmetric around the best fit (indicated by the red dot). The blue line indicates  $\Delta\chi^2 = 1$ , corresponding to a 68% confidence interval.

## 2. Comparison to Simulation

Figure. 27 shows a comparison between a known simulated electron lifetime and the measurement of that lifetime using the method described above. The error is small for electron lifetimes below 1 ms. For large electron lifetimes, however, the method consistently underestimates the electron lifetime, with the effect getting worse as the electron lifetime improves.

This effect seems to be due to a some  $z$ -dependence introduced in processing the data. In simulations of a  $^{228}\text{Th}$  source at the cathode with infinite electron lifetime, the method reports electron lifetimes of  $3.0(9) \times 10^4 \mu\text{s}$  measured in both TPCs simultaneously, and  $4.3(9) \times 10^4 \mu\text{s}$  measured in a single TPC, for runs with 2.5k events in

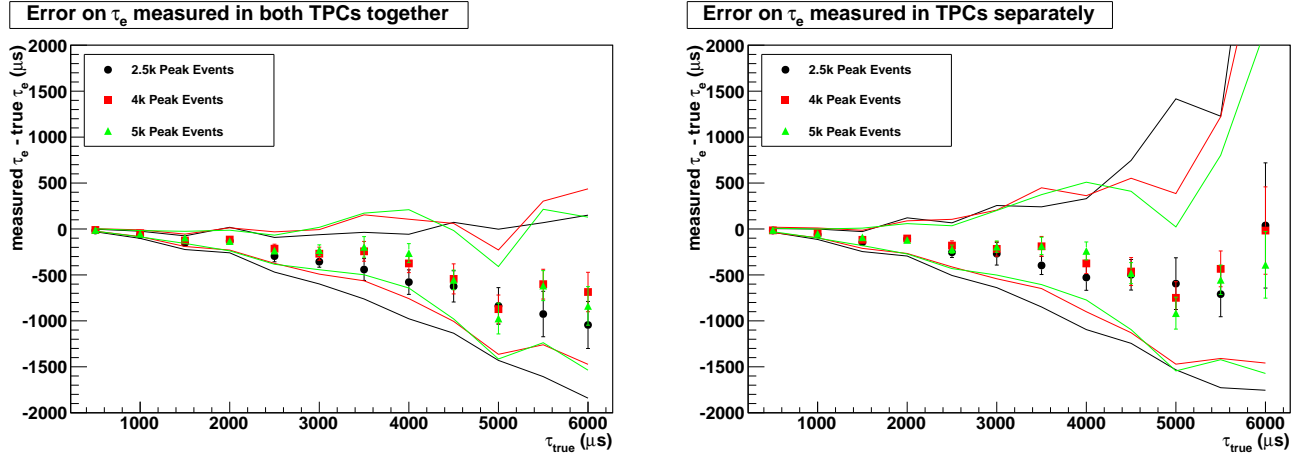


FIG. 27: The absolute error on the electron lifetime measurement for the electron lifetime measured in both TPCs simultaneously (left) and individually (right). The points show the mean error of 20 simulations. The lines show the size of the 68% confidence bands returned by the measurement for those simulations. The measurement method systematically underestimates the purity, and the error grows as the electron lifetime gets large. Typical calibration runs include 2.5k events in the full absorption peak (black), but using more events would improve the error.

the full absorption peak. It reports electron lifetimes of  $5.0(7) \times 10^4 \mu\text{s}$  measured in both TPCs simultaneously and  $4.9(8) \times 10^4 \mu\text{s}$  measured in a single TPC, for runs with 5k events in the full absorption peak.

The error due to this effect is small, however. A measured electron lifetime of  $3000 \mu\text{s}$  corresponds to a true electron lifetime of roughly  $(1/3000 - 1/40000)^{-1} = 3250 \mu\text{s}$ . This will only move the corrected ionization signal 0.3% higher than its true value, if the ionization drifts over the full  $120 \mu\text{s}$  drift time. The effect on the energy resolution in the ionization channel will be half of this, and even smaller in the rotated spectrum. It is not understood what in the processing chain causes the effect, or if it is also present in real data. Therefore, this effect is accepted as a slight worsening in energy resolution, rather than corrected for.

### 3. Practical Considerations

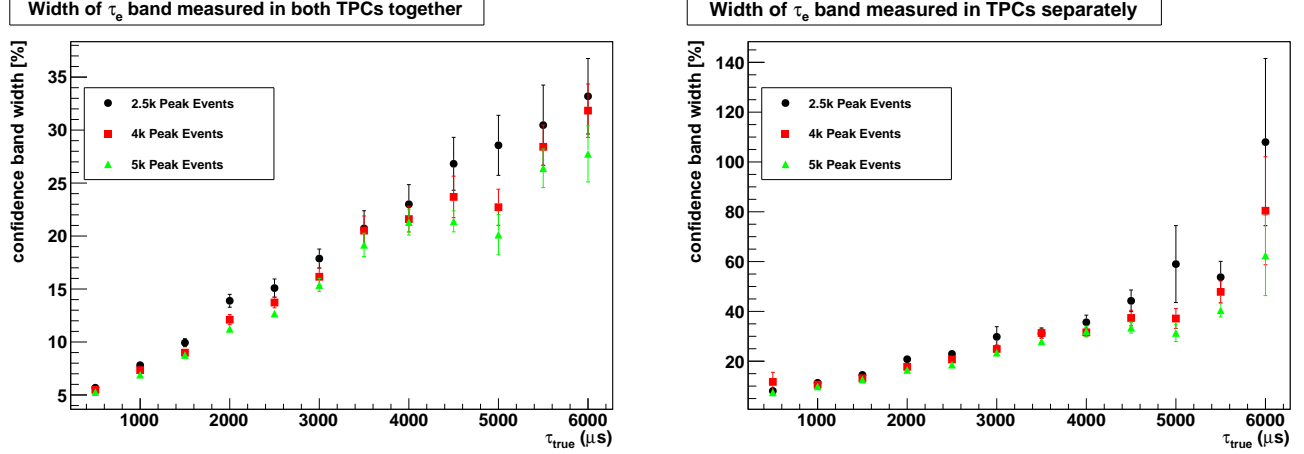


FIG. 28: The width of the 68% confidence band for the electron lifetime measured in both TPCs simultaneously (left) and individually (right). Typical calibration runs include 2.5k events in the full absorption peak (black dots), but using more events would improve the error. Using longer calibrations would improve the uncertainty. However, for long electron lifetimes, it becomes difficult to detect the attenuation and measure it, giving a large uncertainty.

As the electron lifetime grows large, it becomes increasingly difficult to measure. For a  $4000 \mu\text{s}$  electron lifetime,

ionization drifting the full distance will only be attenuated about 3%. This is comparable to the 3.4% energy resolution in the ionization channel at the 2615 keV full absorption peak from  $^{228}\text{Th}$ . This effect is shown in Figure 28. The width of the confidence band for the measurement grows to near 20% of the measured value for large electron lifetimes. Taking more calibration data only partially mitigates this effect, also shown in Figure 28. For low electron lifetimes, a simulated calibration run with twice as many events in the full absorption peak (and requiring twice as much time to run) shrinks the confidence band by roughly  $\sqrt{2}$ . For large electron lifetimes, more events don't shrink the band, suggesting systematic errors such as the relatively short drift time dominate.

### C. Effects of Electron Lifetime on the Energy Resolution

The error on  $E_{rotated}$  due to an uncertainty  $\Delta\tau$  in the electron lifetime is:

$$\frac{\Delta E_{rotated}}{E_{rotated}} = \cos(\theta) \frac{t_d}{\tau^2} \Delta\tau \quad (11)$$

and the error on  $E_{rotated}$  due to an uncertainty  $\Delta t_d$  in the drift time is:

$$\frac{\Delta E_{rotated}}{E_{rotated}} = \cos(\theta) \frac{\Delta t_d}{\tau} \quad (12)$$

#### 1. Position Uncertainty

For true (point-like) single-site events, we can measure their drift time to within about 0.2  $\mu\text{s}$  thanks to the information provided by including multiple points in the fit that extracts information from waveforms. This uncertainty will cause some smearing of the resolution, since the correction relies on a measurement of the drift time. The effect is easy to calculate using Eq. 12. Table. VII provides some concrete numbers.

TABLE VII: The effect of a 0.2  $\mu\text{s}$  drift time uncertainty on the rotated energy resolution, assuming a 100  $\mu\text{s}$  drift time.

$\tau$ ( $\mu\text{s}$ )	$\Delta E/E$ (%)
100	0.20
200	0.10
400	0.05
800	0.02
1000	0.02
1500	0.01
2000	0.01
2500	<0.01

Most events, however, are not point like, and the ionization arrives over a finite period of time. This leads to an uncertainty on the true drift time of  $\sim 3 \mu\text{s}$ , which will result in more smearing of the energy resolution due to the electron lifetime correction. Table. VIII shows the spread for this scenario.

TABLE VIII: The effect of a 3  $\mu\text{s}$  drift time uncertainty on the rotated energy resolution, assuming a 100  $\mu\text{s}$  drift time.

$\tau$ ( $\mu\text{s}$ )	$\Delta E/E$ (%)
100	2.95
200	1.48
400	0.74
800	0.37
1000	0.30
1500	0.20
2000	0.15
2500	0.12
3000	0.10
3500	0.08

## 2. Electron Lifetime Uncertainty

The effect of electron lifetime uncertainty on the energy resolution is given by Eq. 11. With a fixed drift time, it becomes increasingly difficult to measure long electron lifetimes because the attenuation is so slight. The drift distance in EXO-200 is fixed. Varying the electric field to increase the drift time carries some risk to the experiment and so is not done routinely. Furthermore, the attachment rates for electronegative species vary with electric field (see section. IV D 4). Lacking knowledge of the precise nature of the impurities in EXO-200, it is not clear this would provide a good estimate for the electron lifetime at normal electric fields. Parameterizing the uncertainty as a function of electron lifetime provides a way to estimate its effect on energy resolution.

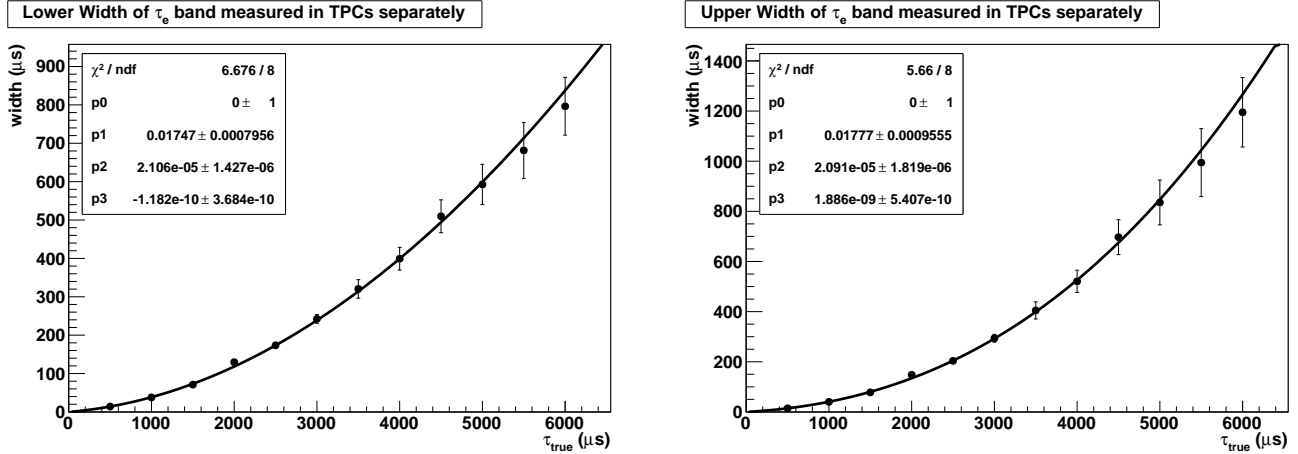


FIG. 29: The width of the uncertainty bars on single electron lifetime measurements as a function of the electron lifetime. Since the uncertainties are asymmetric, the negative uncertainty (left) and the positive uncertainty (right) are fit separately. The fit function is a cubic polynomial.

As shown in Figure. 29, a polynomial function nicely fits the observed uncertainties. The effect on energy resolution is tabulated in Table. IX. In practice, however, a number of measurements go into the actual correction function applied to the data, and so the effect will be smaller.

TABLE IX: The effect of the electron lifetime uncertainty on energy resolution. This is based on the parameterization shown in Figure. 29. Note that the reported resolution assumes only one measurement is used for the correction. In practice, more measurements are used, and so the effect will be smaller.

$\tau$ (μs)	$\Delta E/E$ (%)
100	3.88
200	2.15
500	1.11
800	0.86
1000	0.78
1500	0.67
2000	0.62
2500	0.59
3000	0.58
3500	0.57

## 3. Rate of Change

The electron lifetime can vary with time. The most dramatic instances are following outages, when recirculation is resumed after a period of letting xenon stagnate. Impurities leaching out of the materials in the vessel, or from liquid xenon coming into contact with different subsubsections of plumbing can cause the purity to degrade. When the pump is turned back on, the purity recovers over several days. Likewise, as the pump operates, it can lose pumping ability, which slows the recirculation rate.

Suppose we have two measurements,  $\tau_1 \pm \sigma_{\tau_1}$  and  $\tau_2 \pm \sigma_{\tau_2}$ . The best estimate of the rate of change is simply

$$\frac{d\tau}{dt} = \frac{\tau_2 - \tau_1}{\Delta t}$$

However, propagating the uncertainties, the error on the estimate is

$$\Delta \frac{d\tau}{dt} = \frac{d\tau}{dt} \sqrt{\left(\frac{\sigma_{\tau_1}}{\tau_1}\right)^2 + \left(\frac{\sigma_{\tau_2}}{\tau_2}\right)^2}$$

If the true rate of change is  $+1\sigma$  away from the estimate, events close to the first measurement will be undercorrected, and events close to the second measurement will be overcorrected. This results in an overall smearing to the energy resolution, tabulated in Table. X. This effect will grow if the time between measurements is increased, since more data will be taken with an estimate far from the true value.

TABLE X: The effect of the rate of change of electron lifetime on energy resolution. This shows the additional effect due to uncertainty in the rate of change, with measurements taken 1 day apart. Longer intervals between measurements will result in more smearing. Note that the reported resolution assumes only two measurements are used for the correction. In practice, more measurements are used, and so the effect will be smaller.

$\tau$ (μs)	$d\tau/dt$ (μs d <sup>-1</sup> )	$\Delta E/E$ (%)
1000	10	0.05
	50	0.25
	100	0.47
	500	1.70
	1000	2.44
2000	10	0.01
	50	0.07
	100	0.13
	500	0.54
	1000	0.89
3000	10	0.01
	50	0.03
	100	0.06
	500	0.27
	1000	0.47

#### 4. Overall

The effects of electron lifetime on resolution are taken in account when selecting which runs will be used for the analysis. The guidelines are such that the resolution smearing due to the electron lifetime correction is no more than 0.5%. Runs can be used if:

1. Electron lifetime is above 1000 μs (due to the effects of position uncertainty and electron lifetime uncertainty)
2. Four or more measurements all show similar electron lifetime (to reduce the effect of the electron lifetime uncertainty)
3. The electron lifetime must not be increasing by more than half of its current value per day, nor decreasing by more than a quarter of its current value per day (to reduce the effect of time variation)

#### D. Measurements of Electron Lifetime in EXO-200

Calibration runs taken every 1–2 days serve to measure the electron lifetime in EXO-200. In a typical calibration run, a <sup>228</sup>Th source at the cathode creates  $2.5 \times 10^5$  events in the TPC. Of these, approximately 2500 are single site events within  $2\sigma$  of the full-absorption peak.

### 1. Time Variation and Correction Function

The measured electron lifetime varies in time. Usually, this variation is small and slow. To account for this, a piecewise polynomial is fit to the measured electron lifetimes. This piecewise polynomial can be discontinuous across sudden changes in electron lifetime (due to effects such as recirculation pump stoppages). The polynomial degree can change when the behavior of the electron lifetime changes, such as when rapidly-increasing lifetime after resuming recirculation becomes a steady-state, slowly-varying value. Figure. 30 shows the time variation and the polynomial fit for the separate TPCs. Separate electron lifetimes are used for the different TPCs because there could be some purity gradient in the chamber, and splitting the chamber in half provides a modest approximation. Furthermore, the measured values in the different TPCs are observed to sometimes vary outside of each others' confidence bands.

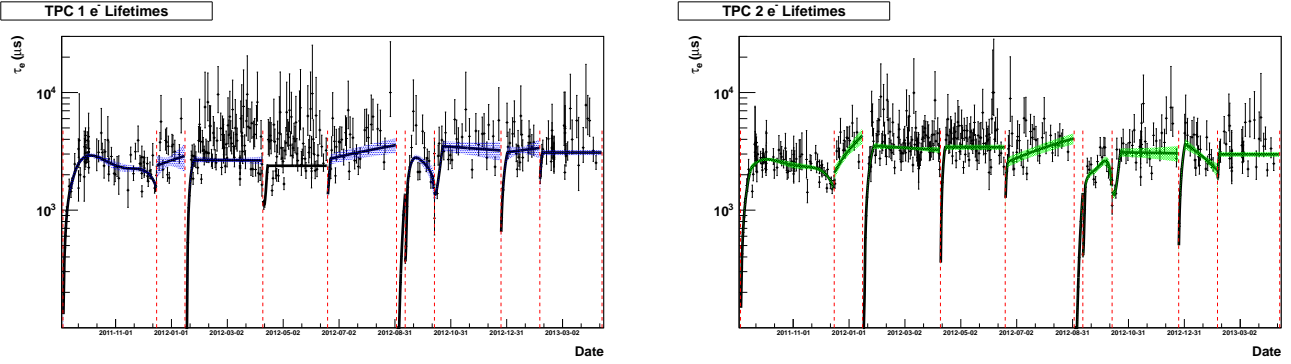


FIG. 30: The fit of a piecewise polynomial to electron lifetime in TPC 1(left) and TPC 2 (right). The colored bands show the 68% confidence interval on the fit. The vertical dashed lines indicate discontinuities in the electron lifetime due to pump stoppages or xenon feeds.

For a good event in EXO-200, the reconstruction algorithms find both a drift time and an (attenuated) ionization signal. The polynomial fit described above provides an estimate of the electron lifetime at the event time. Eq. 9 provides a recipe for correcting the attenuated ionization signal to get a corrected signal, using the drift time and measured electron lifetime.

### 2. Comparison with Recirculation Rate

The rate at which xenon is recirculated through the purifiers effects electron lifetime. Figure. 31 shows a clear trend of increasing electron lifetime with increasing recirculation rate. The highest electron lifetimes are achieved with a recirculation rate above 13 slpm, which corresponds to completely recirculating the volume of the chamber in 1.8 days.

Figure. 32 shows the time history of the electron lifetime, plotted along with the recirculation rate. Since the electron lifetime in the chamber decreases when the pump is recirculating at a reduced rate, there is most likely a constant source of impurities in the TPC. That the electron lifetime worsens significantly after prolonged recirculation stoppages supports this. However, when the recirculation stops, the pressures throughout the system change. This causes liquid levels to change and may also cause the slow control system to feed in more gas. Newly exposed or submerged plumbing, and new gas (even though it is fed through the purifiers, some may be able to feed backward through the pump) could also cause this decrease in electron lifetime, and it is difficult to disentangle the effects. In any case, once recirculation is resumed, the electron lifetime recovers over the course of a few days.

### 3. Comparison with Gas Purity Monitor Readings

The gas purity monitors[?] provide real-time monitoring of the recirculating xenon. GPM 3 samples the gas returning from the TPC. GPM 2 samples the gas coming out of the purifiers. GPM 1 samples the gas at the output of the recirculation pump. Because these sample room temperature gas instead of cryogenic liquid, some impurities may be in different concentrations than in the TPC due to different solubilities. Likewise, the gas purity monitors have a small electric field and short drift distance, and so they will not be able to measure long electron lifetimes. Despite this, GPM 3 may be able to provide some information about the purity of the xenon in the TPC when that purity is poor.

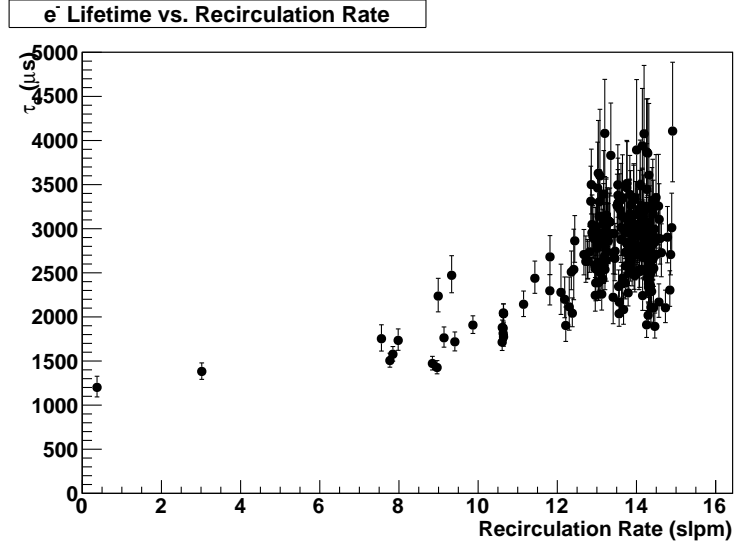


FIG. 31: The electron lifetime plotted as a function of recirculation rate. Time periods when recirculation was fast, but electron lifetimes were low due to a pump stoppage or feed event have been removed. A clear trend is visible in which electron lifetime increases with recirculation rate.

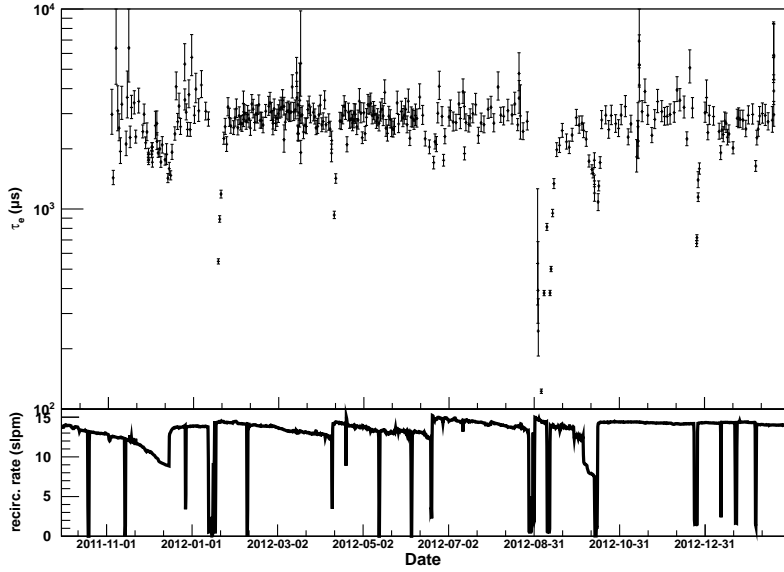


FIG. 32: A time history of the electron lifetime, with the recirculation rate plotted below. The electron lifetime drops when the pump slows or completely stops, and recovers when recirculation resumes at a fast rate.

Figure 33 shows a plot of the gas purity monitor reading for gas returning from the TPC during periods when the electron lifetime was poor due to a pump stoppage or feed event. A loose correlation is visible, with a correlation coefficient of 0.55 over all points. More interesting is that the correlation is stronger during individual recovery incidents, denoted by different markers and colors. So, while the gas purity monitors do not measure the electron lifetime in the TPC on an absolute scale, they provide a good indication of large changes in the electron lifetime.

#### 4. Electron Lifetime in Low Electric Field

The rate constant for electron attachment to impurities varies with the electric field strength, and the species of impurity determines the nature of this variation. As shown in Figure 34 [?], O<sub>2</sub> impurities show decreasing

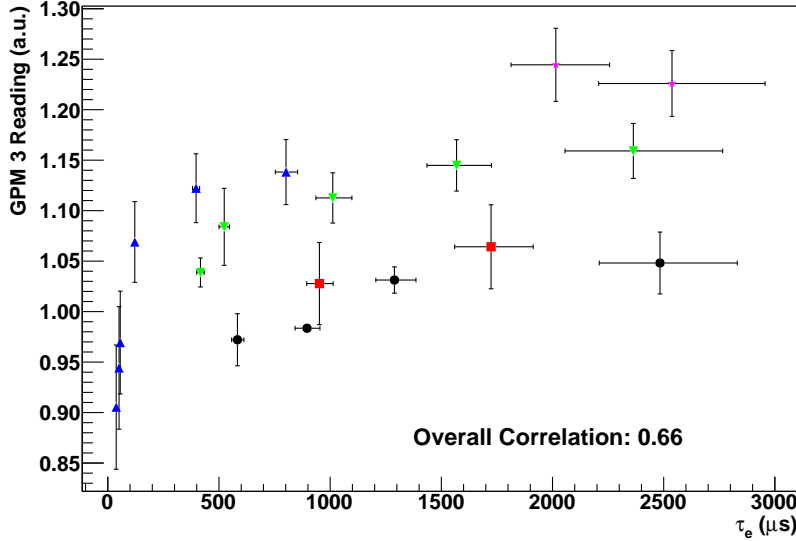
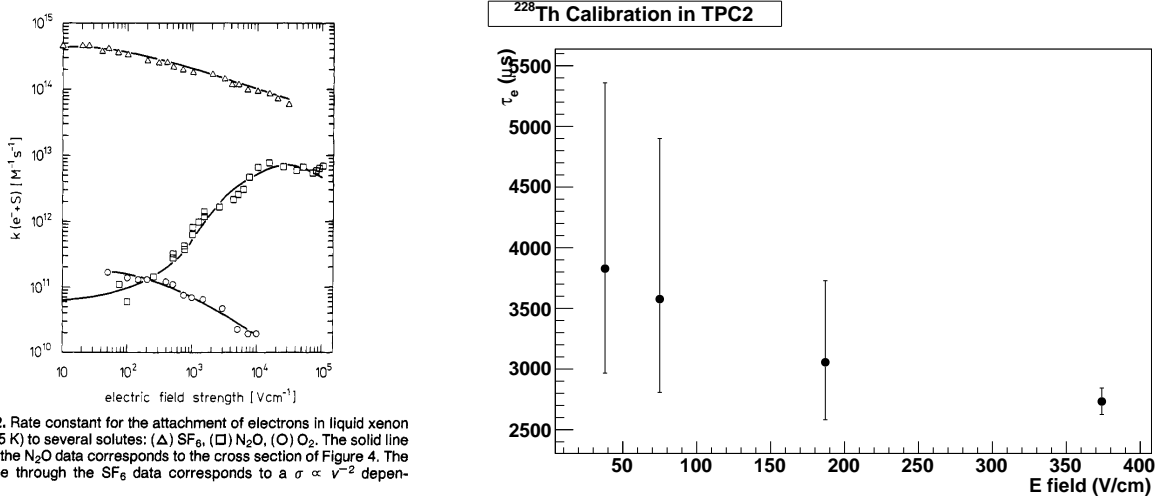


FIG. 33: The reading from the gas purity monitor sampling the gas returning from the TPC (GPM 1), during periods when the electron lifetime was recovering from a pump stoppage or feed event. Different recovery incidents are denoted with different colors and markers. There is an overall correlation coefficient of 0.66 between the GPM reading and the electron lifetime. However, the correlations in individual incidents are stronger.

attachment with increasing field strength, while N<sub>2</sub>O show the opposite.



**Figure 2.** Rate constant for the attachment of electrons in liquid xenon ( $T = 165$  K) to several solutes: ( $\Delta$ ) SF<sub>6</sub>, ( $\square$ ) N<sub>2</sub>O, ( $\circ$ ) O<sub>2</sub>. The solid line through the N<sub>2</sub>O data corresponds to the cross section of Figure 4. The solid line through the SF<sub>6</sub> data corresponds to a  $\sigma \propto v^{-2}$  dependence.

FIG. 34: On the left is a figure by Bakale et al., showing the electron attachment constant as a function of electric field strength. On the right is the measured electron lifetime, which is inversely proportional to the attachment constant, for a number of electric field strengths. For these runs, the calibration source was located slightly on the TPC 2 side of the cathode, giving more events and allowing a better measurement in this TPC. The nominal field for normal operation is 374 V cm<sup>-1</sup>. The results are not incompatible with a constant electron lifetime ( $\chi^2/n.d.f. = 3.15/3$ ). However, there does seem to be a trend of decreasing electron lifetime with increasing electric field, and the magnitude of this decrease is not unreasonable, resembling that expected for N<sub>2</sub>O. (Left figure reprinted with permission from [? ]. Copyright 1976 American Chemical Society.)

Calibration runs of the standard length were taken with the cathode at -4.4 kV, -2.2 kV, -1.45 kV and -1.1 kV, corresponding to electric field strengths of 187 V cm<sup>-1</sup>, 75 V cm<sup>-1</sup>, 38 V cm<sup>-1</sup> and 20 V cm<sup>-1</sup>. Normal operation is at -8 kV, corresponding to 374 V cm<sup>-1</sup>. Unfortunately, there were not enough events in the full-absorption peak to measure the electron lifetime at the lowest field strength. The results are shown in Figure 34. The electron lifetime seems to decrease with increasing electric field, unlike as expected for oxygen. There is not enough information to

identify the exact species of impurity present. For species with similar molecular weight and electron attachment as N<sub>2</sub>O and O<sub>2</sub>, the required concentration of impurities for a 3 ms electron lifetime is on the order of 10<sup>-11</sup> g/g.

### 5. Electron Lifetime Results

In the fit of the electron lifetime versus time, some of the lifetime values from individual runs are excluded. The runs are excluded when the statistics in the full absorption peak do not allow for a well-determined lifetime fit for all z positions in the detector. As a result, all runs that used the <sup>137</sup>Cs calibration source are excluded from the time varying electron lifetime fit. Runs are also excluded when there is significant disagreement between lifetime values of runs that are close together in time but no physical change in the system to justify this change in lifetime. Because runs with shorter electron lifetimes have smaller bars, the runs with poor lifetime values drive the polynomial fit to the data. For this reason, these data are excluded from the fit when they are surrounded by several runs with longer electron lifetimes. Generally runs that are several sigma (or  $\approx 200 \mu\text{s}$ ) away from the surrounding points are excluded from the fit.

The choice of which runs to exclude in the final fit can have a significant effect on the overall lifetime fit. The piecewise polynomial fit to electron lifetime was performed using two independent sets of excluded runs. The time intervals of the piecewise polynomial fit are the same for the two fits in order to minimize the differences between the fits that occur during rapid changes in the electron lifetime. One set of fits is shown in Figure. 35 and the other set of fits is shown in Figure. 36. The fits qualitatively agree with one another as shown in the comparison of the fits in Figure. 37. However, the exclusion of a handful of runs can cause a sustained difference of 500  $\mu\text{s}$  and a peak difference of up to 1500  $\mu\text{s}$  as shown in Figure. 38. This effect is greatest during periods of rapidly changing lifetime, such as after a pump stoppage.

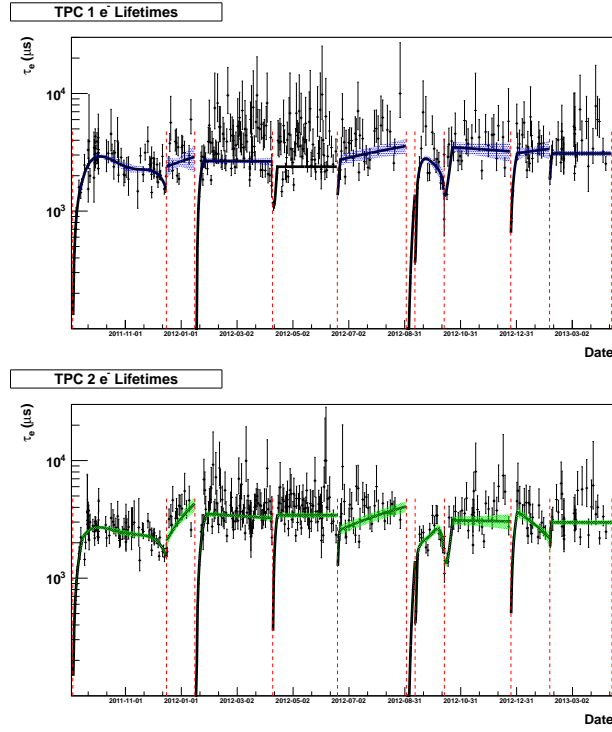


FIG. 35: The fit of a piecewise polynomial to electron lifetime in TPC 1(left) and TPC 2 (right). The colored bands show the 68% confidence interval on the fit. The vertical dashed lines indicate discontinuities in the electron lifetime due to pump stoppages or xenon feeds.

An accurate fit to the electron lifetime measurements improves the energy resolution. The electron lifetime has been fit from September 22, 2011 through the present covering data taken during Run 2a, from September 22, 2011 through April 15, 2012, and Run 2b, from April 16, 2012 through the present. The low-background data set only includes periods of long and stable lifetimes. The fit parameters from Figure. 36 are currently stored in the database and are used for the correction of the charge signal in the low-background data.

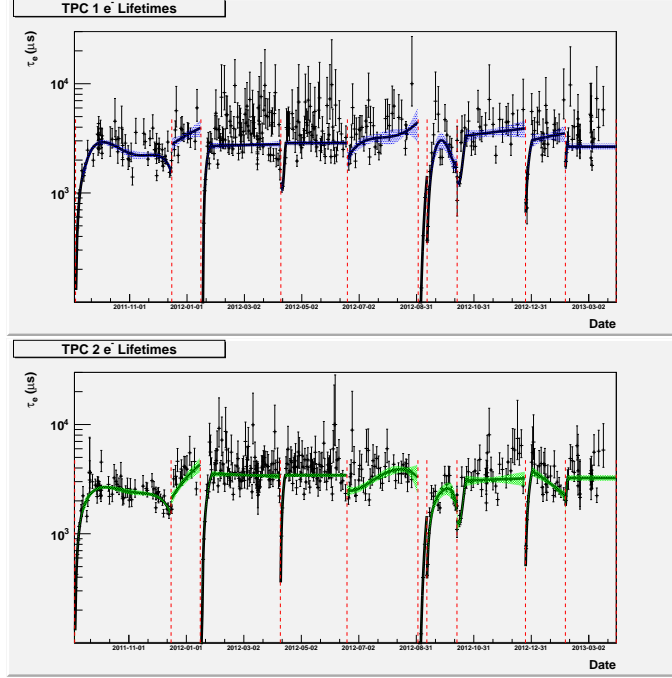


FIG. 36: The fit of a piecewise polynomial to electron lifetime in TPC 1(left) and TPC 2 (right). The colored bands show the 68% confidence interval on the fit. The vertical dashed lines indicate discontinuities in the electron lifetime due to pump stoppages or xenon feeds.

The most up-to-date fits to the electron lifetime are shown in Figure 39 currently fit through April 8, 2013. The agreement of the electron lifetime fits for the two individual TPCs is shown in the overlap of the 68% confidence bands. For Run 2a, it is obvious that fits to the two TPCs as separate detectors is well justified. For Run 2b, the fits are very similar within the uncertainty of the fits and a fit to the whole TPC may provide as good a lifetime value as the two separate fits, but there are two time periods in Run 2b where this is not the case; therefore, a fit to each TPC is still being used for the electron lifetime correction to the low-background data.

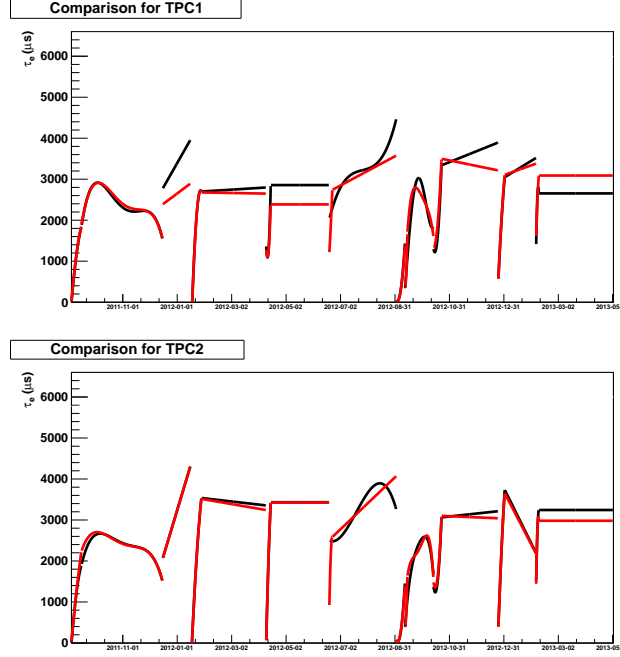


FIG. 37: The comparison between the electron lifetime fits for two different sets of excluded runs. The fit from Figure. 35 is in red, and the fit from Figure. 36 is in black. The two fits qualitatively agree. Currently the fits shown in black are being used for correcting the low-background data.

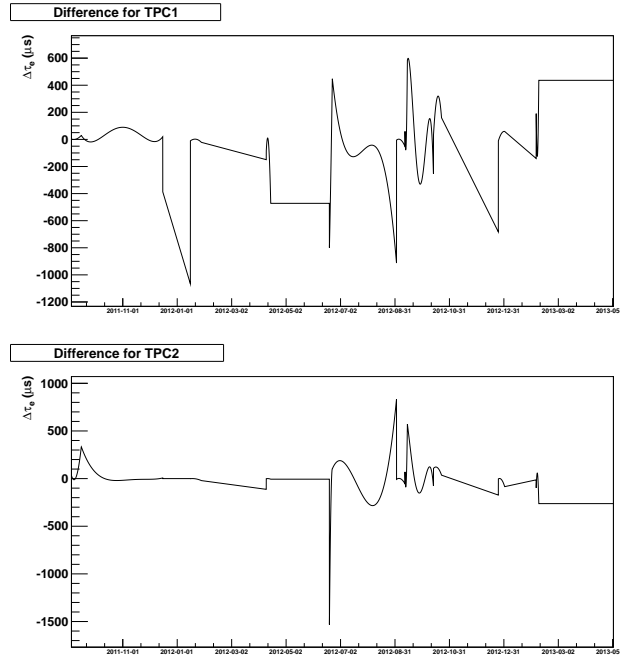


FIG. 38: The difference between the electron lifetime fits for two different sets of excluded runs. The differences between the two fits are typically between  $\pm 500 \mu s$ .

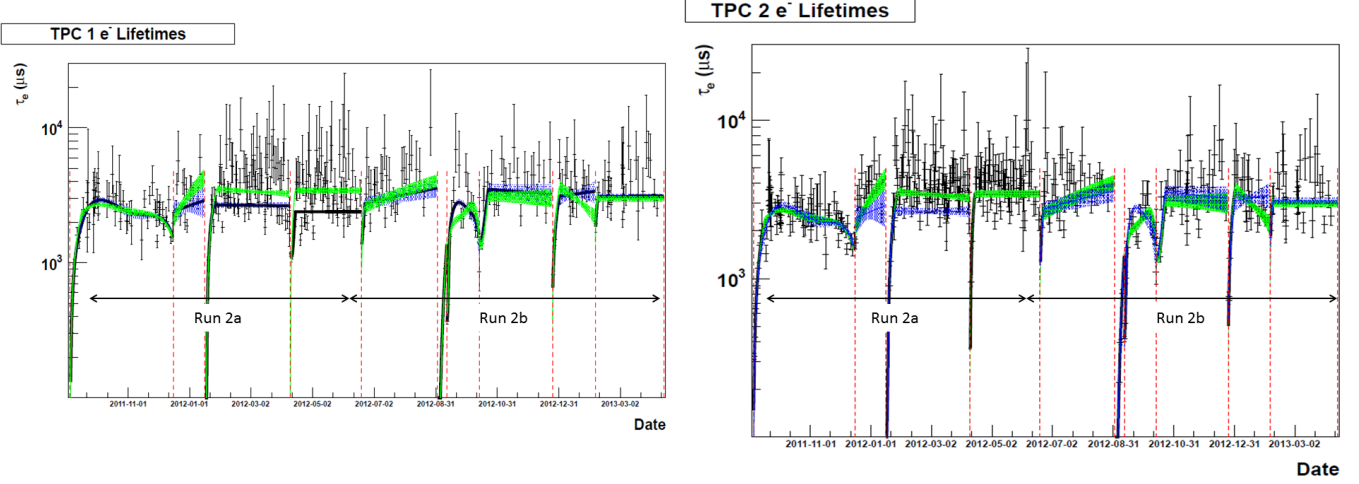


FIG. 39: The most up to date fit of a piecewise polynomial to electron lifetime in TPC 1(left) and TPC 2 (right). The blue bands show the 68% confidence interval for TPC1 and the green bands show the 68% confidence interval for TPC2. Run 2a is defined as data taken from September 22, 2011 through April 15, 2012. Run 2b is defined as data taken from April 16, 2012 to the present (currently April 8, 2013.)

## V. LIGHT MAP AND CORRECTIONS

### A. APD gain measurement

The APD gain correction was not applied in this analysis. However, for the integrity of this document, a brief description about the APD gain measurement is as below.

In order to measure the APD gain, in each LAAPD array one APD device is replaced with a teflon diffuser ball which can be illuminated by an external laser pulser fed through optical fibers. Such laser pulser is used to measure APD gang gains periodically. The measurement consists four steps:

- The APDs are biased at their operating values. The laser is pulsed at low frequency ( $\sim 10$  Hz), and a relative large pulse width (190 ns) without saturating any APD gang.
- Keep the laser pulser configuration. Lower the APDs biases to be their nominal values.
- Keep the APDs biases. Increase the laser pulse width to 750ns.
- Keep the laser pulse configuration. Lower the nominal APDs biases to -300 V, which is corresponding to roughly the unity gain.

For each step, the laser pulser takes 6000 pulses. For step 1 and 4, the raw waveforms for each APD gang are averaged and the amplitude of each channel is extracted by subtracting the waveform baseline from the waveform peak. For step 2 and 3, the waveforms for all channels are averaged together. The amplitudes measured in each step are  $A_1$ ,  $A_2$ ,  $A_3$  and  $A_4$ . Then the laser gain is measured as  $\frac{A_3}{A_2}$ , the gain of each APD gang is calculated as  $\frac{A_1}{A_4} \cdot \frac{A_3}{A_2}$ .

The measured relative gains for each APD gang are shown in Figure 40. Since the fiber enters the TPC on the north end (TPC1, with channel number > 188), so the TPC on the south (TPC2) sees the diffuse laser beam directly, whereas the TPC1 sees reflected light only. As a result, the gain measurements on TPC1 are noisier than TPC2. The observed gain variation between channels is about 12%. The time variation on each channel is around 1%.

In this analysis, the APD gain correction is not separately corrected. Instead, the correction is absorbed in the light map correction described below.

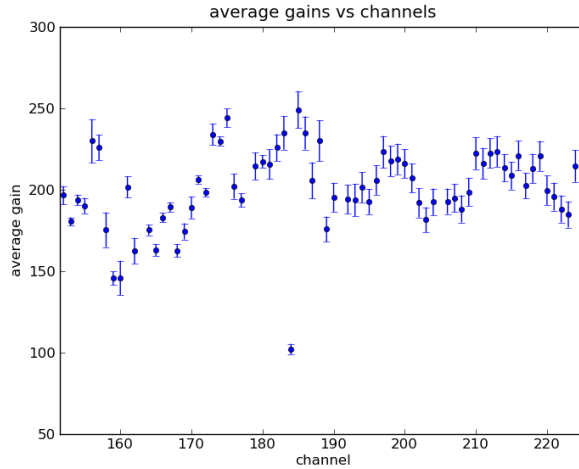


FIG. 40: The measured relative gains for each APD gang channel.

### B. Building the light map

In brief, the method of APD light map correction is almost the same as last  $0\nu\beta\beta$  analysis (refer to Working Document 2). An overview for the APD light map correction is as below.

### 1. Calibration Runs

In principle, in order to illuminate the entire detector, long calibration runs at both anode positions and all three cathode locations are needed. These runs are taken as part of larger calibration campaigns, or whenever electronic components are changed or adjusted in a way that might affect the APD response.

In this study, all the Thorium runs from run 2426 to run 4877 with a good purity measurement (electron lifetime  $>1$  ms) are used for lightmap building. In order to track the potential time-variation, the selected Thorium data set is divided into 4 periods, as listed below (the times are in UTC time):

- Period A: From 2011/10/1 1:00 to 2012/2/20 15:00
- Period B: From 2012/2/20 15:00 to 2012/4/23 17:00, a new period when we swapped an APD electronics board
- Period C: From 2012/4/23 17:00 to 2012/9/28 18:00, splitting at the end of September is just to balance the statistics.
- Period D: From 2012/9/28 18:00 to 2019/12/30 17:00

One thing should be mentioned that, for the later two periods, the calibration data is dominated by the runs near S5. Thus in some sense it violates above principle. However, the as-built lightmaps visually show small differences.

### 2. Event Selection

Only single site full-absorption events are used to make the light map, since both their location and energies are known. Full absorption events are identified by looking at the ionization spectrum. The mean and sigma of the full-absorption peak are fit with a Gaussian + complementary error function model like that used for calibration. Only events with ionization energies between  $+0.33\sigma$  and  $+3.0\sigma$  are used. This cut retains 37% of the full-absorption events, and should only retain 3% of the Compton scatter events with energies within  $2\sigma$  of the peak. Since scintillation is correlated with ionization, and the ionization response is uniform throughout the detector (after electron lifetime and shielding grid corrections), this should give a sample of events with the same scintillation throughout the detector.

### 3. Binning the Detector Volume

The detector volume is divided into 1352 spatial bins. This binning is split into 8  $\phi$  bins, 13 radial bins, and 13  $z$  bins. The  $\phi$  binning is evenly-spaced. For the  $z$  binning, the TPC is divided evenly into 11 slices. The central slice is then divided into 3 even slices, since the response is observed to change rapidly near the cathode. The radial binning consists of 1 bin from 0 mm to 3 mm, bins every 20 mm from 30 mm to 90 mm, bins every 10 mm from 90 mm to 120 mm, and bins every 8 mm from 120 mm to 168 mm. This binning is chosen to ensure adequate statistics within all bins, and to optimally map the response in regions with a high light collection gradient.

Full absorption, single site events from all calibrations are placed into the bins according to the event location. Then the mean of each bin is stored in a 3-dimensional histograms. This histogram stores the scintillation response in each bin of the detector and is referred to as the “light map”. It is stored in a database. The light maps for the four periods are shown in Figure. 41 and Figure. 42. Histograms of the number of events in each bin, and the error on the mean, are also retained to ensure an adequate amount of data was used.

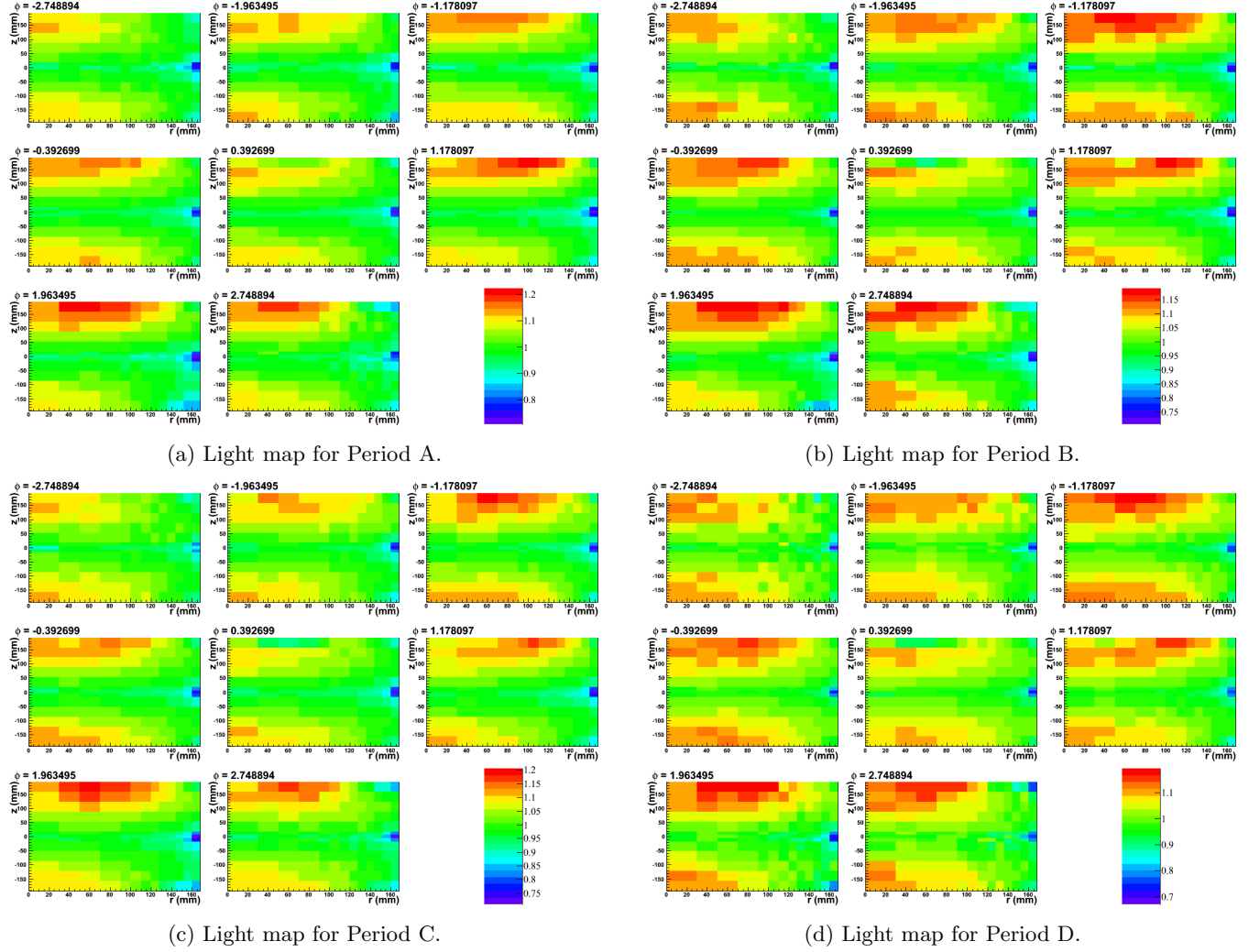


FIG. 41: The lightmaps, showing the bins in  $r$  (horizontal axis) and  $z$  (vertical axis) for each of the 8  $\phi$  bins. The four lightmaps (A, B, C, D) are corresponding to the four periods.

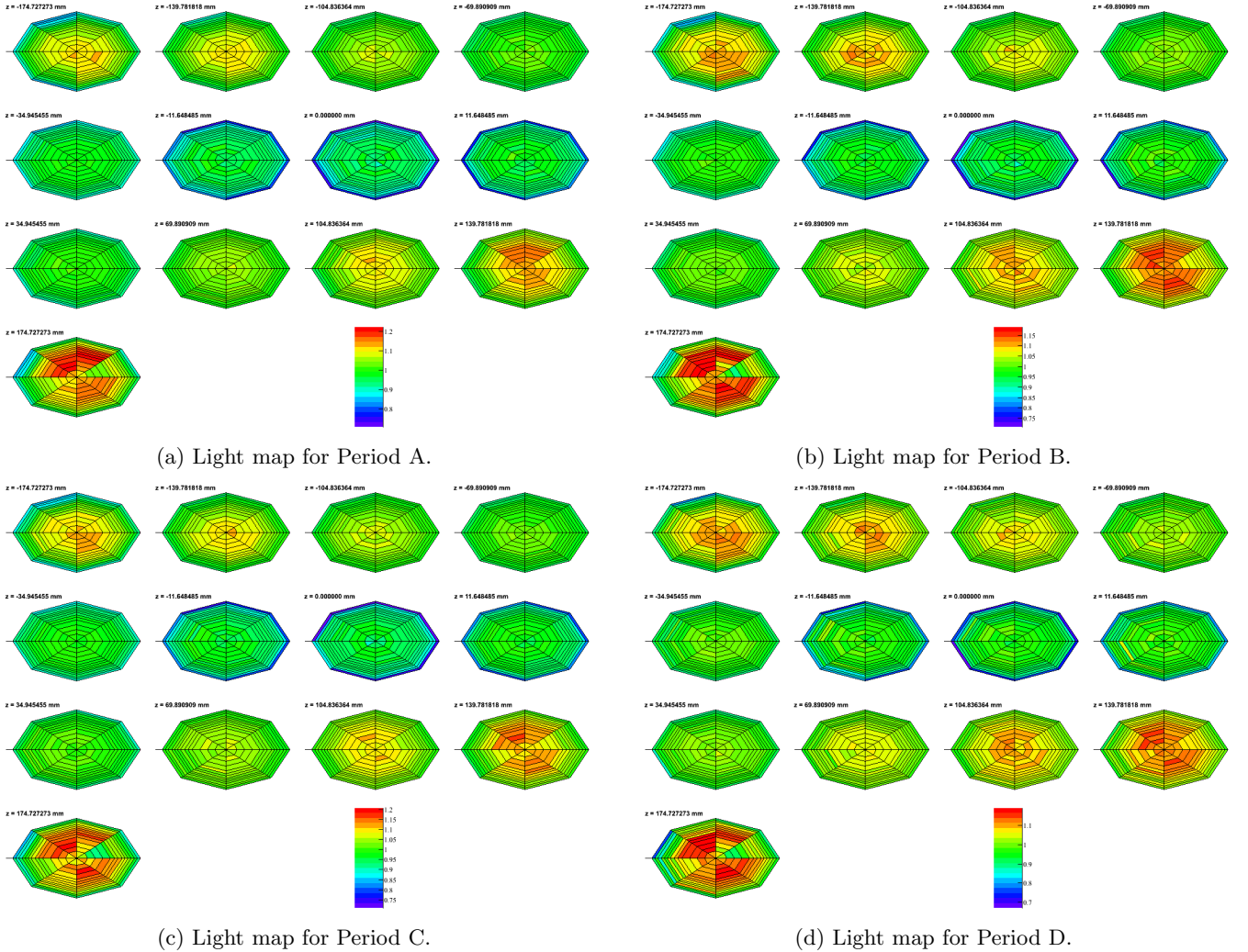


FIG. 42: The lightmaps, showing the bins in  $r$  and  $\phi$  for each of the 13  $z$  bins. The four lightmaps (A, B, C, D) are corresponding to the four periods.

### C. Correction Function

#### 1. Trilinear interpolation in cylindrical polar coordinates

Suppose a function  $F(r_i, \phi_j, z_k)$  is defined only at discrete points, and  $f(r, \phi, z)$  is a smooth transition between the defined points of  $F$ . The simplest way to do so is with trilinear interpolation. Define

$$r_d = \frac{r_{i+1} - r_i}{r_{i+1} + r_i}; \phi_d = \frac{\phi_{j+1} - \phi_j}{\phi_{j+1} + \phi_j}; z_d = \frac{z_{k+1} - z_k}{z_{k+1} + z_k} \quad (13)$$

where  $r_i \leq r < r_{i+1}$  and  $z_k \leq z < z_{k+1}$ . In cylindrical coordinates,  $\phi$  is cyclical, and so  $\phi$  lies between  $\phi_j$  and  $\phi_{j+1} \bmod 2\pi$ . Multiples of  $2\pi$  may need to be added or subtracted from the angles at which  $F$  is defined to ensure  $0 \leq \phi_d < 1$ .

Now  $f$  can be constructed:

$$\begin{aligned} f(r, \phi, z) = & F(r_i, \phi_j, z_k)(1 - r_d)(1 - \phi_d)(1 - z_d) \\ & + F(r_i, \phi_j, z_{k+1})(1 - r_d)(1 - \phi_d)z_d \\ & + F(r_i, \phi_{j+1}, z_k)(1 - r_d)\phi_d(1 - z_d) \\ & + F(r_i, \phi_{j+1}, z_{k+1})(1 - r_d)\phi_dz_d \\ & + F(r_{i+1}, \phi_j, z_k)r_d(1 - \phi_d)(1 - z_d) \\ & + F(r_{i+1}, \phi_j, z_{k+1})r_d(1 - \phi_d)z_d \\ & + F(r_{i+1}, \phi_{j+1}, z_k)r_d\phi_d(1 - z_d) \\ & + F(r_{i+1}, \phi_{j+1}, z_{k+1})r_d\phi_dz_d \end{aligned} \quad (14)$$

There is a complication, however, when the lower neighbor bin for  $r$  is the  $z$ -axis. In order to ensure that  $f$  is single-valued at  $r = 0$ , define the value of  $F$  at the axis as the mean value for the surrounding points:

$$F(r_0 = 0, \phi, z_k) = \frac{1}{N_\phi} \sum_{j=1}^{N_\phi} F(r_1, \phi_j, z_k) \quad (15)$$

Then can still be used. In this case,  $\phi_d$  will not matter in the terms involving  $r_i$ .

#### 2. Correcting for Light Response

To correct for the light response, first the histogram containing the light map is normalized such that the average response is 1. Let  $F(r_i, \phi_j, z_k)$  be the value of the normalized light map for the bin that has center  $(r_i, \phi_j, z_k)$ . Then let  $f(r, \phi, z)$  be the trilinear interpolation of  $F$ . show an example of this interpolation. The normalized scintillation response for an event is

$$g = \frac{\sum_{m=1}^N E_m f(r_m, \phi_m, z_m)}{\sum_{m=1}^N E_m} \quad (16)$$

where the sums are over the  $N$  ionization clusters in the event, each with a position  $(r_m, \phi_m, z_m)$  and an ionization energy  $E_m$ . This assumes that the fraction of total scintillation light produced by a charge cluster at a given position is the same as that cluster's fraction of total ionization energy.

If  $E_s$  is the uncorrected scintillation signal, then

$$E_{s,\text{corrected}} = \frac{E_s}{g} \quad (17)$$

is the corrected signal.

Table. XI shows the improvement in the scintillation-only energy resolution for calibration data taken with a  $^{228}\text{Th}$  source at several positions around the detector. The runs were taken about the same time, thus they're a good representation of the improvement. The mean improvement in  $\sigma/E$  was 2.0 % for single site events, and 1.8 % for multiple site data. An example of the improvement is shown in Figure. 45. One thing need be mentioned that, the resolution numbers in Table. XI may not be a good representation of the overall scintillation resolution for the entire time period because of the time variation caused by APD noise, which will be discussed in section VIC.

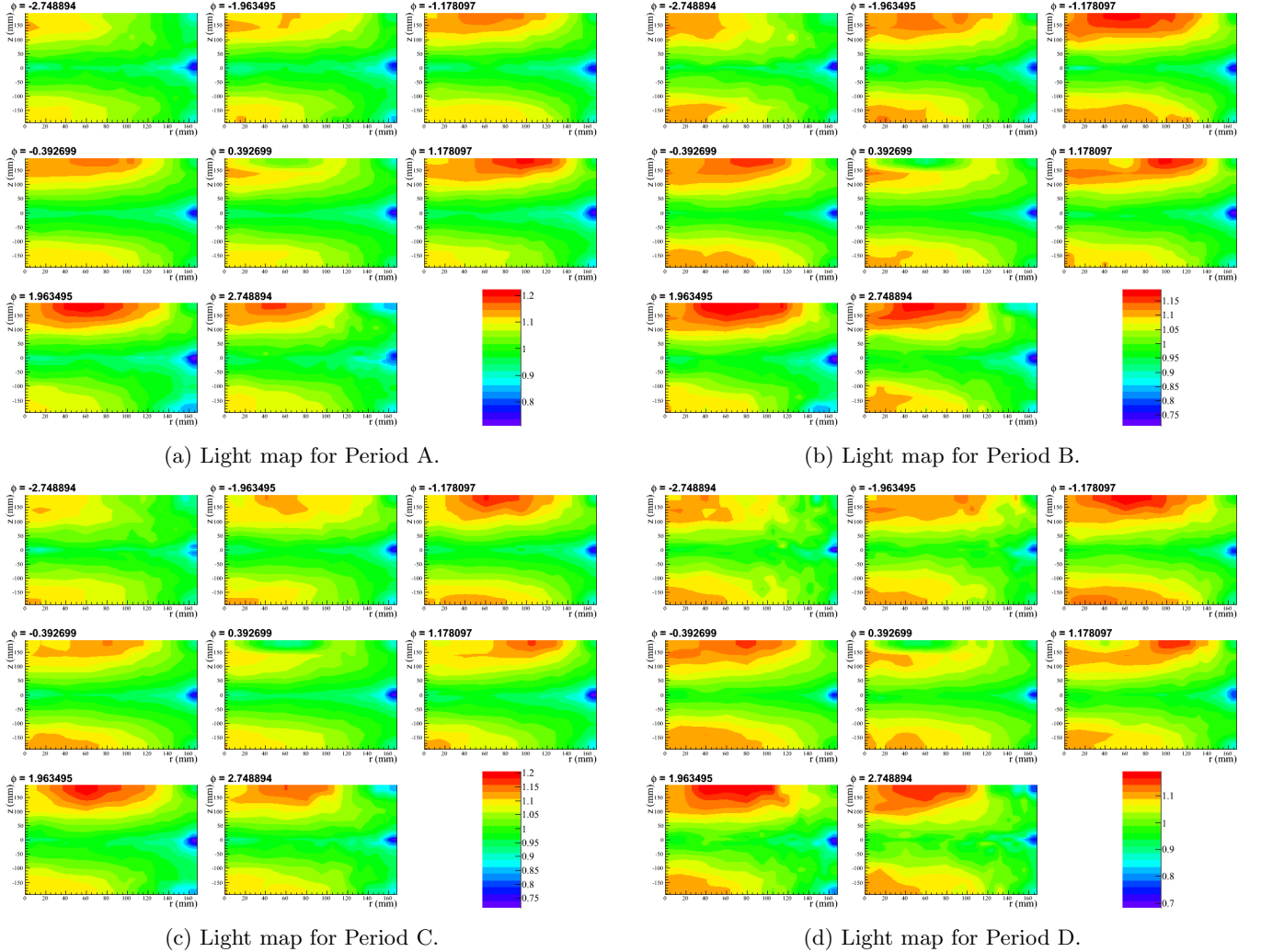
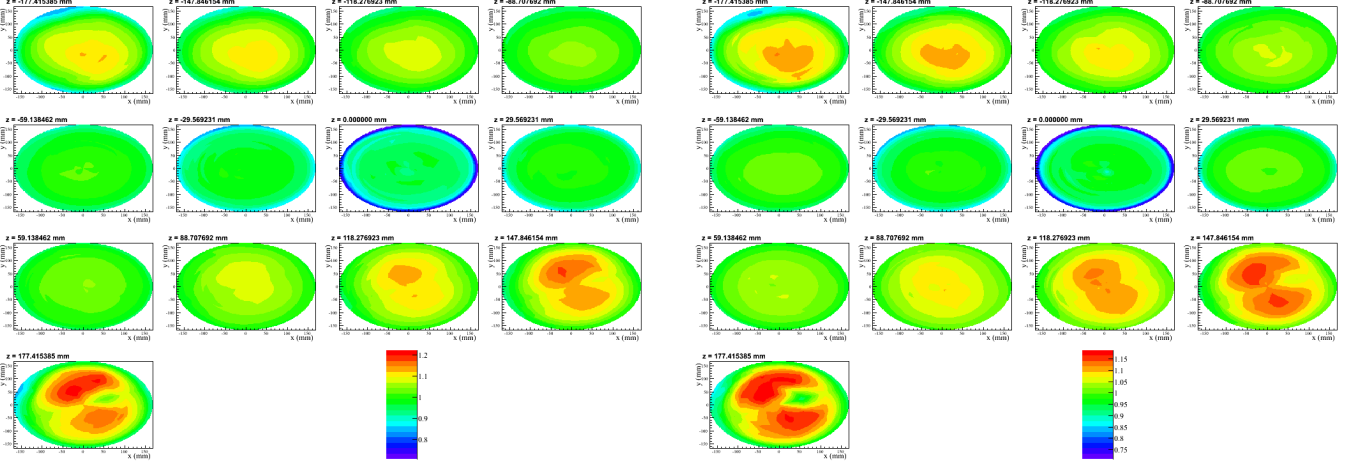


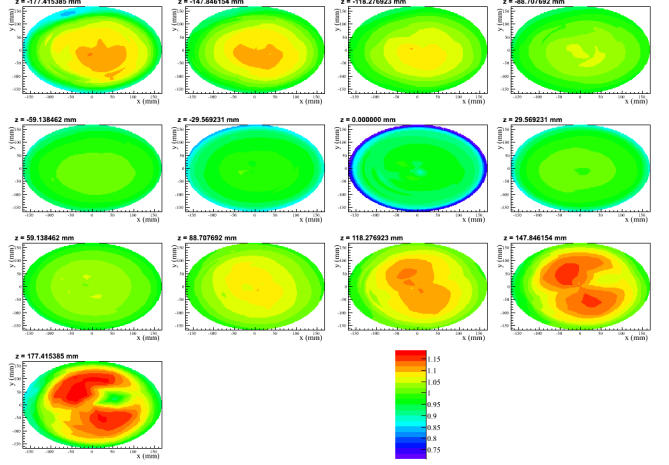
FIG. 43: The light response functions  $f(r, \phi, z)$ , evaluated at 8 discrete values of  $\phi$  over the full range of  $r$  (horizontal axis) and  $z$  (vertical axis). The four lightmaps (A, B, C, D) are corresponding to the four periods.

TABLE XI: The improvement in the scintillation-only energy resolution ( $\sigma/E$ ) after applying the correction for both single site (SS) and multiple site (MS) events. This is based on fitting a Gaussian + complimentary error function model to  $^{228}\text{Th}$  calibration data taken at a number of positions.

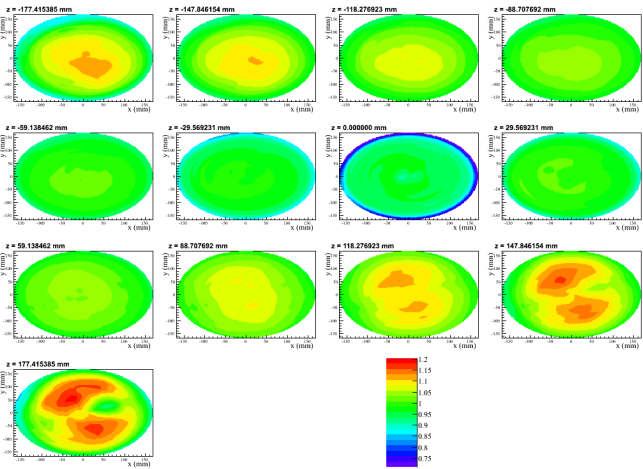
Run Number	Source Position	Multiplicity	$\sigma/E$ without correction (%)	$\sigma/E$ with correction (%)
2719, 2737	cathode	+x	SS $8.01 \pm 0.18$	6.13 $\pm 0.12$
2785, 2817, 2837		+x	MS $8.03 \pm 0.08$	6.33 $\pm 0.06$
2865	cathode	+y	SS $8.73 \pm 0.28$	6.09 $\pm 0.16$
		+y	MS $8.99 \pm 0.12$	6.49 $\pm 0.08$
2866, 2867	cathode	-y	SS $8.17 \pm 0.24$	5.94 $\pm 0.15$
		-y	MS $8.48 \pm 0.15$	6.64 $\pm 0.07$
2725, 2743	anode	+z	SS $7.65 \pm 0.26$	5.89 $\pm 0.14$
2766, 2804, 2828		+z	MS $7.86 \pm 0.09$	6.03 $\pm 0.06$
2714, 2732	anode	-z	SS $7.21 \pm 0.21$	5.95 $\pm 0.14$
2748, 2771, 2811		-z	MS $7.56 \pm 0.10$	6.21 $\pm 0.08$



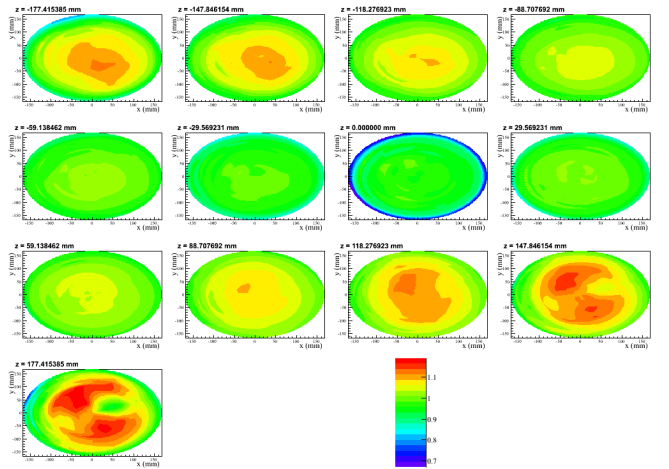
(a) Light map for Period A.



(b) Light map for Period B.



(c) Light map for Period C.



(d) Light map for Period D.

FIG. 44: The light response function  $f(r, \phi, z)$ , evaluated at 13 discrete values of  $z$  over the full range of  $x$  (horizontal axis) and  $y$  (vertical axis). The four lightmaps (A, B, C, D) are corresponding to the four periods.

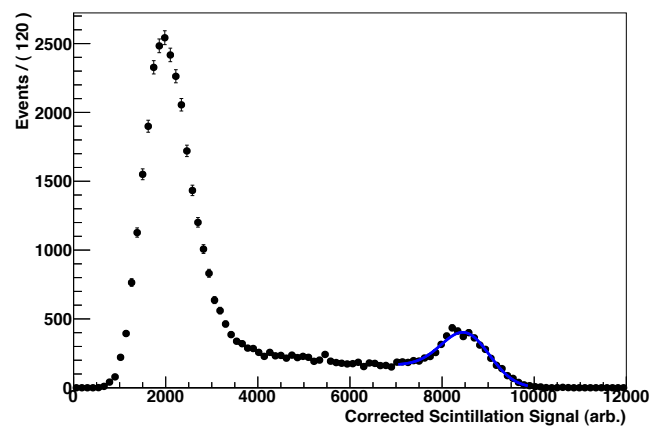
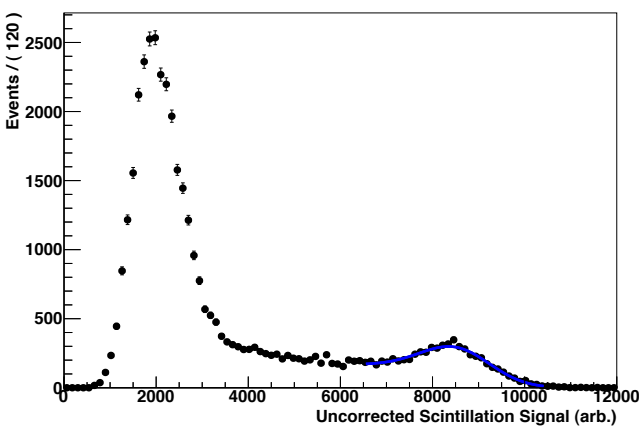


FIG. 45: The scintillation energy spectrum for a  $^{228}\text{Th}$  source at the cathode in the  $+y$  position. The uncorrected spectrum (left) has  $\sigma/E = 8.7\%$ . The corrected spectrum (right) has  $\sigma/E = 6.1\%$ .

#### D. Residual Dependence Check

The residual dependence after the lightmap correction has been checked using alpha events in the TPC. The alpha events are selected by requiring the scintillation energy  $>30,000$  (un-calibrated unit). Fig. 46 shows the sum of APD gangs and sum of APD plane signals versus Z distribution before light map correction. Fig. 47 is the lightmap corrected energy versus Z distribution. The remaining z-dependence is  $\sim 5\%$ .

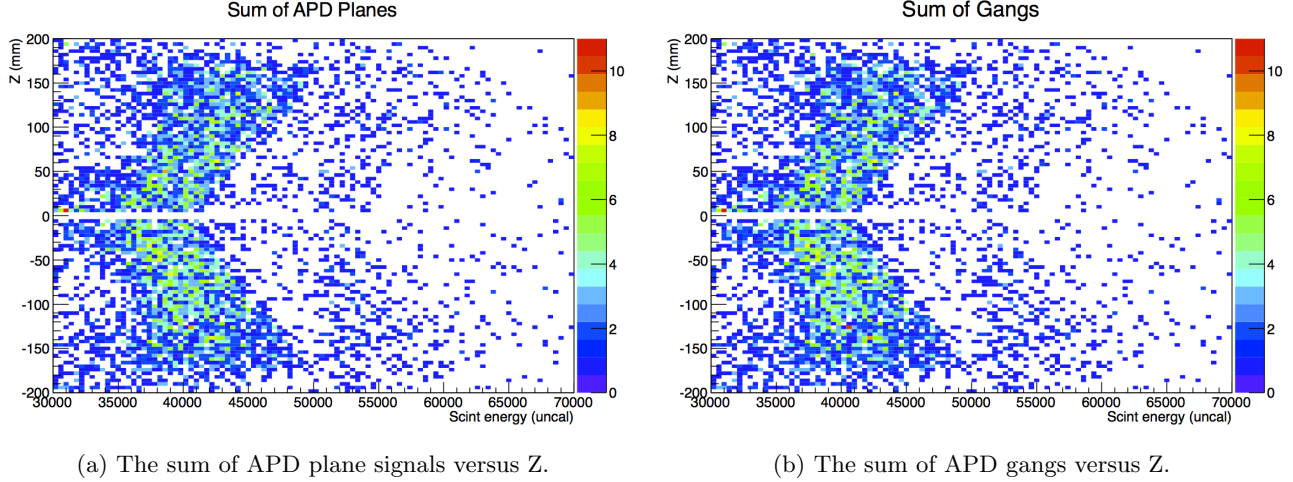


FIG. 46: The sum of APD gangs and sum of APD plane signals versus Z position distribution.

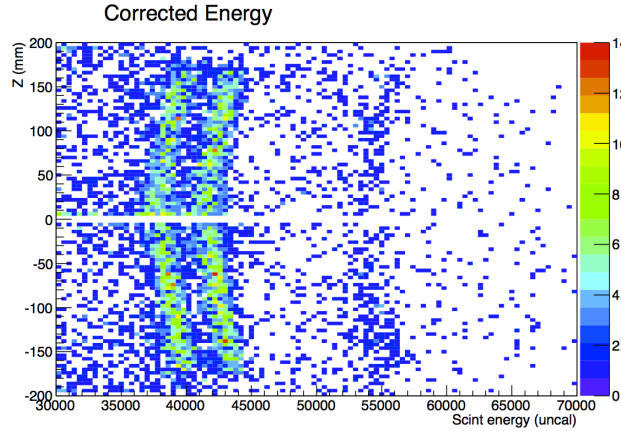


FIG. 47: The lightmap corrected energy versus Z distribution. A residual z-dependence of  $\sim 5\%$  can be seen.

There was an earlier study done by Bill Fairbank, using alpha events to provide a check of light map. It was found the variation in  $R$  and  $\phi$  direction is less than 1%, but not as good in  $Z$ . Below are some details about Bill's study.

The fits to scintillation energy spectra were done to groups in  $R$ ,  $Z$  and  $\theta$  for the  $^{222}\text{Rn}$  and  $^{218}\text{Po}$  alpha peaks. The regions were similar to those used by Steve, except that data was compressed into one dimension of 8  $\phi$  bins or 13 radial bins, instead of 1352 voxels. The fitting function used is as below:

$$y = m_1 \cdot e^{-\left(\frac{x-m_6 \cdot 5990}{m_7 \cdot \sqrt{5990}}\right)^2} + m_2 \cdot e^{-\left(\frac{x-m_6 \cdot 6115}{m_7 \cdot \sqrt{6115}}\right)^2} \quad (18)$$

where it assumes the scintillation is proportional to the  $Q$  value of alpha decay and the resolution is proportional to  $\sqrt{Q}$ . Fig. 48a is the spectrum of all the data within  $0 < R < 160$ ,  $6 < Z < 182$  and  $-\pi < \theta < \pi$ . The uniformity of the parameter  $m_6$ , the proportionality scale factor for scintillation versus  $Q$ , gives a measurement of how well the light map correction is performed. The scale factors, normalized to the value in Fig. 47, are plotted versus  $R$ ,  $Z$  and  $\theta$  in Fig. 48b to Fig. 48d. The corrections in  $R$  and  $\theta$  seem to be very good, agreeing to  $<1\%$ . However, a several

percent variation in  $Z$  was found. It is also found that the resolution of  $Z$ -slices is significantly better than that of the average in Fig. 47 due to the variation of the scale factor with  $Z$ .

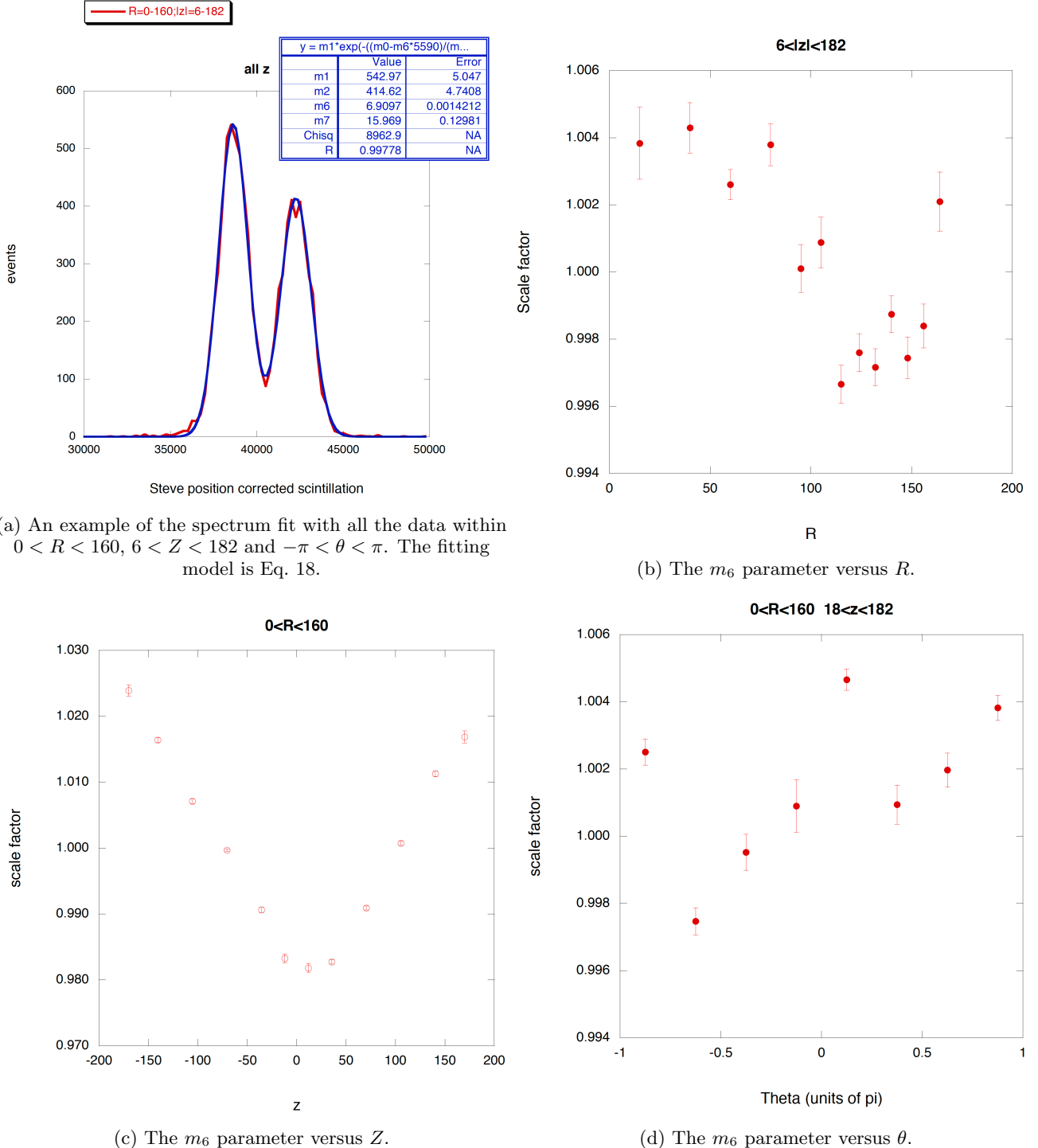


FIG. 48: The uniformity of the parameter  $m_6$ , the proportionality scale factor for scintillation versus  $Q$ , is plotted versus  $R$ ,  $Z$  and  $\theta$

A plot of charge versus scintillation for alpha events with and without a V-wire signal in Fig. 49 shows that there is little difference in the electron distribution. It may indicate the lack of V-wire identification in 35% of these events have something to do with how the electron cloud passed through the V-wires and how well the induction signal was

reconstructed. For these events with no V-wire signal, the light map correction is not very effective, as might be expected.

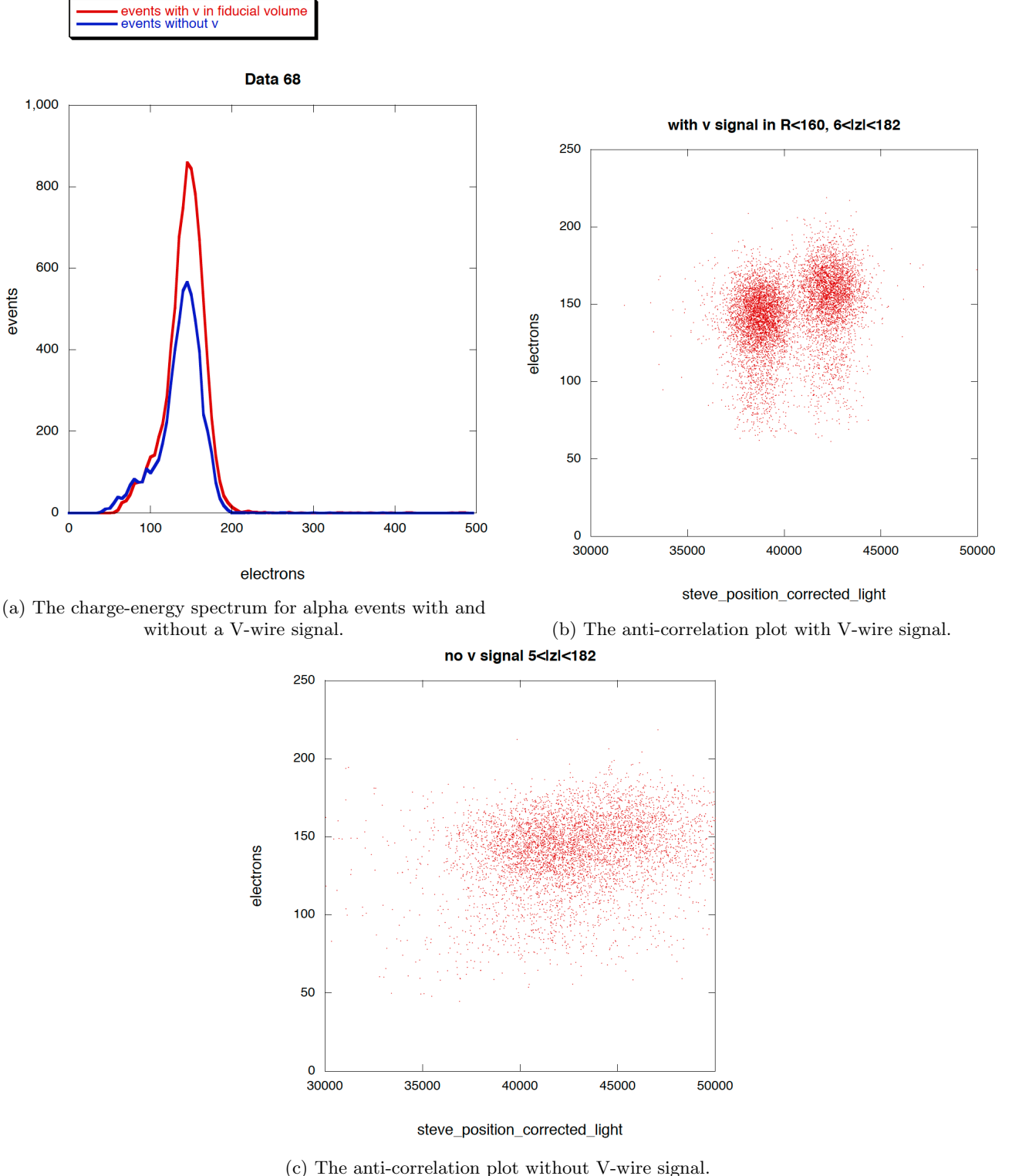


FIG. 49: The anti-correlation between charge and scintillation for alpha events, with and without a V-wire signal in the fiducial volume. Here the fiducial volume cut is  $0 < R < 160, 6 < Z < 182$ , a bit different from the standard fiducial volume cut in this  $2\nu\beta\beta$  analysis.

## VI. ANTI-CORRELATION AND TIME VARIATION CORRECTIONS

### A. Calibration Sources

The EXO-200 detector are calibrated using three radioactive sources ( $^{137}\text{Cs}$ ,  $^{60}\text{Co}$ ,  $^{228}\text{Th}$ ) at two strengths each. The source rates are listed in Table.XII. The activities of the weak sources were set according to the maximum tolerable event rate of DAQ system. The strong sources were used to enhance the rates of events under energy peaks.

TABLE XII: Source certificates data.

source	Contained Radioactivity	Half-life
$^{137}\text{Cs}$ strong	13.14 kBq	$30.17 \pm 0.16$ y
$^{137}\text{Cs}$ weak	2820 Bq	$30.17 \pm 0.16$ y
$^{60}\text{Co}$ strong	7.060 kBq	$5.272 \pm 0.001$ y
$^{60}\text{Co}$ weak	529.5 Bq	$5.272 \pm 0.001$ y
$^{228}\text{Th}$ strong	34.04 kBq	$698.2 \pm 0.6$ d
$^{228}\text{Th}$ weak	1417 Bq	$698.2 \pm 0.6$ d

Weak  $^{228}\text{Th}$  source were deployed every a few days for electron lifetime measurement and energy calibration purpose. A position near the cathode was chosen as the routine  $^{228}\text{Th}$  source deployment position. Due to the complexity of changing calibration sources, the  $^{60}\text{Co}$  and  $^{137}\text{Cs}$  sources were deployed every a few months to perform a comprehensive calibration campaign for energy calibration studies:

- $^{60}\text{Co}$  source: deployed in September and October, 2011; March and November, 2012; February, 2013.
- $^{137}\text{Cs}$  source: deployed in October, 2011; November, 2012; February, 2013.

### B. Anti-correlation

The measured scintillation and ionization energies are anti-correlated. The 2D SS and MS energy spectra are independently rotated and projected onto a 1D energy variable  $E_R$ :

$$E_R = E_S \cdot \sin(\theta^R) + E_I \cdot \cos(\theta^R) \quad (19)$$

where  $E_S$  and  $E_I$  are the energies measured in scintillation and ionization channel respectively,  $\theta^R$  is the rotation angle,  $E_R$  is referred as rotated energy. **In this analysis, the determination of  $\theta^R$  is to achieve the best resolution of  $E^R$  at the  $^{228}\text{Th}$  full-absorption  $\gamma$  line.**

In practice, by scanning the  $\theta^R$  value, the resolution of the 2615 keV  $\gamma$  line from  $^{228}\text{Th}$  source is observed to have a minima. Then taking into account the fitting error on resolution, a parabolic fit is performed near the minima to determine the optimal  $\theta^R$ . Apparently, such anti-correlation method significantly improves the energy resolution. However, two issues need be addressed:

- Is the  $\theta^R$  determined from  $^{228}\text{Th}$  data also optimal for different  $\gamma$  lines (e.g,  $^{60}\text{Co}$  and  $^{137}\text{Cs}$ ) and different particles (e.g,  $\alpha$ 's from  $\text{Bi} - \text{Po}$  cascade decay)?
- Can a single set of parameters correctly calibrate the energy of  $\beta/e^+$ ,  $\gamma$  and  $\alpha$  particles? If not, how to estimate the difference between energy scales and its uncertainty?

Such two issues will be discussed later.

### C. Time variation correction

#### 1. Time dependent rotation angle

Due to gain variation, noise fluctuation, etc, the resolution in either ionization or scintillation channel varies versus time. The energy resolution history for Th calibration runs is shown in Fig.50, where the Th calibration runs in a week are combined. The ionization-only and scintillation-only energy spectra are both fit with a Gaussian plus complimentary error function model. The ionization-only energy resolution is quite stable versus time and, the

average resolution is  $3.53\% \pm 0.06\%$  ( $4.11\% \pm 0.05\%$ ) for SS (MS) events, respectively. The jump in late June, 2012 is due to the bad Xenon purity caused by a power outage event. The scintillation-only energy resolution has much larger time variation. It's found to be correlated with the time variation of coherent noise on APD channels, as shown in Fig. 51. In Fig. 51a, it shows the coherent noise for each APD front-end electronics board as a function of time. A noisy APD board (named as APD00) was replaced at the end of February, 2012, immediately leading to a better resolution in scintillation channel, as shown in Fig. 50. Afterwards, the coherent APD noise slowly increases, leads to the slow degeneration of resolution. The source causing the coherent APD noise is not quite clear by the time this note is written.

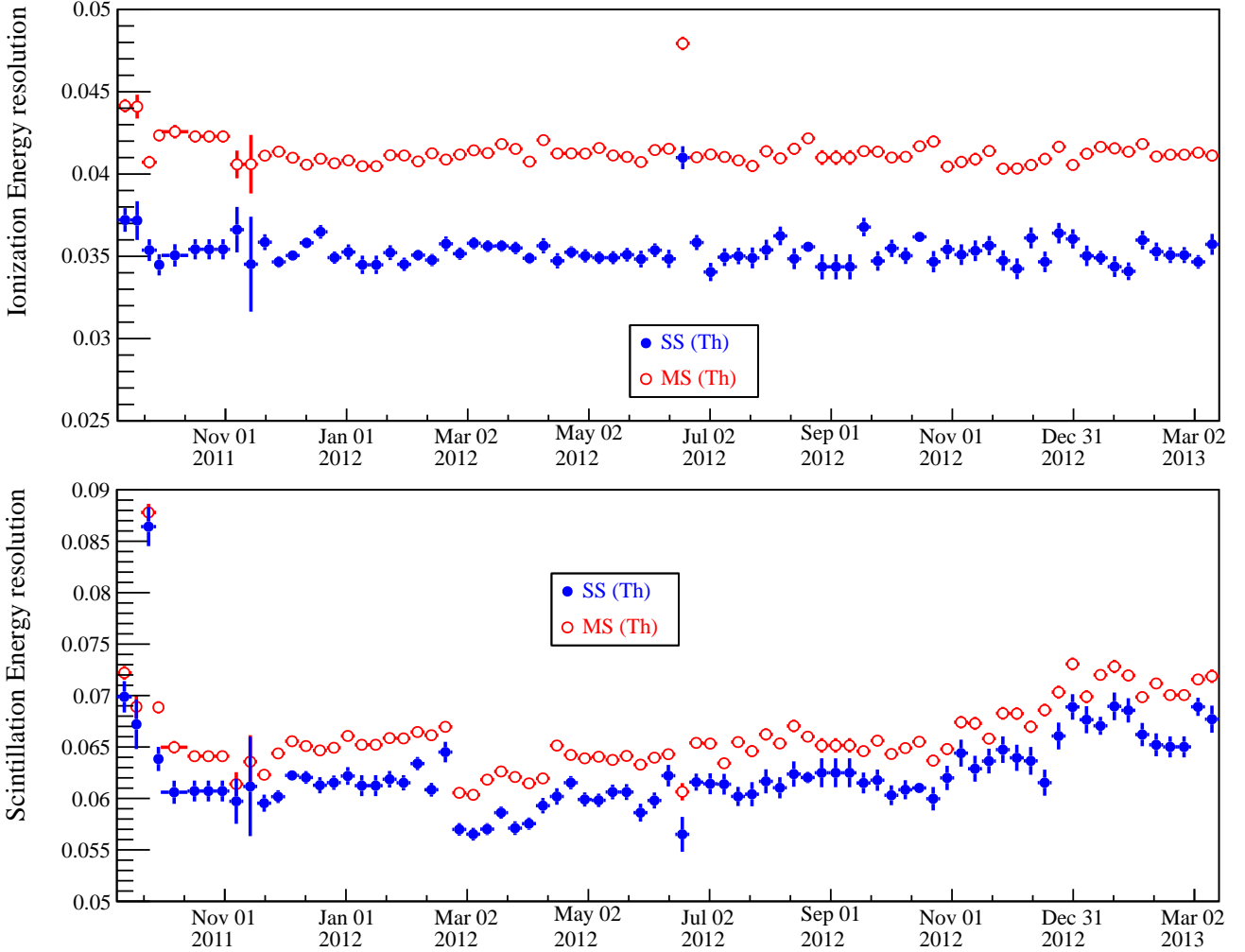


FIG. 50: Ionization only and scintillation only resolution at 2615keV  $\gamma$  of  $^{228}\text{Th}$  source. Each data point combines the  $^{228}\text{Th}$  runs (with a measured electron lifetime  $>1$  ms) in a week.

Since the optimal  $\theta^R$  is essentially determined by the resolution of scintillation signal and ionization signal. If the energy resolution in scintillation signal is getting worse, according to Eq. ??, the optimal  $\theta^R$  will decrease for both SS and MS events. The time dependent rotation angles are shown in Fig. 52. The shaded periods represent the time that we did not deploy  $^{228}\text{Th}$  sources ('empty' calibration periods). There are two ways to estimate the optimal rotation angles for those periods. One is to combine the  $^{228}\text{Th}$  runs in two nearest weeks to calculate an optimal rotation angle, e.g, for the period in Oct, 2012. The other way is to directly take the rotation angle in the closest week as an approximation, e.g, the other three shaded periods in 2012. The rotated energy resolution is shown in Fig.53. A clear correlation between the APD noise and rotated energy resolution is observed by comparing Fig. 51 and Fig. 53.

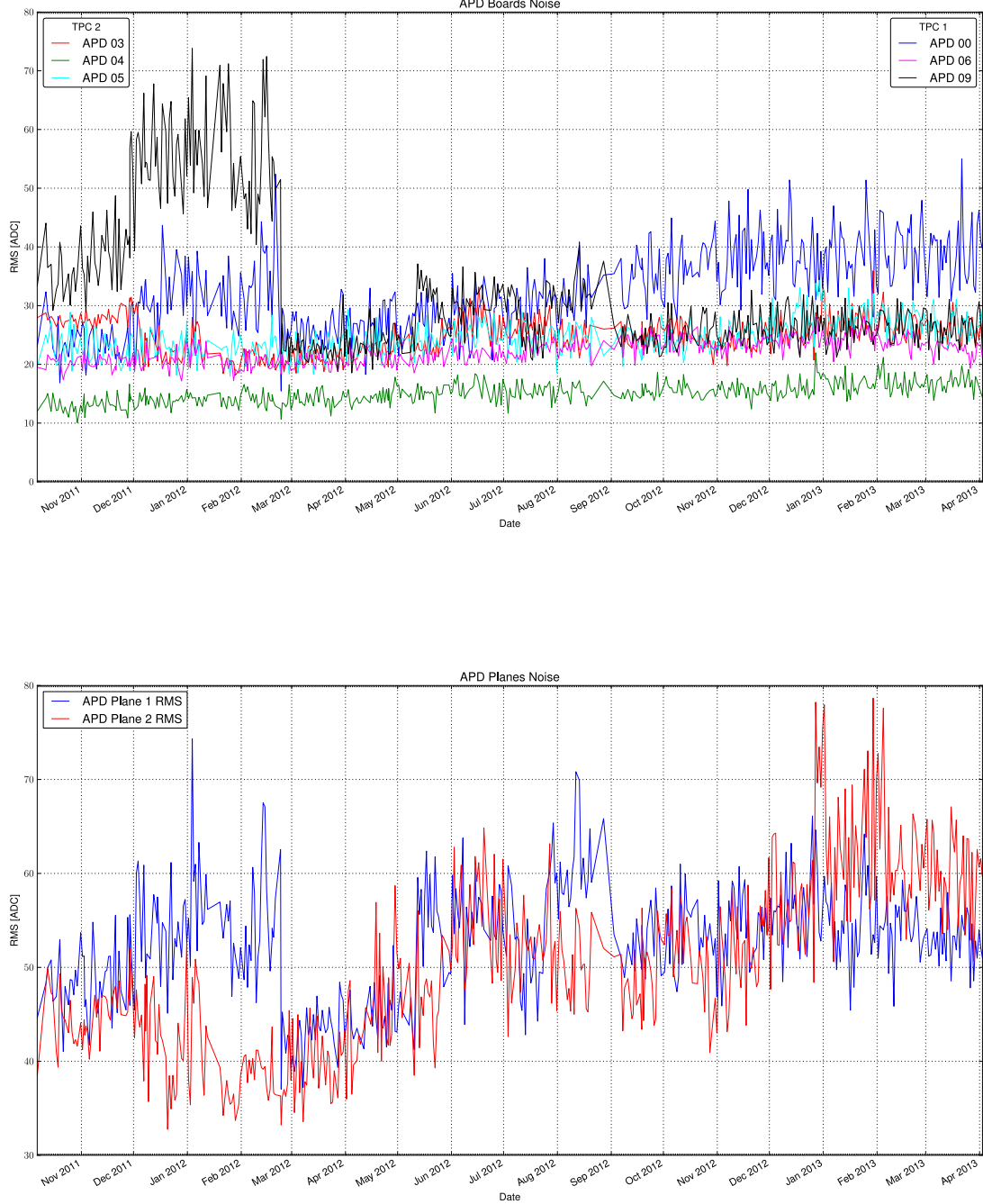


FIG. 51: APD coherent noise history. Top (a): the coherent noise for each APD front-end card. Bottom (b): the coherent noise for APDs in each TPC.

At the beginning of last  $0\nu\beta\beta$  data set (from Sep.21, 2011 to Apr.15, 2012), there were a few changes on operating the detector, as shown in the Fig. 54. It's a zoom-in of Fig. 52, focusing on the last  $0\nu\beta\beta$  data set:

- U-wires shaping time changed on Sep.21, 2011 (long dashed line)
- APD bias voltage changed on Sep.28, 2011 (dotted line)

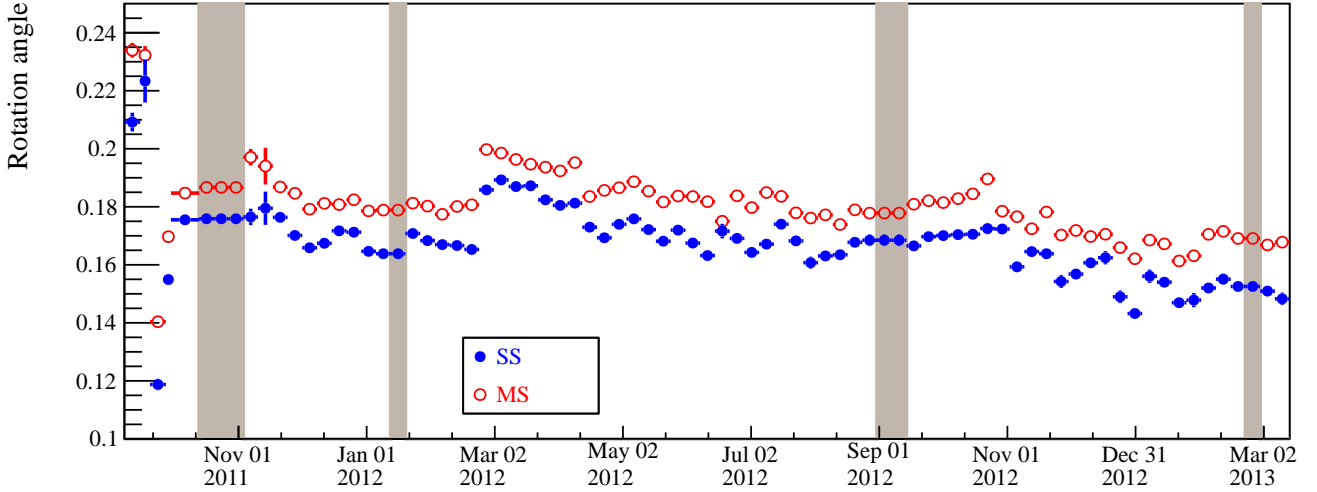


FIG. 52: Optimal rotation angle up to Mar, 2013. Such rotation angle is determined by achieving the best energy resolution in the rotated space. The shaded periods represent the time that we did not deploy  $^{228}\text{Th}$  sources ('empty' calibration periods).

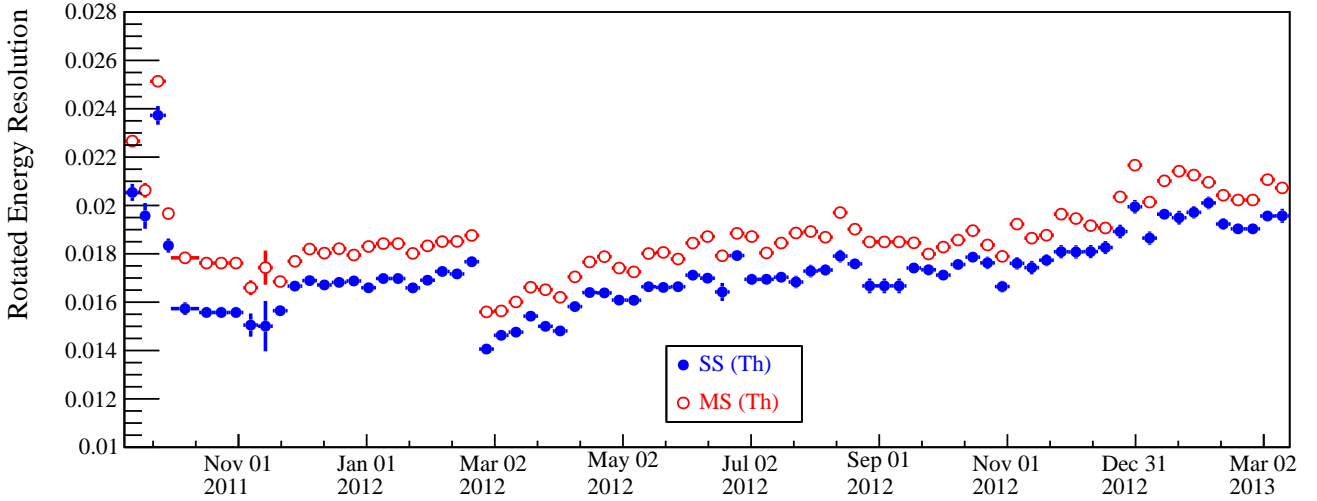


FIG. 53: Rotation energy resolution at 2615keV  $\gamma$  of  $^{228}\text{Th}$  source.

- APD bias voltage changed on Sep.30, 2011 (dash-dotted line)

Since such hardware changes or detector operation changes will change the amplitude of ionization or scintillation signals. The periods between these changes are taken as separate calibration periods. With the time-depended rotation angles, the rotated energy peaks (un-calibrated) at the 2615 keV  $\gamma$  line is shown in Fig. 55. The time periods for different calibration campaigns using  $^{60}\text{Co}$  and  $^{137}\text{Cs}$  sources are also marked out. Those data can be used to check whether the apparent time variation on the  $^{228}\text{Th}$  peak is the same at lower energies. A natural way is to check the ratio of un-calibrated energy peaks at 662 keV, 1173 keV and 1333 keV to the peak at 2615 keV, as described below.

## 2. Energy Ratio and Time Variation Correction

As shown in Fig. 55, till March 2013, there are 4  $^{60}\text{Co}$  calibration campaigns and 3  $^{137}\text{Cs}$  calibration campaigns. Each point represents a calibration period. Using the corresponding rotation angle in each calibration period, the un-calibrated energy peaks at  $^{60}\text{Co}$   $\gamma$  lines can be calculated, as shown in Fig. 56. Though the  $^{60}\text{Co}$  data is limited, a clear time variation is observed. However, the ratio of  $^{60}\text{Co}$  peaks to  $^{228}\text{Th}$  peak has much less variation, as shown

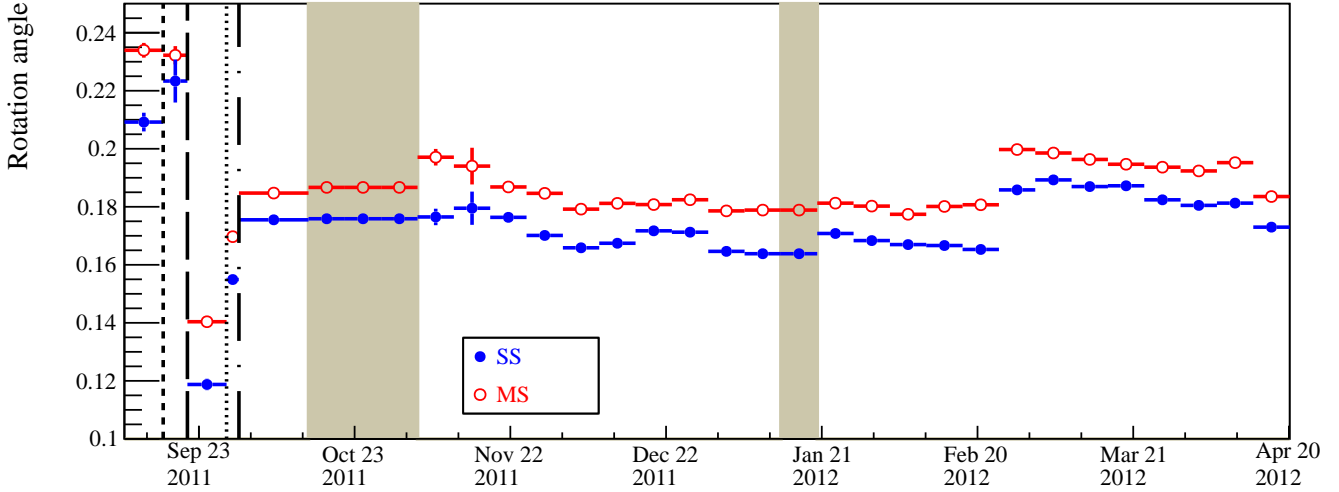


FIG. 54: Rotation angle in bb0n data set (from Sep.21, 2011 to Apr.15, 2012).

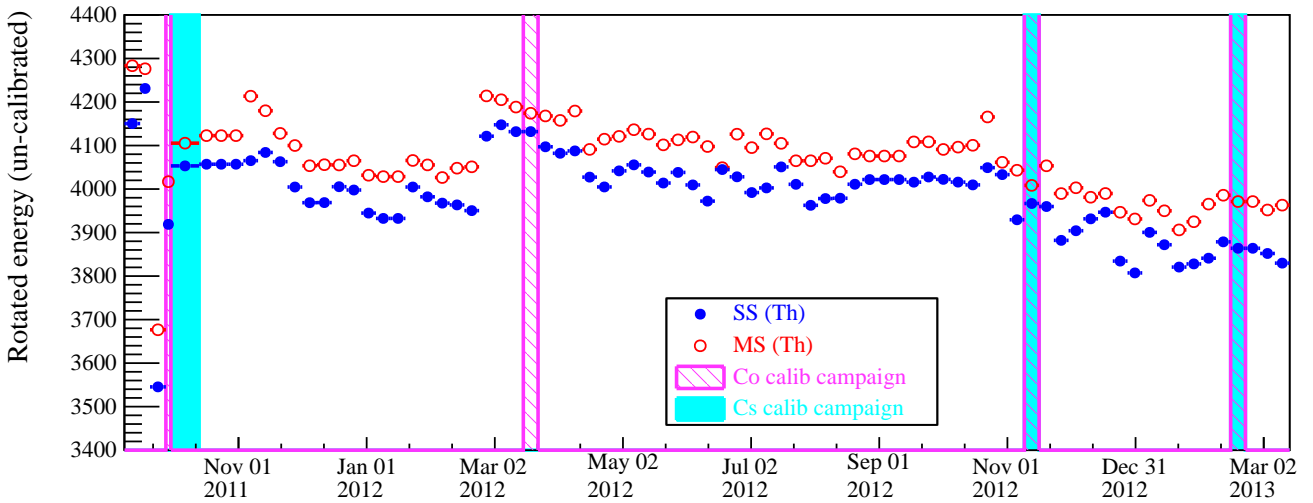


FIG. 55: Rotated energy (un-calibrated) peak of  $^{228}\text{Th}$  source. The used rotation angles are shown in Fig. 52. The time periods for different calibration campaigns using  $^{60}\text{Co}$  and  $^{137}\text{Cs}$  sources are also marked out.

in Fig. 57, indicating that the time variation can be largely canceled by using this ratio. The same strategy can be done for  $^{137}\text{Cs}$ , as shown in Fig. 58. The ratio values are summarized in Table. XIV. For the calibration purpose, the energy ratio values are regarded as constants and the RMS values throughout all existing calibration campaigns as the ratio uncertainties.

From MC, it is known that the fitted peak (using a Gaussian plus complementary error function model) has a small bias relative to the true  $\gamma$  energy. One reason is the Compton shelf on the left side of the full-absorption peak, the other reason is the fitting model itself. Such biases also slightly depend on energy resolution, as discussed in Working Document Run2, section 6.6.2. However, within the observed time variation of energy resolution, the bias values change very small. In addition, when the calibration sources are at different positions, the component of Compton shelf in the spectrum has slightly different. It causes small differences on the bias values, as shown in Fig. 59. In the end, the bias values and energy ratios in MC are listed in Table. XIII and Table. XIV.

The energy ratio from MC are fitted with a parabolic function to the observed values, named as the energy ratio correction curve  $f(R)$ . Fig. 60a and Fig. 60b show the energy ratio correction curves for the rotated energy of SS and MS events, respectively. The difference between the SS and MS energy ratio correction curve is shown in Fig. 60c. The difference between two correction curves is very small, within 0.02%. Similar correction curves can be obtained for ionization only energy, as shown in Fig. 61. It shows the ratio correction factor for MS events is higher than that for SS events.

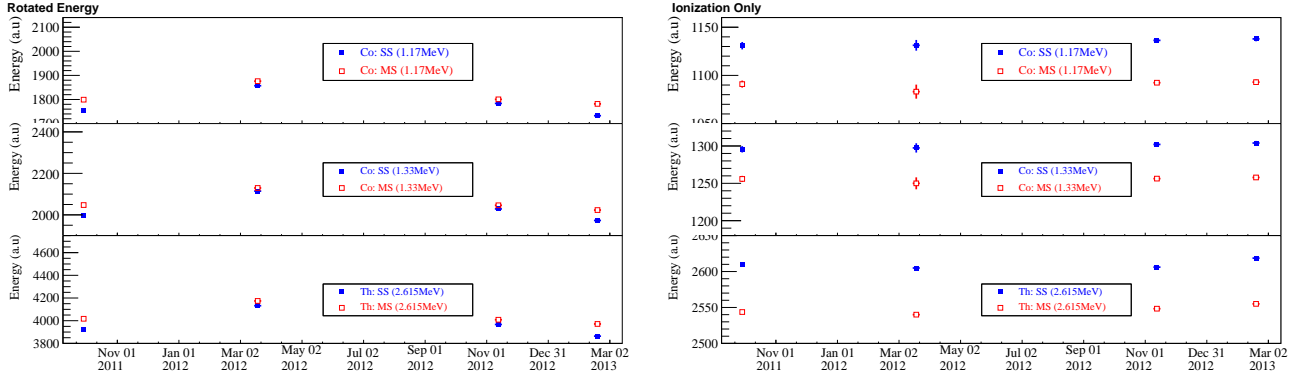


FIG. 56: Left (a): The rotated energy peaks (un-calibrated) for  $^{60}\text{Co}$ . Right (b): The ionization only energy peaks (un-calibrated) for  $^{60}\text{Co}$ . In both plots, the  $^{228}\text{Th}$  peaks in the same calibration weeks are at the bottom panel.

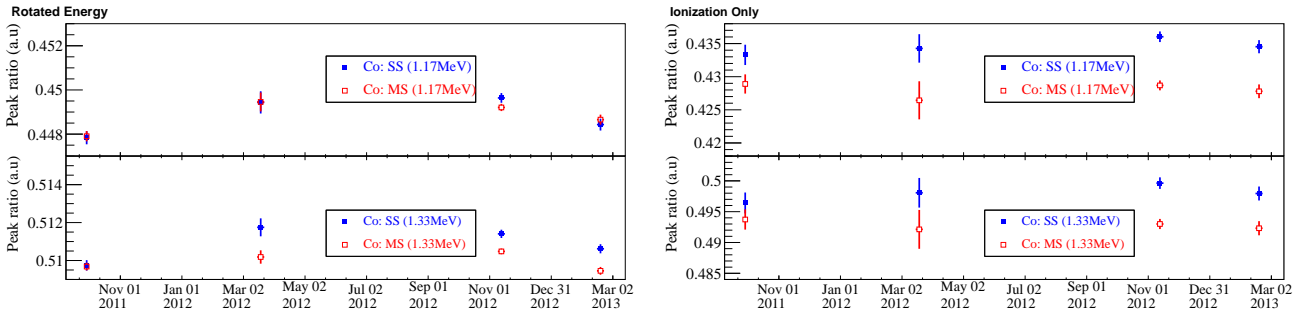


FIG. 57: Left (a): The ratios of rotated energy peaks of  $^{60}\text{Co}$  relative to the peaks of  $^{228}\text{Th}$ . Right (b): The ratios for ionization only energy peaks of  $^{60}\text{Co}$  relative to the peaks of  $^{228}\text{Th}$ .

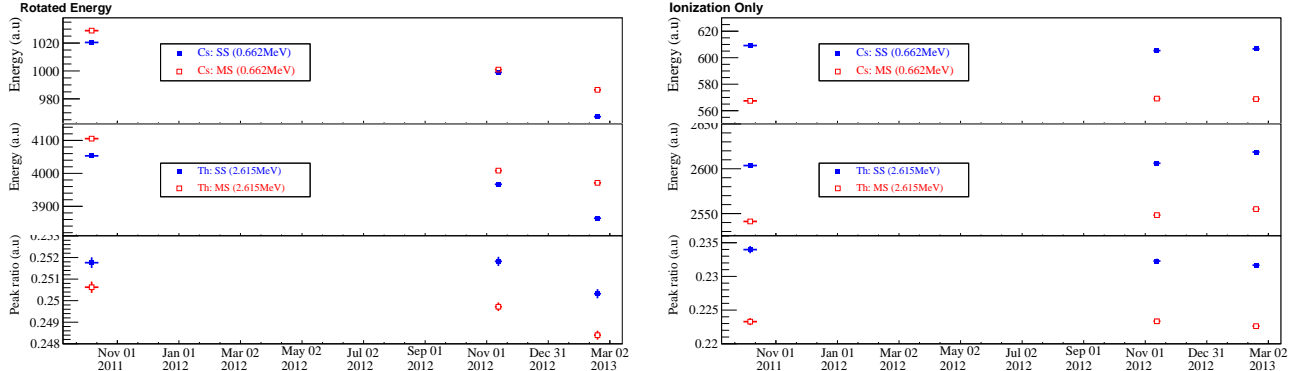


FIG. 58: Left (a): The rotated energy peaks of  $^{137}\text{Cs}$  and their ratios relative to the peaks of  $^{228}\text{Th}$ . Right (b): The ionization only energy peaks of  $^{137}\text{Cs}$  and their ratios relative to the peaks of  $^{228}\text{Th}$ .

Thus, the time variation correction is done in following steps:

- The optimal rotation angle is determined weekly by combining  $^{228}\text{Th}$  calibration runs in that week, referred as  $\theta_w^R$ . The corresponding peak position of  $E_R$  at 2615 keV  $\gamma$  line is referred as  $E_w^{Th}$ .
- For each event, use the corresponding weekly rotation angle to calculate the rotated energy (un-calibrated),  $E_{raw}$ . Then the energy ratio  $R$  is calculated as  $R = \frac{E_{raw}}{E_w^{Th}}$ .
- The corrected energy ratio is  $R_{corr} = f(R)$  and the calibrated energy is  $E = (E_{true}^{Th} - E_{bias}) \cdot f(R)$ .

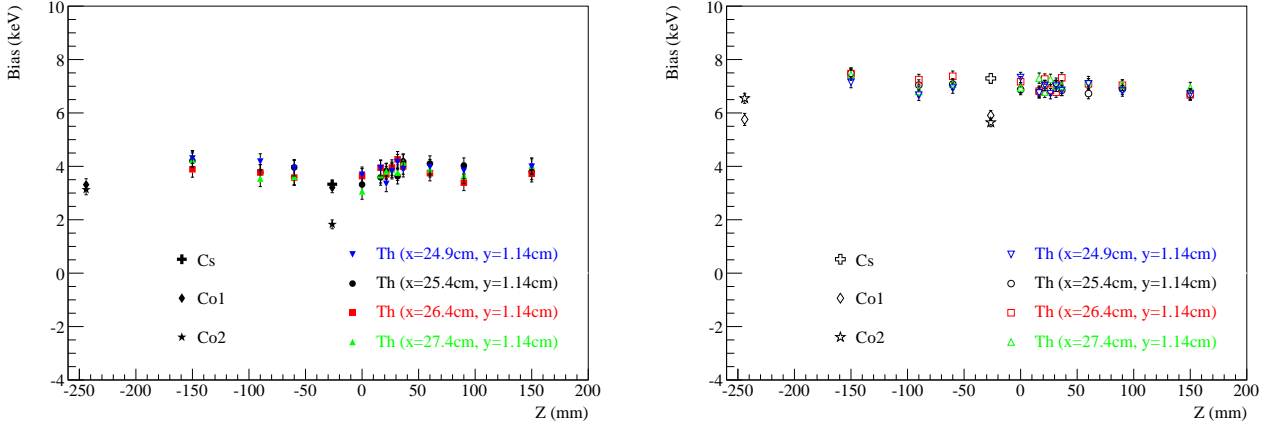


FIG. 59: The energy bias for different sources from a group of MC. The bias was introduced by fitting smeared MC energy spectrum by using a Gaussian plus complementary error function model, defined as  $(E_{true} - E_{fit})$ . Just as a check, a group of Th MC with different calibration tube positions and Z locations (in the tube) is used, and there is slight difference between different source locations.

TABLE XIII: The energy bias table. The bias was introduced by fitting smeared MC energy spectrum by using a Gaussian plus complementary error function model, defined as  $(E_{true} - E_{fit})$ .

	$^{137}\text{Cs}$ @662 keV	$^{60}\text{Co}$ @1173 keV	$^{60}\text{Co}$ @1333 keV	$^{228}\text{Th}$ @2615 keV
SS	3.19 keV	3.19 keV	2.50 keV	3.82 keV
MS	8.13 keV	6.19 keV	6.35 keV	7.15 keV

TABLE XIV: The **Rotated** and **Ionization only** energy ratio table. For both data and MC, the ratio is defined as fitted energy peaks of  $^{137}\text{Cs}$  or  $^{60}\text{Co}$  relative to that of  $^{228}\text{Th}$ . The error on data comes from the RMS value of all existing calibration campaign data.

<b>Rotated Energy</b> $\gamma$ peaks	SS		MS	
	data	Expectation	data	Expectation
$^{137}\text{Cs}$ @662 keV	$0.2513 \pm 6.9\text{-}4$	0.2523	$0.2496 \pm 9.1\text{-}4$	0.2507
$^{60}\text{Co}$ @1173 keV	$0.4488 \pm 7.4\text{-}4$	0.4480	$0.4488 \pm 6.0\text{-}4$	0.4474
$^{60}\text{Co}$ @1333 keV	$0.5109 \pm 7.7\text{-}4$	0.5095	$0.5100 \pm 4.0\text{-}4$	0.5087
<b>Ionization only</b> $\gamma$ peaks	SS		MS	
	data	Expectation	data	Expectation
$^{137}\text{Cs}$ @662 keV	$0.2326 \pm 9.7\text{-}4$	0.2523	$0.2231 \pm 9.1\text{-}4$	0.2507
$^{60}\text{Co}$ @1173 keV	$0.4345 \pm 9.8\text{-}4$	0.4480	$0.4280 \pm 9.7\text{-}3$	0.4474
$^{60}\text{Co}$ @1333 keV	$0.4980 \pm 1.1\text{-}3$	0.5095	$0.4928 \pm 6.3\text{-}4$	0.5087

#### D. Systematics

It is expected that the energy time variation and the small non-linearity can be corrected by using the calibration strategy discussed in section VI C. However, it needs additional data to check the systematics. In Oct 2011, for about one month we only deploy  $^{60}\text{Co}$  source as routine calibration instead of deploying  $^{228}\text{Th}$  source. So those  $^{60}\text{Co}$  runs can be used to check the energy calibration. Fig. 62a shows the calibrated energy peaks of  $^{60}\text{Co}$  source as a function of time, which looks quite stable. Fig. 62b shows the energy peaks distributions and the dashed lines in each subplots indicate the expected values. The mean value of each distribution agree with the expectation quite well.

In low background (L.B.) data, the  $^{40}\text{K}$  background events (emitted from the TPC detector materials) are also good to check the energy scale systematics. Since the  $^{40}\text{K}$  peak in L.B. SS events is much less obvious than that in MS events, so here we just use the L.B. MS spectrum to check the  $^{40}\text{K}$  energy peak. Fig. 63 is the MS energy spectrum of simulated  $^{40}\text{K}$  background events. The fitted peak position is  $1455.7 \pm 0.2$  keV using a (Gaus+Erfc) model, which indicates the fitting model introduces a 5.1 keV bias. For L.B. data, to increase the statistics we not only use the Run2A data set, but use all the golden L.B. runs from Run2464 to Run4875. As we know, in the L.B. data there are

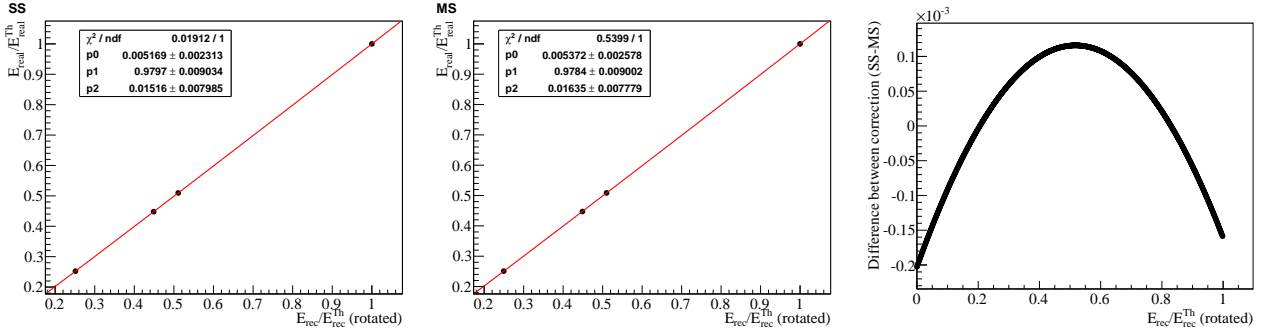


FIG. 60: Rotated energy ratio. Left (a): rotated energy ratio for SS events, data points are from  $^{137}\text{Cs}$ ,  $^{60}\text{Co}$  and  $^{228}\text{Th}$  sources. Middle (b): rotated energy ratio for MS events. The fitted curve is a second order polynomial function. Right (c): the difference between two correction curves, defined as (SS-MS).

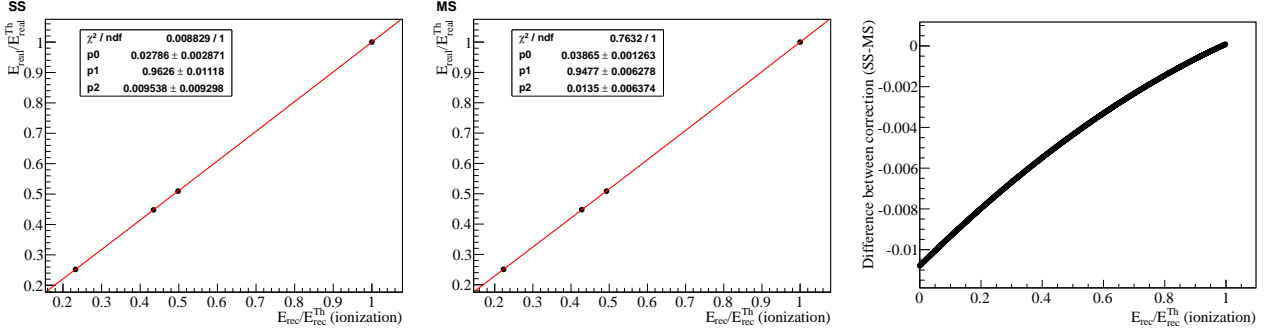


FIG. 61: Ionization energy ratio. Left (a): ionization only energy ratio for SS events, data points are from  $^{137}\text{Cs}$ ,  $^{60}\text{Co}$  and  $^{228}\text{Th}$  sources. Middle (b): ionization only energy ratio for MS events. The fitted curve is a second order polynomial function. Right (c): the difference between two correction curves, defined as (SS-MS).

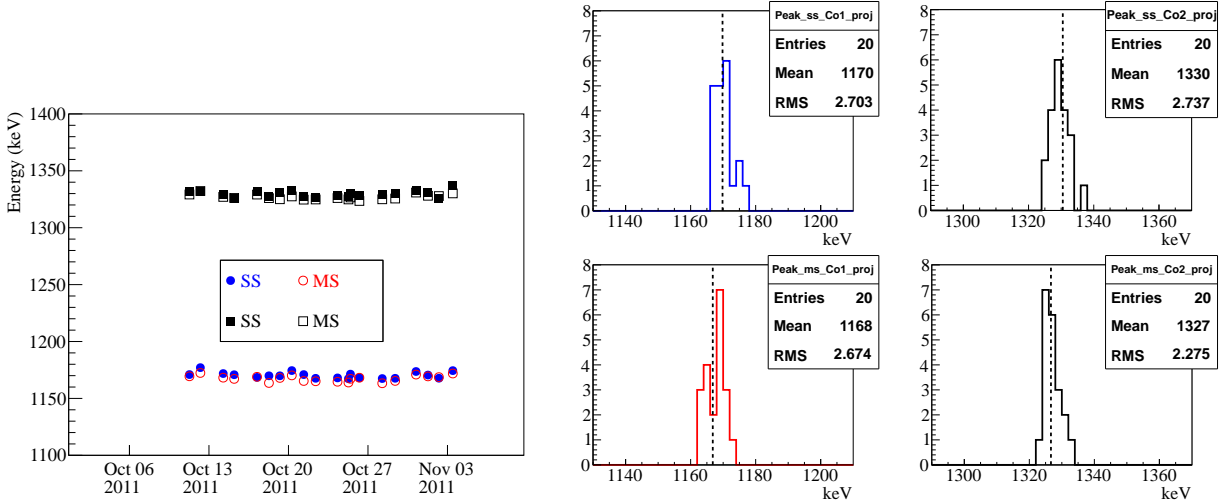


FIG. 62: Check  $^{60}\text{Co}$  peaks for the period in Oct, 2011 with no  $^{228}\text{Th}$  calibration data. Left (a): the fitted energy peaks (calibrated) as a function of time. Right (b): the energy peaks distributions. The dashed lines in each subplots indicate the expected values: 1169.8 keV (SS), 1330.5 keV (SS), 1166.8 keV (MS) and 1326.6 keV (MS).

multiple components can contribute the  $^{40}\text{K}$  energy peak region. For simplicity, we use two (Gaus+Erfc) models to describe  $^{40}\text{K}$  and the nearby  $^{60}\text{Co}$  peak, respectively, and use a exponential function to approximate the underlying  $2\nu\beta\beta$  spectrum. We also try different fitting ranges to check how it affects the fitted energy peak, as shown in Fig. 64. In the end, we quote the  $^{40}\text{K}$  energy peak from L.B MS spectrum as 1455.4 keV (the mean of the three fitted energy

peaks), and the uncertainty is 3.1 keV (the difference between the maximum and minimum fitted peaks).

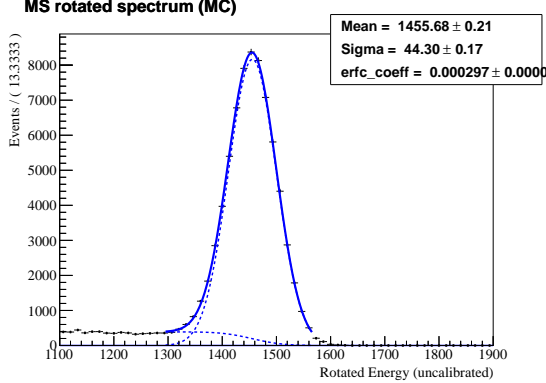


FIG. 63: The energy spectrum of simulated  $^{40}\text{K}$  background events from the TPC detector materials. This MC data is corresponding to the P.D.F called *AllVessel\_K40* for the final fitting. Again, a (Gaussian+Erfc) model is used to fit the smeared MC energy spectrum.

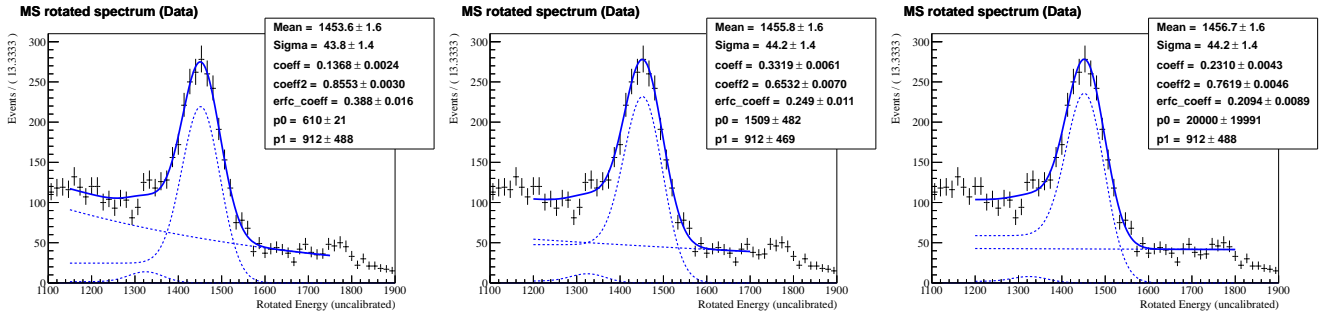


FIG. 64: The energy spectrum of MS events in L.B data, with golden runs from Run2464 to Run4875. For simplicity, we use two (Gaus+Erfc) models to describe  $^{40}\text{K}$  and the nearby  $^{60}\text{Co}$  peak, respectively, and use a exponential function to approximate the underlying  $2\nu\beta\beta$  spectrum. The sub-figures show the results with different fitting ranges, where the data points are exactly the same.

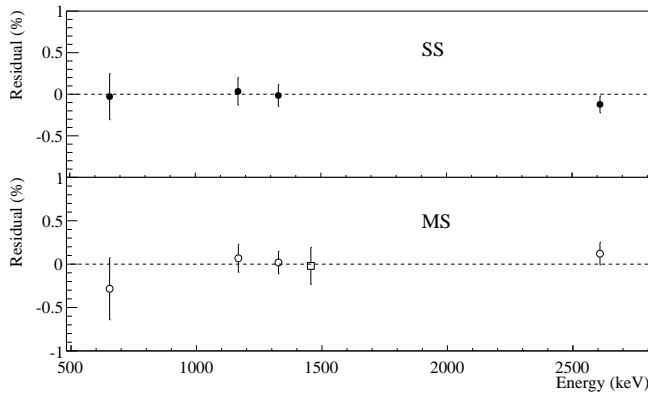


FIG. 65: The residuals, defined as  $(E_{\text{calib}} - E_{\text{exp}})/E_{\text{exp}}$ , for the calibrated energy peaks at the  $\gamma$  lines of three sources. For each point, the central value is the mean of all available calibration campaign data, the error bar is the RMS. The rectangular point in bottom panel is from the  $^{40}\text{K}$  peak in low background MS spectrum.

The residuals of the calibrated energy at the  $\gamma$  lines of three sources, defined as  $(E_{\text{calib}} - E_{\text{exp}})/E_{\text{exp}}$ , are shown in Fig. 65. For each data point, the central value is the mean of all available calibration campaign data, and the error bar is the RMS. The  $^{40}\text{K}$  point discussed above is also superimposed in Fig. 65.

### 1. Efficiency uncertainty caused by energy scale uncertainty

From Fig. 65, the energy scale uncertainty at 662 keV is  $\sim 0.4\%$  ( $\sim 2.5$  keV). The energy cut used for source agreement study and low background fit in this analysis is (700keV, 3500keV). If assuming the energy scale uncertainty at 700 keV cut is also  $\sim 0.4\%$ , using the smeared MC spectrum of sources ( $^{228}\text{Th}/^{60}\text{Co}$ ) and  $2\nu\beta\beta$  events, the relative uncertainty on efficiency can be calculated as  $N(697.5\text{keV} < E < 702.5\text{keV})/N(700\text{keV} < E < 3500\text{keV})/2$ . Such uncertainty is  $\sim 0.3\%$  for source data and  $\sim 0.4\%$  for  $2\nu\beta\beta$  events. The efficiency uncertainty caused by resolution variation is negligible,  $< 0.05\%$ .

## VII. ENERGY RESOLUTION (ITERATIVE APPROACH)

### A. Introduction

The current Monte Carlo (MC) simulation of EXO-200 does not account for the (anti-)correlation between the light captured from the scintillation process and the charge deposited and/or induced in U- and V-wires from the ionization process. This imposes limits to the prediction of the MC simulation for quantities that make use of such correlation. In particular, the resolution in the rotated energy estimated with MC simulation does not match that observed in data. As a result, another procedure is used to estimate the resolution in the rotated energy spectrum.

In the previous physics analysis, data from calibration campaigns was used to measure the resolution in four points of the rotated energy spectrum: at 667 keV, using a  $^{137}\text{Cs}$  source; at 1173 keV and 1332 keV, using a  $^{60}\text{Co}$  source; and at 2614 keV, using a  $^{228}\text{Th}$  source. For each of these sources, the data from different locations and dates were combined to increase the number of events used in the measurements. The resolution for each of the above energy position was obtained by fitting a Gaussian plus a complementary error function (Erfc) to the characteristic energy peak of each source. The resulting four points were used to fit the following resolution function:

$$\sigma^2(E) = p_0^2 E + p_1^2 + p_2^2 E^2, \quad (20)$$

where  $p_0$ ,  $p_1$  and  $p_2$  represent the statistical, noise and gain drift contributions, respectively.

The above procedure can be improved in a number of ways. First, the combination of data from different dates may hide effects caused by different conditions of the system. Thus, it is desired to estimate the resolution parameters as a function of time. Moreover, the Gaussian plus Erfc fit is observed to be biased by the range of the fit. It is especially complicated to apply it for the Co peak at 1173 keV, because of the background events under this peak that are related to the peak at 1332 keV and should not be described only by the Erfc. In addition, this type of fit can be additionally biased by the combination of data from different source locations. Finally, the risk imposed by frequent deployment of different types of source translates into seldom calibration campaigns. As a result, the data acquired in only a few weeks is used to describe the energy resolution of the data taken during all the time period of the physics runs.

In order to correct for some of the above effects, it is suggested to fit the MC energy spectrum (using the same smearing procedure) to that observed in calibration data which is taken on a regular time basis. The most frequent type of calibration data is  $^{228}\text{Th}$  at a location referred to as S5, where the source is near the cathode. (Hereafter, this particular source and location setup will be referred to as *Th@S5*.) This method replaces the Gaussian plus Erfc model by a more realistic MC model of the source, that includes the detector geometry and simulation of the interactions in the detector.

The resolution of detectors are commonly described by Gaussian distributions. In these cases, the energy distribution is described by the convolution of the MC probability density function (pdf) and the Gaussian distribution that models the resolution. Attempts to calculate the resolution parameters of EXO-200 using Th@S5 data to fit this model with standard fit procedures, such as RooFit and MIGRAD, failed to converge when no constraints were imposed. At the time when these attempts were made, additional problems of the model had not been addressed yet and may now have been fixed. However, in this fit procedure, the MC pdf have to be binned before the convolution.

### B. The Iterative Approach

Motivated by the complications to calculate the resolution parameters of EXO-200 discussed in section VII A, Igor Ostrovskiy proposed [1] a statistical procedure, initially developed by Ryan Patterson [2], to estimate these parameters using Th@S5 data and its MC pdf. This procedure is usually referred to as *the iterative approach*. During the course of this work, I ran into some problems related to our implementation of the method, but in particular, I corrected a fundamental problem with the method itself[? ]. This section provides a description of the method including my personal corrections, as well as consistency checks of the current implementation.

#### 1. Description of the Method

A common problem in MC models of detectors is the estimation of the covariance matrix of its parameters. Laboratory tests can be used to estimate the parameters, but they often do not account for the correlation between them. To overcome this problem, R. Patterson [2] proposed a statistical procedure that accounts for all laboratory tests (or the best knowledge of the parameters included in the model) to estimate their correlations and tune their values to

the actual MC model of the detector using data acquired with the final detector setup. In the case of parameters for which no measurements are available, enormous errors are given.

The underlying assumption of the method is that all the parameters compose a multivariate Gaussian distribution. The initial mean of this distribution ( $\bar{\mathbf{s}}_0$ ) is considered to be the best known values of the parameters in the model,  $\bar{\mathbf{s}}_0 = (s_{0,0}, \dots, s_{0,N})$ , where  $N$  is the number of parameters. The initial covariance matrix ( $\Sigma_0$ ) has the diagonal set to the square of the best known errors of the parameters, while the off-diagonal is set to zero (no initial correlations). Using this distribution,  $\bar{\mathbf{s}}_0$  and  $\Sigma_0$ , many parameter sets  $\{s_0^{(1)}, \dots, s_0^{(M)}\}$  are drawn, with  $M \sim 1000$ . Then, the available data from the detector is compared to the predictions of the model using each parameter set  $s_0^{(m)}$  with a  $\chi^2$  test, which results in  $\chi_{0,m}^2$ . A comparison between the likelihood of drawing the parameter set and that of having it to describe the data is used to assign a weight for each parameter set.

The likelihood of drawing the parameter set  $s_0^{(m)}$ , relative to the others, is given by:

$$d_{0,m} = \exp\left(-\frac{1}{2}W_{0,m}\right) = \exp\left(-\frac{1}{2}(s_0^{(m)} - \bar{s}_0)^T \Sigma_0^{-1} (s_0^{(m)} - \bar{s}_0)\right), \quad (21)$$

where  $W_{0,m}$  is the square of the Mahalanobis distance between  $s_0^{(m)}$  and  $\bar{s}_0$ ; and  $\Sigma_0^{-1}$  is the inverse of the covariance matrix. On the other hand, the smallest value that the above  $\chi^2$  test can achieve ( $\chi_{min}^2$ ) follows a chi-square distribution with  $D - N$  degrees of freedom, where  $D$  is the number of data points. In addition, the quantity  $\Delta\chi^2 \equiv \chi^2 - \chi_{min}^2$  is distributed as a chi-square distribution with  $N$  degrees of freedom. Therefore, the likelihood of having the parameter set  $s_0^{(m)}$  to describe the data, relative to the others, is given by:

$$p_{0,m} = \exp\left(-\frac{1}{2}\Delta\chi_{0,m}^2\right). \quad (22)$$

If the data points provide an additional constraint to the initial set of parameters, ie.  $p_{0,m} < d_{0,m}$  or  $W_{0,m} > \Delta\chi_{0,m}^2$ , then it is possible to reduce the error in the parameters by adjusting the relative likelihood of the parameter set  $s_0^{(m)}$  from  $d_{0,m}$  to  $p_{0,m}$ . Hence, each parameter set is assigned an additional weight of:

$$\eta_{0,m} = \min\left(1, \frac{p_{0,m}}{d_{0,m}}\right). \quad (23)$$

Using these weights, a new multivariate Gaussian distribution is constructed from the  $M$  drawn parameter sets with mean:

$$\bar{\mathbf{s}}_1 = \frac{\sum_m \eta_{0,m} \mathbf{s}_0^{(m)}}{\sum_m \eta_{0,m}}, \quad (24)$$

and covariance matrix:

$$\Sigma_{1,ij} = \frac{\sum_m \eta_{0,m} (s_{0,i}^{(m)} - s_{1,i})(s_{0,j}^{(m)} - s_{1,j})}{\frac{M-1}{M} \sum_m \eta_{0,m}}. \quad (25)$$

This procedure can be repeated as many time as wanted to improve the estimation of the parameters and their covariance matrix.

This method is primarily constructed to estimate the covariance matrix of parameters in a MC model. This is obtained by down-weighting samples that are less likely to describe the measured data. As a consequence, it further reduces uncertainties while finding parameters that minimize the  $\chi^2$  variable. For parameters with errors that are further constrained, the final error is estimated by  $\Delta\chi^2 < \text{UP}$ , where UP is a value that depends on the number of parameters [3]. For instance,  $N = 1$  and  $\text{UP} = 1$  implies a coverage of 68.3% of the draws in the limit of many iterations. This follows as a consequence of equation 23.

## 2. Implementation of the Method

The above method is currently implemented to calculate the resolution parameters of EXO-200. This sections details specific settings used in such calculation.

Equation 20 is used to smear the energy from MC simulation by the following procedure. The true energy ( $E_{true}^{(evt)}$ ) from each event in the MC dataset is used to fill a binned energy distribution histogram. This histogram support

bins of arbitrary widths. The contribution of a MC event with energy  $E_{true}^{(evt)}$  to a bin  $b$  of the energy distribution delimited by the low and high energy edges  $E_{low}^b$  and  $E_{high}^b$ , respectively, is given by:

$$C_{E_{low}^b, E_{high}^b}^{(evt)} = \frac{1}{2} \left( \operatorname{erf} \left( \frac{E_{high}^b - E_{true}^{(evt)}}{\sigma(E_{true}^{(evt)})} \right) - \operatorname{erf} \left( \frac{E_{low}^b - E_{true}^{(evt)}}{\sigma(E_{true}^{(evt)})} \right) \right), \quad (26)$$

where  $\operatorname{erf}(x)$  is the error function (the cumulative function of the Gaussian distribution); and  $\sigma(x)$  is the square root of equation 20. As a result, each bin  $b$  of the smeared energy distribution is filled with a content given by:

$$C_b = \sum_{evt \in \text{MC}} C_{E_{low}^b, E_{high}^b}^{(evt)}. \quad (27)$$

The current calculations are performed for an energy distribution between 700 keV and 3500 keV, with bin widths of 20 keV.

The calculations for SS and MS events are performed independently. In each case, the 3 resolution parameters,  $p_0$ ,  $p_1$  and  $p_2$ , compose the parameter space. Their initial values are set those numbers obtained in the closest (in time) calibration campaign (figure 72). The errors are increased by taking the maximum value between the error assigned by the calibration campaigns and 100%. A total of 1000 parameter sets are drawn in every iteration.

In the calculation of the  $\chi^2$ , the bins are combined until there are at least 36 events in data and MC distributions. (This is to assure the validity of the approximation of a Poisson by a Gaussian distribution.) Then, it is calculated by:

$$\chi^2 = \sum_{b=1}^{N_b} \frac{\left( \frac{o_b}{O_T} - \frac{e_b}{E_T} \right)^2}{\frac{o_b}{O_T^2} + \frac{e_b}{E_T^2}}, \quad (28)$$

where  $N_b$  is the number of bins;  $o_b$  is the number of observed events in the data bin  $b$ ;  $e_b$  is the number of expected events in the bin  $b$  of the smeared MC energy distribution; and  $O_T$  and  $E_T$  are the total number of events in data and smeared MC energy distributions, respectively.

The  $\chi^2_{min}$  is unknown. In the current implementation, each iteration  $i$  uses the following choice for this number:

$$\chi_{i,min}^2 = \min_{m \leq M} \chi_{i,m}^2. \quad (29)$$

With this choice, at least one of the parameter sets drawn in the iteration  $i$  is weighted to unit ( $\eta = 1$ ). Moreover, in order to compensate parameter sets with different number of degrees of freedom, the following expression is used:

$$\Delta\chi_{i,m}^2 = (\chi_{i,m}^2 - NDF_{i,m}) - (\chi_{i,min}^2 - NDF_{i,min}), \quad (30)$$

where  $NDF_{i,m}$  is the number of degrees of freedom observed in the  $\chi^2$  calculation of the parameter set  $s_i^{(m)}$ , while  $NDF_{i,min}$  is the analog quantity for the parameter set yielding  $\chi_{i,min}^2$ .

The following additional requirement is imposed to each iteration  $i$ :

$$\sum_{m=1}^M \eta_{i,m} > 300. \quad (31)$$

This is necessary to sample enough points of the pdf of the resulting multivariate Gaussian distribution[? ]. In the current implementation, if this condition is not satisfied,  $\chi_{i,min}^2$  is replaced by the next value in the set  $\{\chi_{i,m}^2\}$  sorted by increasing value. The latter operation is repeated until equation 31 is satisfied.

### 3. Results Using Th@S5 Data

Only Th@S5 data and its MC simulation is used in the current calculation of the resolution parameters. The data is grouped on a weekly basis using the exactly same time periods at which EXO-200 data is calibrated. There is a significant difference between the energy spectrum shape of data acquired with different trigger settings[? ]. For this reason, data acquired with different trigger settings are not mixed. Table XV shows the runs grouped by week and trigger settings.

Week	Start	End	Runs	Trigger
4	2011-09-28 16:00:00	2011-10-01 01:13:00	2418, 2423	random 50 Hz
5	2011-10-01 1:13:00	2011-10-14 11:00:00	2426, 2434, 2447	random 50 Hz
11	2011-11-18 11:00:00	2011-11-25 11:00:00	2817	prescale 1
12	2011-11-25 11:00:00	2011-12-02 11:00:00	2837, 2848	prescale 1
13	2011-12-02 11:00:00	2011-12-09 11:00:00	2883, 2885, 2886, 2904	prescale 1
14	2011-12-09 11:00:00	2011-12-16 11:00:00	2927, 2938, 2947	prescale 1
15	2011-12-16 11:00:00	2011-12-23 11:00:00	2966, 2981, 2991	prescale 1
16	2011-12-23 11:00:00	2011-12-30 11:00:00	3007, 3024, 3028	prescale 1
17	2011-12-30 11:00:00	2012-01-06 11:00:00	3034, 3053, 3074	prescale 1
18	2012-01-06 11:00:00	2012-01-13 11:00:00	3099, 3109	prescale 1
20	2012-01-20 11:00:00	2012-01-27 11:00:00	3137, 3142, 3147, 3152, 3158	prescale 1
21	2012-01-27 11:00:00	2012-02-03 11:00:00	3169, 3173, 3178, 3184, 3195, 3199	prescale 1
22	2012-02-03 11:00:00	2012-02-10 11:00:00	3204, 3214, 3218, 3223, 3227, 3231, 3236	prescale 1
23	2012-02-10 11:00:00	2012-02-17 11:00:00	3246, 3250, 3254, 3258, 3262, 3266, 3270	prescale 1
24	2012-02-17 11:00:00	2012-02-24 11:00:00	3281, 3283, 3295, 3298	prescale 1
25	2012-02-24 11:00:00	2012-03-02 11:00:00	3342, 3345, 3347, 3351, 3352, 3355, 3358, 3361	prescale 1
26	2012-03-02 11:00:00	2012-03-09 11:00:00	3364, 3367, 3376, 3379, 3382, 3383, 3386, 3389	prescale 1
27	2012-03-09 11:00:00	2012-03-16 11:00:00	3392, 3395, 3404, 3407, 3410, 3413	prescale 1
28	2012-03-16 11:00:00	2012-03-23 11:00:00	3436, 3440, 3451, 3456, 3459	prescale 1
29	2012-03-23 11:00:00	2012-03-30 11:00:00	3463, 3468, 3471, 3476, 3488, 3492	prescale 1
30	2012-03-30 11:00:00	2012-04-06 11:00:00	3497, 3500, 3503, 3507, 3511, 3516, 3520	prescale 1
31	2012-04-06 11:00:00	2012-04-13 11:00:00	3531, 3534, 3537, 3542, 3547, 3550	prescale 1
32	2012-04-06 11:00:00	2012-04-20 11:00:00	3562, 3566, 3570, 3576, 3580	prescale 1

TABLE XV: Th@S5 runs used in the calculation of the weekly resolution parameters.

Figure 66 shows a comparison between the energy distributions in data and MC simulation for the initial values of the resolution parameters, while figure 67 shows the same comparison after 20 iterations of the method. The values of the reduced chi-square ( $\chi^2_{red} = \chi^2/NDF$ ) as a function of the iteration is depicted in figure 68 for 4 sample weeks. After a few iterations, the  $\chi^2_{red}$  slowly converges to a minimum. The relative error estimated at the characteristic energy peak observed in Th@S5 data (at 2614 keV) is plotted as a function of the iteration number in figure 69. They illustrate the increasing reduction of the errors assigned to the resolution parameters.

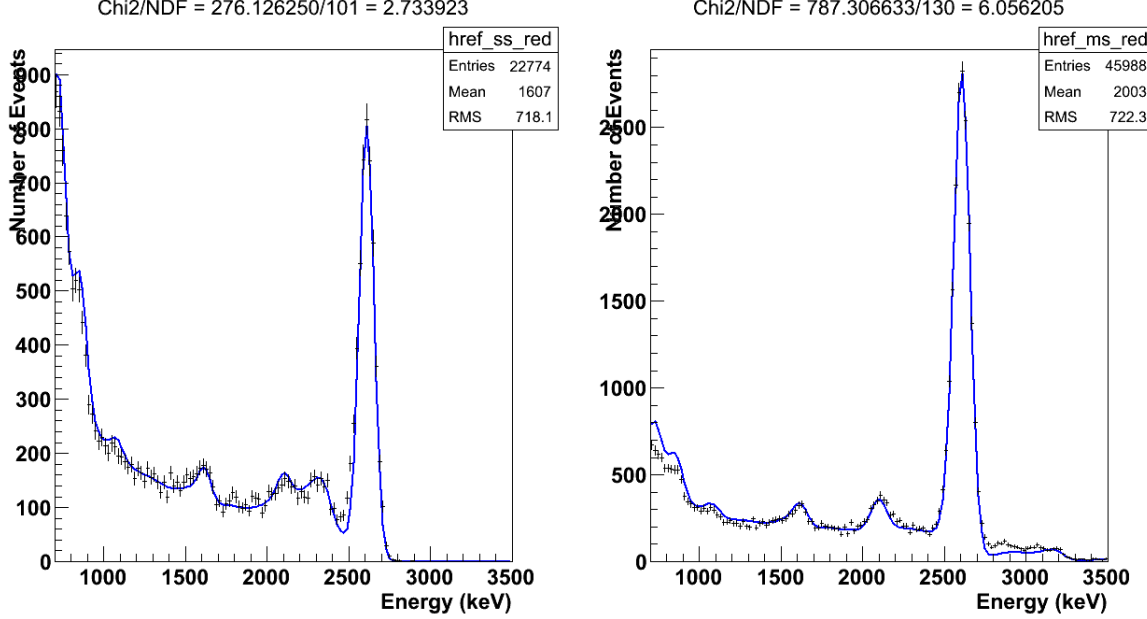


FIG. 66: Sample comparison between energy distributions in data and MC simulation for SS (left) and MS (right) events. This comparison is performed using data from week 4, at iteration 0 (resolution parameters from previous analysis).

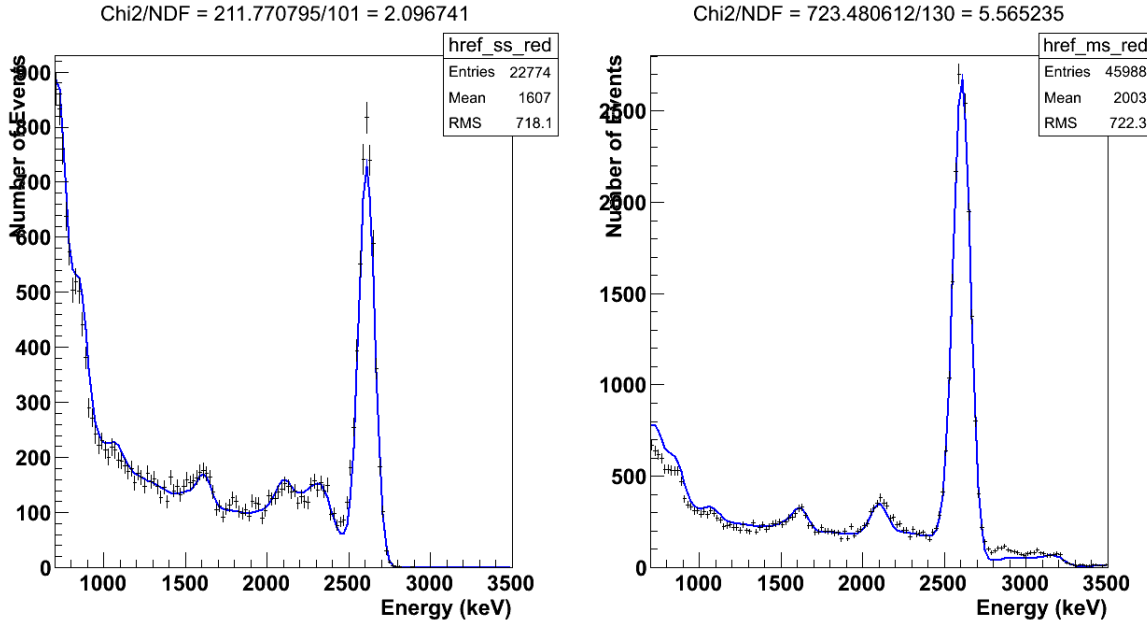


FIG. 67: Sample comparison between energy distributions in data and MC simulation for SS (left) and MS (right) events. This comparison is performed using data from week 4, after 20 iterations. Both SS and MS  $\chi^2$  are significantly reduced.

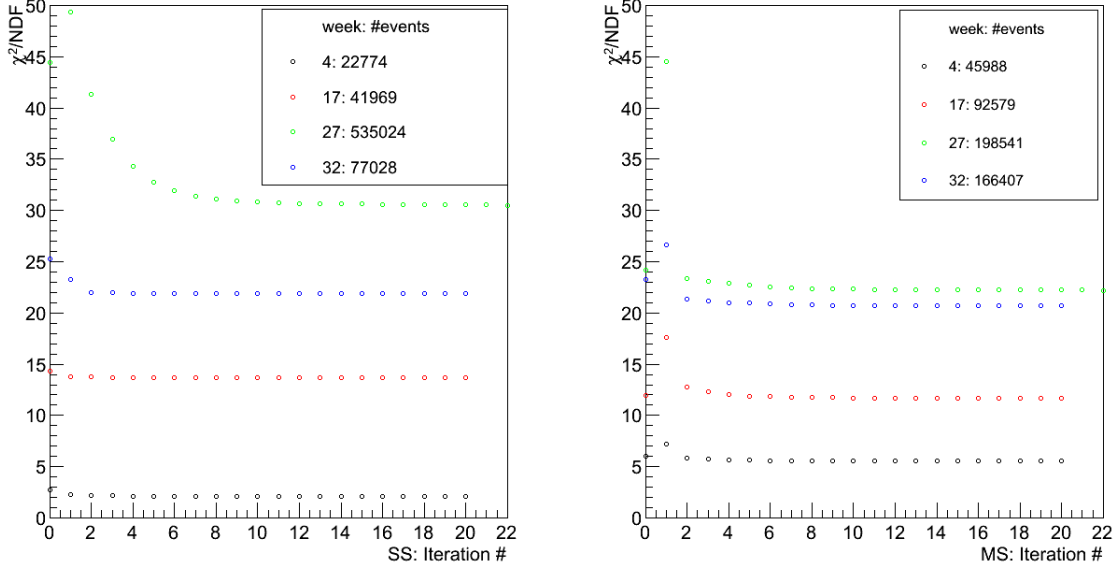


FIG. 68: Evolution of the reduced  $\chi^2$  as a function of the iteration number for 4 sample weeks.

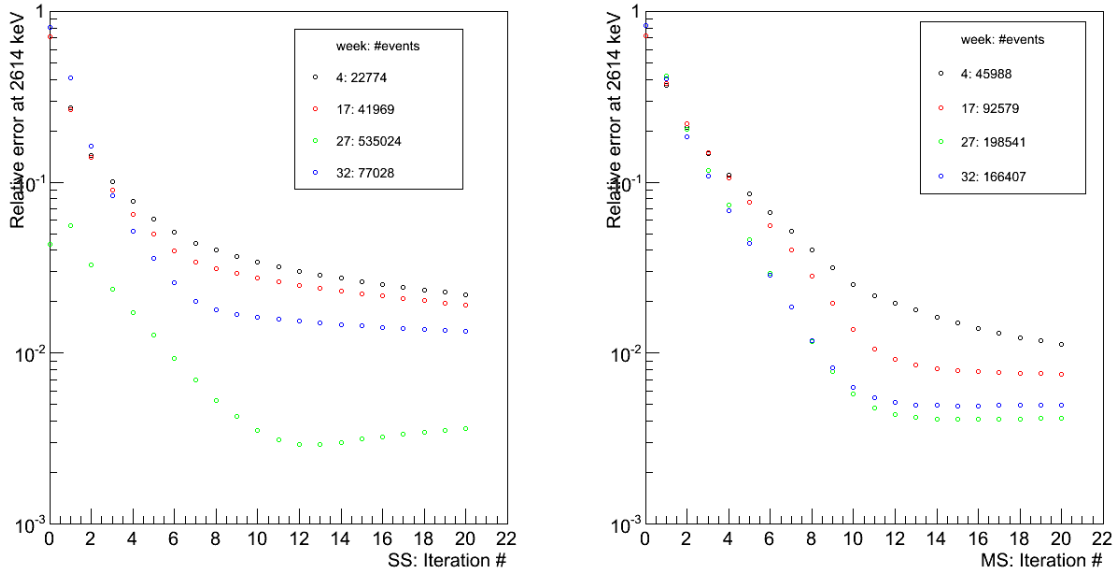


FIG. 69: Evolution of the relative resolution error at the energy 2614 keV as a function of the iteration number.

It is possible to compare the resolution at 2614 keV calculated from this method against that from a Gaussian plus Erfc fit on a weekly basis. Weekly calibration data using  $^{228}\text{Th}$  at various positions were used to calculate its characteristic peak position and corresponding resolution for calibration purposes. Figure 70 shows a comparison of the resolutions obtained for an energy of 2614 keV using both methods as a function of the week. In SS events, the trend of the resolution is similar for both methods. However, there is a small systematic difference between them. This difference has not been studied yet, but could be related to either the bias in the Gaussian plus Erfc fits or to the resolution model (equation 20). The situation in MS events is different, where both methods agree within errors. The error sizes are also similar between the two methods, which is in principle expected, since both arise only from statistical nature.

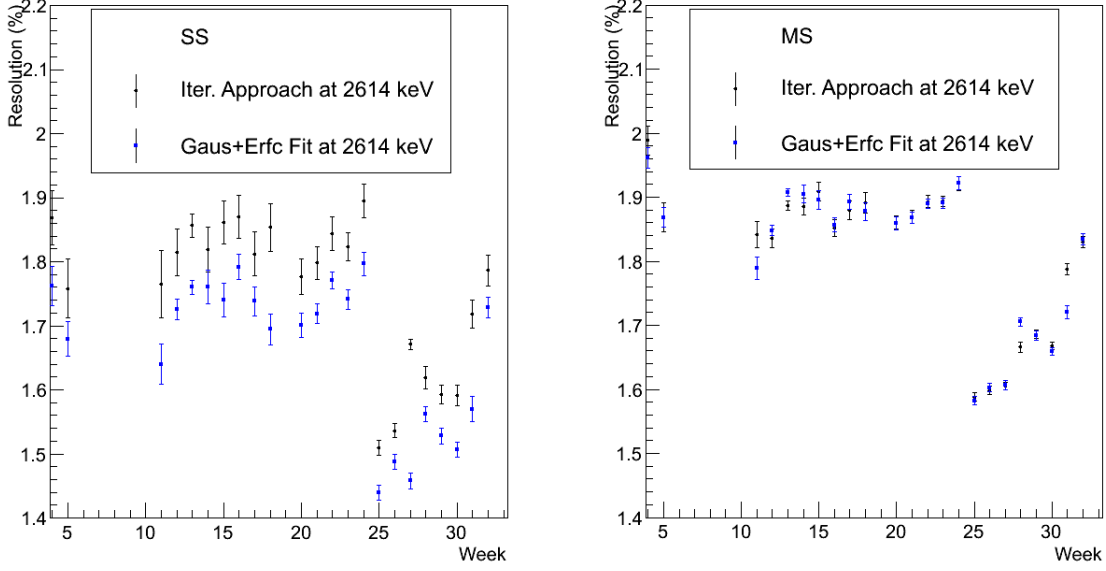


FIG. 70: Comparison of the calculated resolution at 2614 keV using the iterative approach and the Gaussian plus Erfc fit for the weeks in consideration.

#### 4. $^{60}\text{Co}$ Cross-check

A natural question that rises from figures 66 and 67 is whether the low energy peaks in these energy distributions actually help to constrain the values of the resolution parameters or they are entirely dependent on only the characteristic peak at 2614 keV. One can observe that, from the same figures, the reduced  $\chi^2$  decreases even though the characteristic peak seems to be worsen fitted by the MC simulation. This indicates that, indeed, the other peaks play some role in the MC fit. However, to further show the role of the other peaks, the energy distribution of Co@S5 in data is compared to its MC simulation before and after the fit of the Th@S5 MC simulation to its corresponding data at the same week in which the Co@S5 measurements were performed. Figure 71 shows this comparison for SS events. There is a significant improvement in the description of the Co peaks observed at 1173 and 1332 keV.

### C. Resolution Parameters for $2\nu\beta\beta$ Analysis

This section presents the results of the resolution parameters on a weekly basis. A comprehensive study of the statistical errors associated to the weekly parameters is performed to exclude suspicious results. The calculation of the average resolution parameters is described next, followed by a discussion of the errors associated to these parameters.

#### 1. Weekly Resolution

Between September, 2011, and April, 2012, two calibration campaigns took place in dates that correspond to weeks 4 and 28. Using these two campaigns, the resolution model (equation 20) was fit to data as presented in figure 72. Figure 73 shows the comparison between the resolution calculated at four energy values (667, 1173, 1332 and 2614 keV) using the parameters from campaign fits (figure 72) and from the weekly calculation (section VII B 3).

As observed in figure 73, the resolution depends on the method. The results from the iterative approach present slightly higher values for the resolution. In week 25, it detects an improved resolution in both SS and MS events, that is believed to be caused by a replacement of an APD board. This improvement in resolution is later observed in the calibration campaign of week 28. In SS events of week 27 (hereafter referred to as *week27-SS*), the results from the iterative approach seems offset with respect to the other values. This week is revisited below.

In order to validate the errors estimated from the iterative approach, the  $\chi^2$  profile is studied as a function of one and two parameters (1D and 2D, respectively). The main object of this study is to exclude suspicious results where errors are verified to be clearly mis-calculated, while keeping a simple and fast procedure. Hence, the non-varying

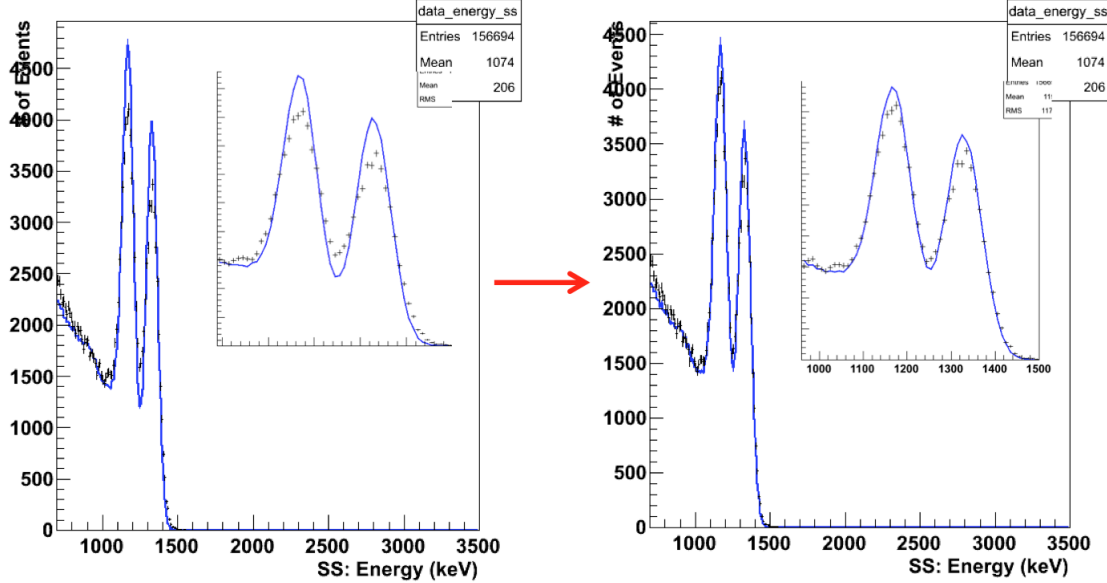


FIG. 71: Comparison of the Co@S5 energy distribution in SS events before and after the iterative approach is applied to Th@S5 data.

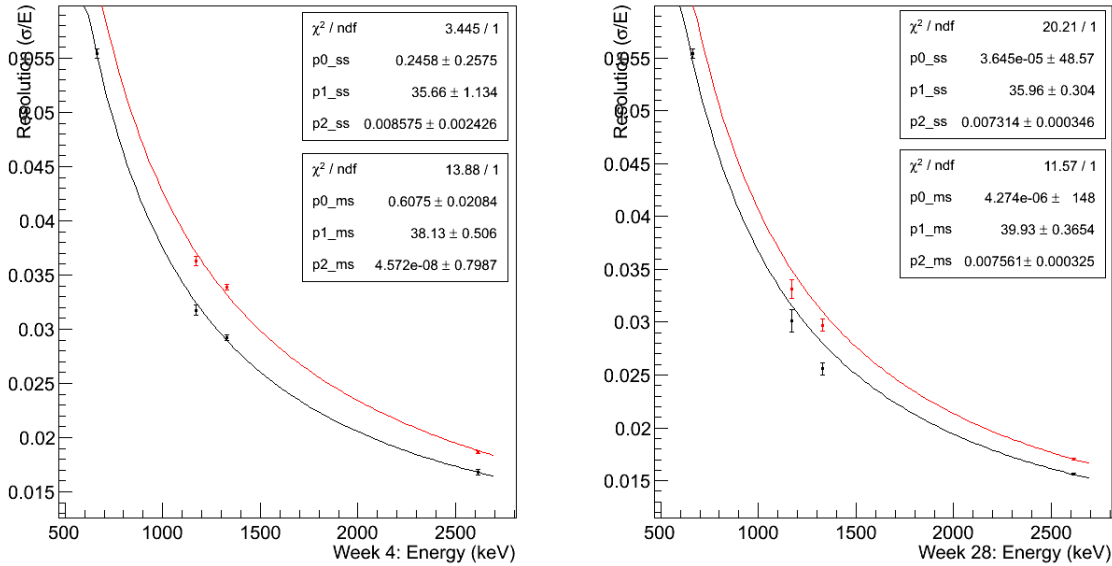


FIG. 72: Measurements of the characteristic energy peak of the four calibration sources in two calibration campaigns. Black and red colours correspond to SS and MS events, respectively. A fit of equation 20 is performed using these data points.

parameters in these  $\chi^2$  profiles are fixed at the same position, the position that minimizes the  $\chi^2$  as estimated by the iterative approach after 20 iterations. The underlying assumption of this study is that, for all the weeks, the  $\chi^2$  near the minimum is well approximated by an ellipsoid.

The 1D profiles are performed between -1 and +1 error around the varying parameter. They are expected to be described by a polynomial of second degree (parabola). An example of 1D profile, along with a parabola fit, is depicted in figure 74. In this example, the parabolas seem to fit fairly well the  $\chi^2$  profile. The  $\chi^2$  of the parabola fit ( $\chi^2_{\text{par}}$ ) is calculated using unit weights for all points. The probability of the observation of  $\chi^2_{\text{par}}$  is calculated using its number of degrees of freedom for all the fits. The only probability different than unit is observed in the  $\chi^2$  profile of week13-SS. Figure 75 shows the results of 1D profiles in week13-SS, which explains the results from the probability calculation. Therefore, week13-SS is rejected by this study and replaced by week12-SS.

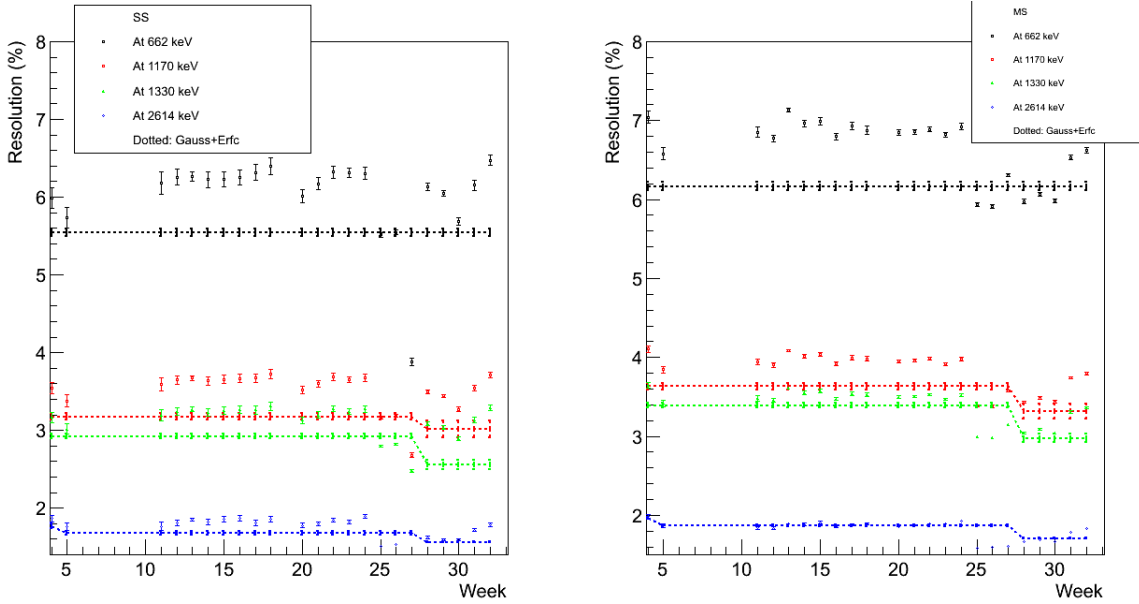


FIG. 73: Comparison of the calculated resolution at four energy values as a function of week between results from the iterative approach and those from the Gaussian plus Erfc fits.

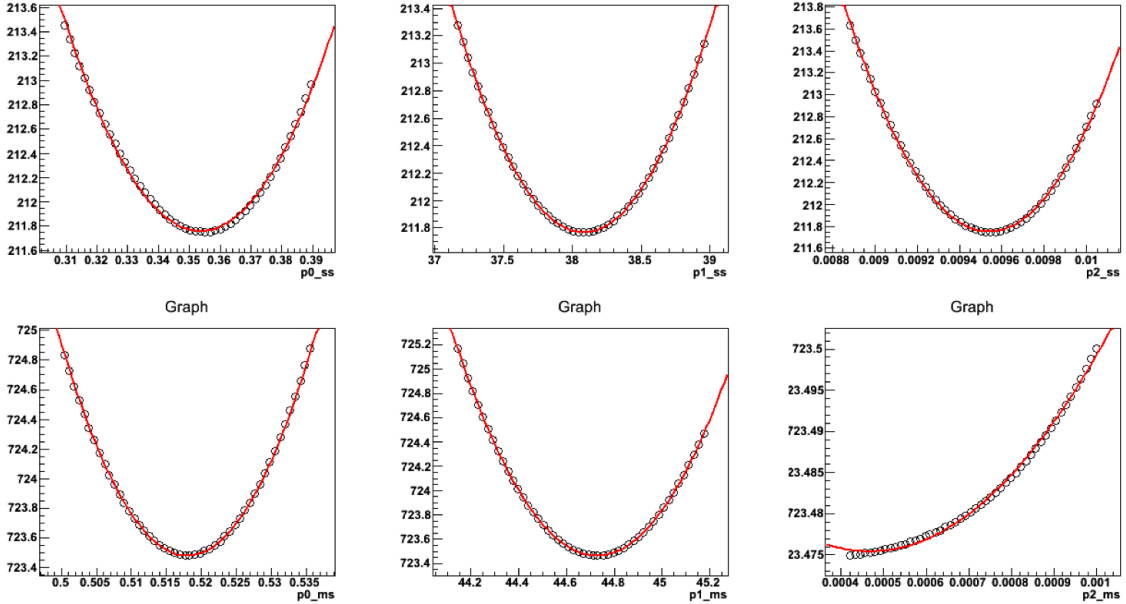
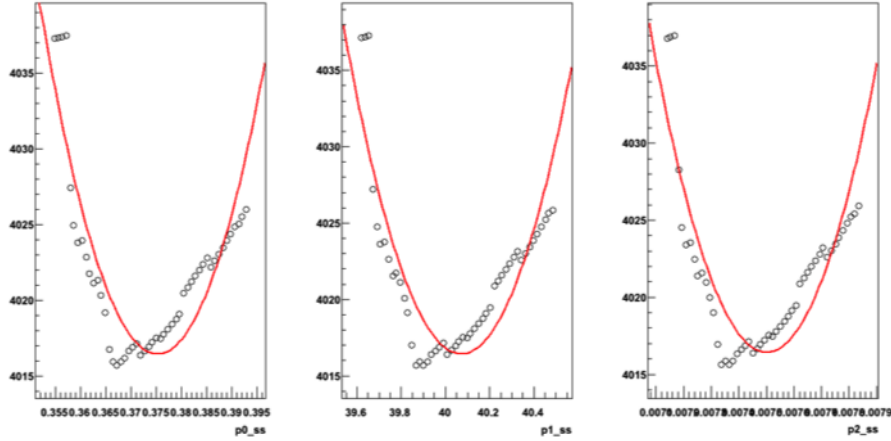
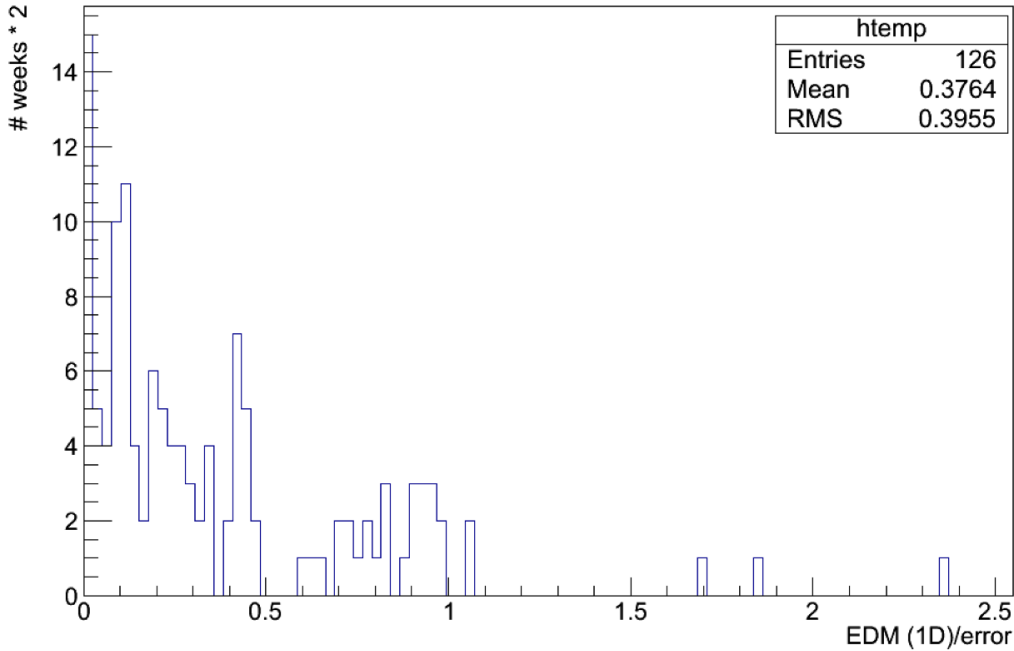


FIG. 74: Parabola fits to 1D profile of the  $\chi^2$ . The sample week is 4.

A better minimum of each parameter can be estimated from the 1D profile using the parabola parameters. For a parabola given by  $p(x) = a_2x^2 + a_1x + a_0$ , its minimum is located at  $x_{min} = -a_1/2a_2$ . The difference between the weekly parameters ( $p_i$ , for  $i = 0, 1$  or  $2$ ) and their corresponding  $x_{min}$  can be calculated in units of their error:  $edm_i = |p_i - x_{min}|/\delta p_i$ . This distance (edm-1D) is shown in figure 76. Only week27-SS presents this difference larger than 3. It is calculated to be 61, which indicates the termination of the iterative approach without convergence. This explains the mis-behaviour observed in figure 73. Hence, the resolution parameters for week27-SS are replaced by those from week26-SS.

FIG. 75: 1D profile of the  $\chi^2$  for results in week13-SS.FIG. 76: Difference, in units of the parameter error, between the minimum from the parabola fit to the 1D profile of the  $\chi^2$  and the parameter estimated using the iterative approach. Week13-SS and week27-SS are omitted.

The 2D profiles are performed between -2 and +2 errors around the values from the iterative approach for varying parameters. In this case, the contours of parameters yielding the same  $\chi^2$  are expected to be ellipses. The orientation of the ellipse gives the orientation of the correlation between the parameters. Figure 77 shows an example of the 2D profiles. In order to improve the visualization and allow the calculation of the correlation between parameters, each point is assigned a weight given by a pdf calculated by:  $P_2(A, B) = N_P \exp(-\chi^2(A, B))$ , where  $N_P$  is the normalization factor for this pdf. Figure 78 depicts  $P_2(A, B)$  corresponding to figure 77. The correlation between two parameters is obtained using:  $\text{cor}(A, B) = (\bar{AB} - \bar{A}\bar{B}) / (\sigma_A \sigma_B)$ , where the means and standard deviations are calculated using  $P_2$  marginalized over the other parameter as the pdf. The correlation using this formula is compared to that obtained from the iterative approach in figure 79. Only week5-MS presents a correlation of opposite sign. All the other correlations are negatives as expected. The resolution parameters from week4-MS are then considered for week5-MS.

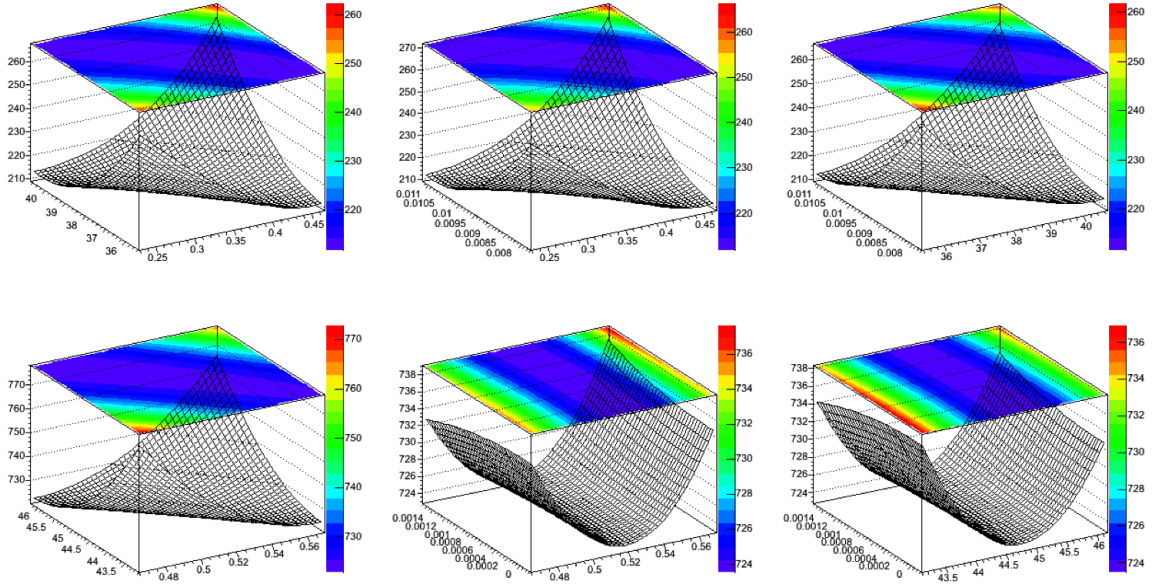


FIG. 77: Sample week (4) of 2D profiles of the  $\chi^2$ . Top are SS parameters, while bottom presents MS parameters. From left to right, the parameters from  $p_0$  to  $p_2$  are depicted in increasing order.

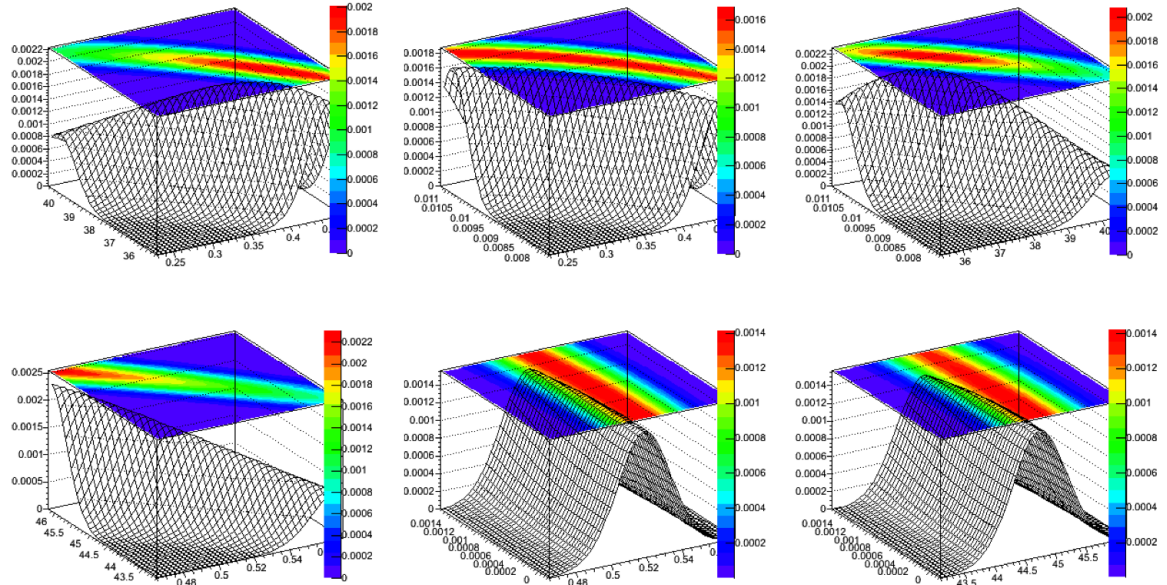


FIG. 78: Sample week (4) of 2D  $\chi^2$  likelihood ( $P_2(\chi^2(x,y))$ ). Green contours correspond to a confidence level of 68% ( $P(\chi^2) \rightarrow P(\chi^2)/2$ ). Top are SS parameters, while bottom presents MS parameters. From left to right, the parameters from  $p_0$  to  $p_2$  are depicted in increasing order.

In conclusion, the study of the 1D and 2D profiles flagged 3 suspicious calculations (7% of all calculations). Each of these issues is caused by a different problem: strange behaviour of the chi-square; non-convergence of the iterative approach; and wrong orientation of the correlation. Rather than fixing these issues, for simplicity, the parameters used in these weeks are taken from the corresponding previous week. The resolution parameters for weeks without Th@S5 measurements are assigned to those values of the corresponding nearest week. The weekly values of the resolution parameters are depicted in figure 80.

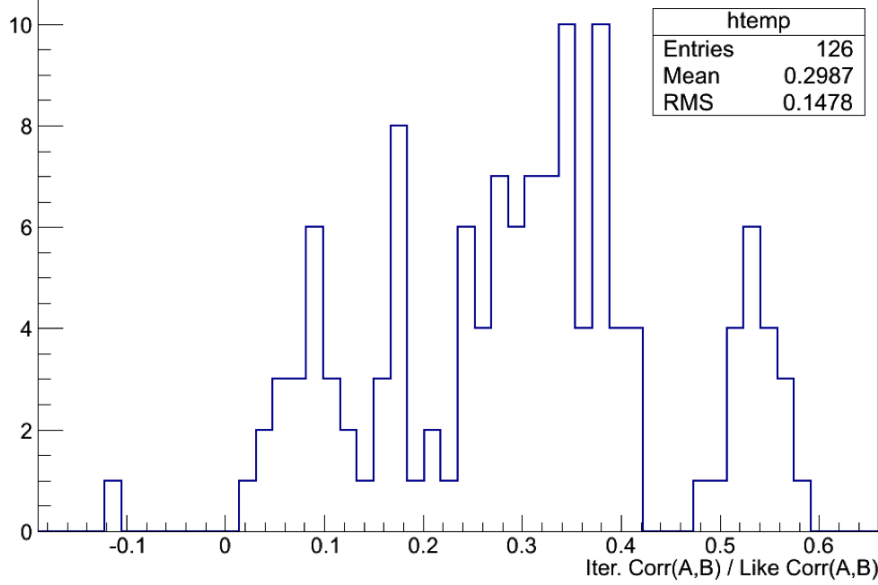


FIG. 79: Correlation between two parameters  $A$  and  $B$ , where  $(A, B) = (p_0, p_1)$ ,  $(A, B) = (p_0, p_2)$  and  $(A, B) = (p_1, p_2)$ , as estimated using the iterative approach divided by that using the 2D  $\chi^2$  profile.

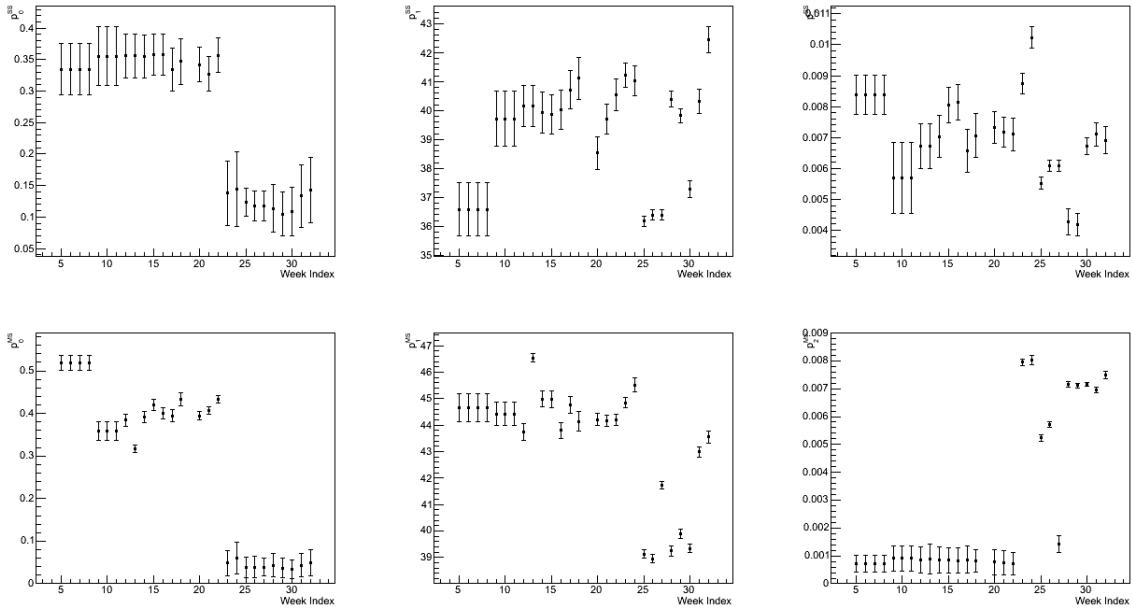


FIG. 80: Weekly resolution parameters as a function of the weeks.

## 2. Average Resolution and Parameters

The procedure to calculate the average resolution parameters is the following:

- the number of observed SS and MS events in physics runs are grouped by week ( $N_w^{SS}$  and  $N_w^{MS}$ , respectively, for week  $w$ ). The weekly time periods are those from the energy calibration and resolution parameters;
- each week is assigned a weight given by:  $W_w^{SS,MS} = N_w^{SS,MS} / \sum_w N_w^{SS,MS}$ ;
- the Th@S5 MC energy is smeared using each of the weekly resolution parameter sets;
- the resulting smeared MC energy distribution for each week is scaled by its corresponding weight,  $W_w^{SS,MS}$ , and then added together;

- the iterative approach is applied on the weighted sum of the MC energy distributions to obtain the average resolution parameters.

Figure 81 shows some samples of weighted smeared MC energy distributions and the resulting weighted sum, while figure 82 depicts the result of the iterative approach after 200 iterations. The average resolution parameters are calculated to be:

$$p_0^{SS} = 0.000682225 \sqrt{\text{keV}}, \quad p_1^{SS} = 40.6528 \text{ keV}, \quad p_2^{SS} = 0.00795144, \quad (32)$$

and

$$p_0^{MS} = 0.000278297 \sqrt{\text{keV}}, \quad p_1^{MS} = 42.5712 \text{ keV}, \quad p_2^{MS} = 0.00845904. \quad (33)$$

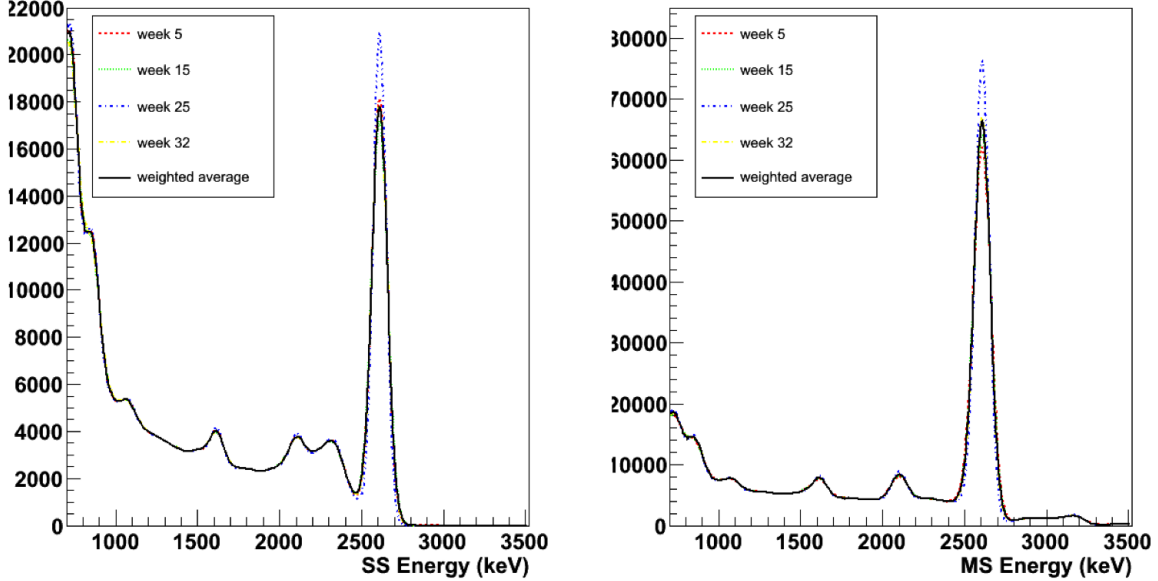


FIG. 81: Samples of weighted weekly MC energy distributions along with the final weighted sum distribution.

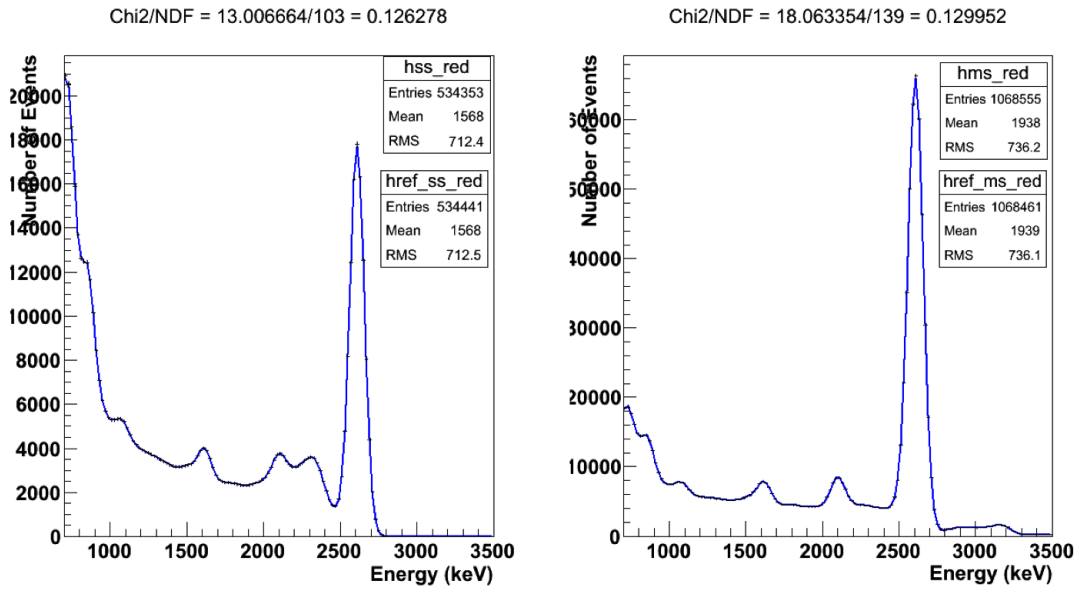


FIG. 82: Results of the iterative approach applied on the weighted sum energy distribution after 200 iterations.

Three sources of error are considered for the average resolution parameters. The first one arises from the application of the iterative approach on the weighted sum. This error is scaled by the size of the MC dataset and it is expected to be small. These covariance matrices for SS and MS resolution parameters are:

$$\Sigma_{SS}^{iter} = \begin{pmatrix} 0.00388068 & -0.000138496 & -1.21712 \times 10^{-8} \\ -0.000138496 & 0.0303011 & -5.1721 \times 10^{-6} \\ -1.21712 \times 10^{-8} & -5.1721 \times 10^{-6} & 1.53364 \times 10^{-8} \end{pmatrix} \quad (34)$$

and

$$\Sigma_{MS}^{iter} = \begin{pmatrix} 0.00179291 & -0.000281536 & -1.86156 \times 10^{-7} \\ -0.000281536 & 0.0092984 & -1.13479 \times 10^{-6} \\ -1.86156 \times 10^{-7} & -1.13479 \times 10^{-6} & 4.2027 \times 10^{-9} \end{pmatrix}. \quad (35)$$

The second source of error arises from the variation of the resolution parameters over time. This time variation can be observed in figure 73, and is expected to result in the most significant error. Its covariance matrices for the SS and MS resolution parameters are calculated by:

$$\Sigma_{ij,time}^{SS,MS} = \frac{\sum_{w=5}^{N_w} W_w^{SS,MS} (p_{i,w}^{SS,MS} - \bar{p}_i^{SS,MS}) (p_{j,w}^{SS,MS} - \bar{p}_j^{SS,MS})}{N_w - 1}, \quad (36)$$

where  $N_w$  is the number of weeks;  $W_w^{SS,MS}$  are the weights used in the calculation of the average parameters for SS and MS events, respectively;  $p_{i,w}$  is the weekly resolution parameter with  $i = 0, 1$  and  $2$  in week  $w$ ; and  $\bar{p}_i$  is the corresponding average resolution parameter. These covariance matrices for SS and MS resolution parameters arising from the time variation are:

$$\Sigma_{SS}^{time} = \begin{pmatrix} 0.00326648 & -0.0145155 & -8.51913 \times 10^{-6} \\ -0.0145155 & 0.214441 & 5.694 \times 10^{-5} \\ -8.51913 \times 10^{-6} & 5.694 \times 10^{-5} & 9.96546 \times 10^{-8} \end{pmatrix} \quad (37)$$

and

$$\Sigma_{MS}^{time} = \begin{pmatrix} 0.00467659 & 0.0208139 & -8.43685 \times 10^{-5} \\ 0.0208139 & 0.205081 & -0.000337749 \\ -8.43685 \times 10^{-5} & -0.000337749 & 1.62945 \times 10^{-6} \end{pmatrix}. \quad (38)$$

The last considered source of error arises from the statistical nature of the Th@S5 data. These are the errors of the weekly resolution parameters estimated by the iterative approach. Their propagation to the average resolution parameters is calculated as follows:

- draw  $N_d \sim 100 - 1000$  times the weekly resolution parameters using their covariance matrices;
- for each draw, obtain the weighted sum of the smeared MC energy distribution in a similar manner as that proceeded to obtain the average resolution parameters;
- apply the iterative approach for each draw;
- each draw results in new resolution parameters:  $p_{i,d}^{SS,MS}$ .

Finally, the propagation of the statistical errors are obtained using the following formula:

$$\Sigma_{ij,stat}^{SS,MS} = \frac{\sum_d^{N_d} (p_{i,d}^{SS,MS} - \bar{p}_i^{SS,MS}) (p_{j,d}^{SS,MS} - \bar{p}_j^{SS,MS})}{N_d - 1}. \quad (39)$$

These covariances matrices are calculated: (in calculation)

A first approximation can be obtained if the average parameters are considered as a simple weighted average of the weekly parameters. This is a valid approximation since this covariance matrix has elements that are significantly smaller than that caused by the time variation. They are calculated by:

$$\Sigma_{ij,stat}^{SS,MS} = \sum_{w=5}^{N_w} (W_w^{SS,MS})^2 \Sigma_{ij,week}^{SS,MS}, \quad (40)$$

which results in:

$$\Sigma_{SS}^{stat} = \begin{pmatrix} 5.62671 \times 10^{-5} & -0.000232331 & -2.40505 \times 10^{-7} \\ -0.000232331 & 0.0176009 & -4.83362 \times 10^{-6} \\ -2.40505 \times 10^{-7} & -4.83362 \times 10^{-6} & 1.57881 \times 10^{-8} \end{pmatrix} \quad (41)$$

and

$$\Sigma_{MS}^{stat} = \begin{pmatrix} 1.50974 \times 10^{-5} & -8.02213 \times 10^{-5} & -5.93974 \times 10^{-9} \\ -8.02213 \times 10^{-5} & 0.00440586 & -2.41816 \times 10^{-7} \\ -5.93974 \times 10^{-9} & -2.41816 \times 10^{-7} & 5.63476 \times 10^{-9} \end{pmatrix}. \quad (42)$$

The sum of the above three covariance matrices is:

$$\Sigma_{SS}^{total} = \begin{pmatrix} 0.00720343 & -0.0148863 & -8.77181 \times 10^{-6} \\ -0.0148863 & 0.262343 & 4.69342 \times 10^{-5} \\ -8.77181 \times 10^{-6} & 4.69342 \times 10^{-5} & 1.30779 \times 10^{-7} \end{pmatrix} \quad (43)$$

and

$$\Sigma_{MS}^{total} = \begin{pmatrix} 0.0064846 & 0.0204521 & -8.41883 \times 10^{-5} \\ 0.0204521 & 0.218785 & -0.000339126 \\ -8.41883 \times 10^{-5} & -0.000339126 & 1.63929 \times 10^{-6} \end{pmatrix}. \quad (44)$$

The resolution as a function of energy is depicted in figure 83. In particular, the resolution at the lower energy threshold (700 keV), at the  $Q$ -value (2458 keV) and at the characteristic peak of Th (2614 keV) are  $5.86 \pm 0.07\%$  ( $6.14 \pm 0.06\%$ ),  $1.84 \pm 0.03\%$  ( $1.93 \pm 0.05\%$ ), and  $1.75 \pm 0.03\%$  ( $1.84 \pm 0.06\%$ ) in SS (MS) events, respectively.

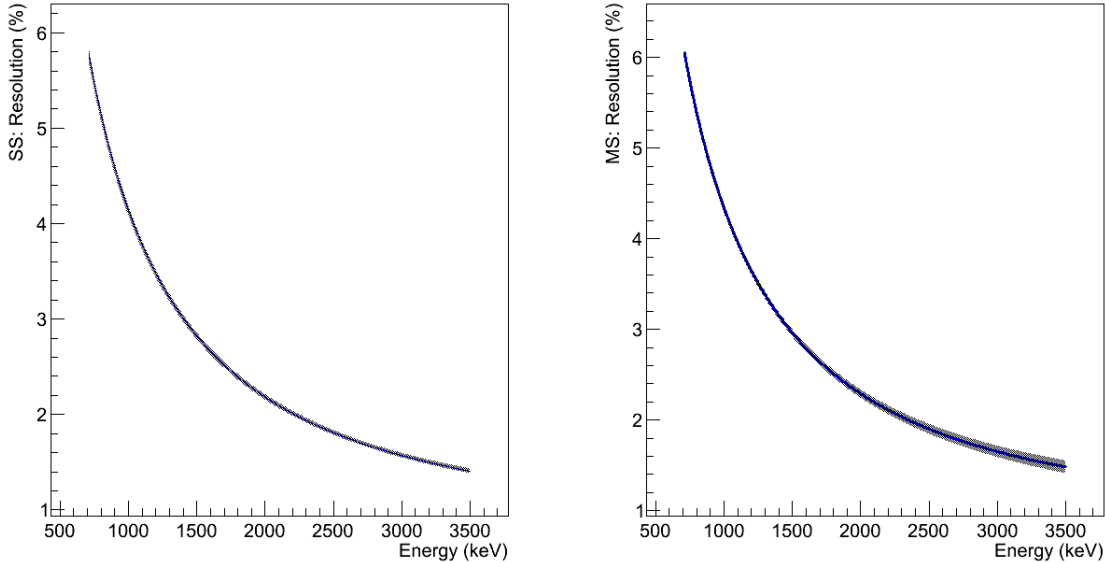


FIG. 83: Energy resolution curves as a function of the energy with errors represented by dotted bands in SS (left) and MS (right) events.

#### D. Future Work

During the course of this work, it was realized that the number of events available in MC simulation is not enough to allow the previous smearing procedure. This procedure consisted of simply throwing a Gaussian random number for each MC event to smear the MC energy distribution. In addition to the high correlation between energy bins, this procedure was observed to cause a jitter in 1D  $\chi^2$  profiles (figure 84). It follows from this issue the difficulty to minimize such function with standard minimization methods, especially those that rely on derivatives of the function.

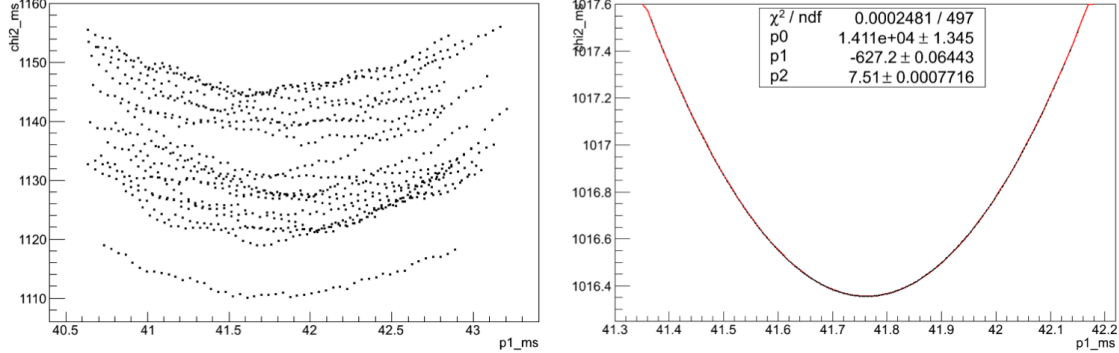


FIG. 84: 1D profile of the  $\chi^2$  as a function of  $p_1^{MS}$  before (left) and after (right) use of the appropriate smearing procedure.

After the above problem was fixed using the smearing procedure described in section VII B 2, MIGRAD was revisited in attempt to fit the resolution parameters using a fit of the Th@S5 MC model to its corresponding data. Even though the results of MIGRAD seem to further reduce the minimum values of the  $\chi^2$ , and modify significantly the resolution parameters, the resolution itself is not much affected. In addition, MIGRAD errors are based on the second derivative and can be dubious in case of a flat  $\chi^2$  near the minimum. The MINOS algorithm failed to calculate improved errors for the resolution parameters. Hence, a more robust usage of the iterative approach is proposed in which the results of MIGRAD are considered as the initial values of the parameters. However, based on the fact that the resolution is not expected to change much, and that the resolution parameter errors do not contribute significantly to the  $2\nu\beta\beta$  analysis, this proposal is going to be revisited in a later date.

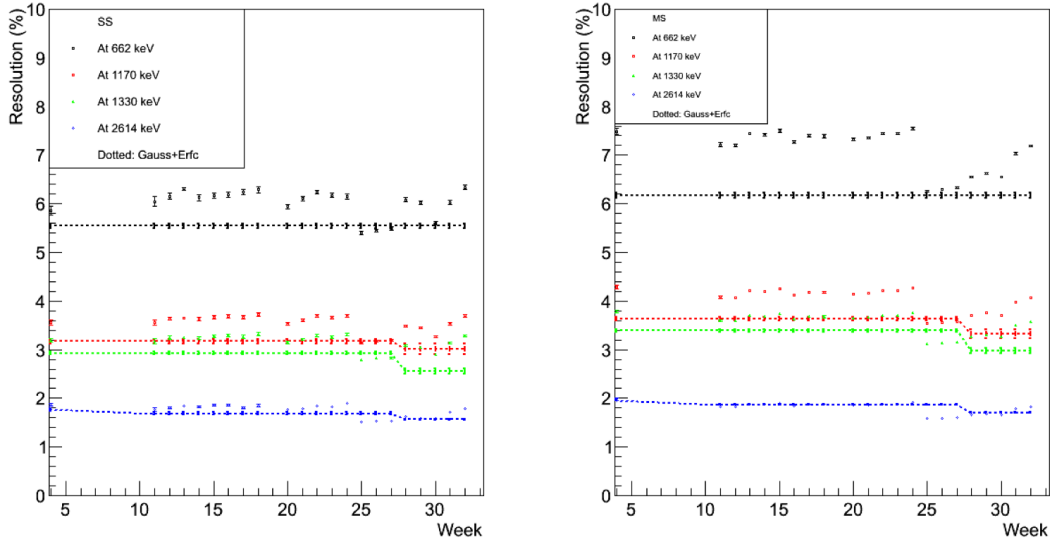


FIG. 85: Energy resolution obtained using the results from MIGRAD as initial values of the iterative approach.

Another possible improvement is the addition of more data in the iterative approach. Rather than using only Th@S5, any other available data can be included in a combined fit. This would make usage of all the calibration data available. However, one must balance between considering more data and how well the data is described by the MC simulation.

Finally, the iterative approach has shown itself as a promising method to improve the calculation of parameters of the detector. It is particularly interesting in problems with many parameters. This can be the case of EXO-200 detector if one decides to calculate the rotation angle, energy calibration and resolution parameters all at once. In particular, this could be applied to the charge-scintillation 2D energy spectrum, in a total of 13 parameters. For this reason, the current implementation of the iterative approach is planned to be extended in a flexible module. Its high CPU usage is a constraint that must be taken in consideration.

---

- [1] I. Ostrovskiy, <http://stanford.io/12ABiay>
- [2] R. Patterson, A search for muon neutrino to electron neutrino oscillations at  $\Delta m^2 > 0.1 \text{ eV}^2$ , PhD Thesis, 2007
- [3] Minuit Manual, <http://wwwasdoc.web.cern.ch/wwwasdoc/minuit/node33.html>

\*Some references for the older work are missing here.